Drop Size and Velocity Distributions in Sprays, A New Approach Based on the Maximum Entropy Formalism

by

Richard William Sellens

A thesis
presented to the University of Waterloo
in fulfilment of the
thesis requirement for the degree of

Doctor of Philosophy

in

Mechanical Engineering

Waterloo, Ontario, 1987

I hereby declare that I am the sole author of this thesis.

I authorize the University of Waterloo to lend this thesis to other institutions or individuals for the purpose of scholarly research.

I further authorize the University of Waterloo to reproduce this thesis by photocopying or by other means, in total or in part, at the request of other institutions or individuals for the purpose of scholarly research.

The University of Waterloo requires the signatures of all persons using or photocopying this thesis. Please sign below, and give address and date.

Abstract

A new basis for the prediction of the drop size and velocity distribution in a spray is developed, using the maximum entropy formalism. The prediction considers the imposition of integral conservation constraints for mass, momentum and mechanical energy on the breakup of an undulating liquid sheet. The resulting drop size distribution is similar to the widely used empirical distributions, while the velocity distribution is Gaussian, with a variance that decreases with increasing drop size.

Measurements were made in a simple water spray using the Phase / Doppler technique to obtain the joint size / velocity PDF. Photographic measurements were used to obtain an estimate of the geometry of the breakup region.

Good agreement was found between the measurements and the predictions, except in the region where drag forces had strongly influenced the distribution. This discrepancy was expected, as drag effects were not included in the model.

Acknowledgements

I would like to acknowledge the help of many people in producing this thesis, and in executing the work that it represents.

My supervisor, Tom Brzustowski, has provided continuing guidance in my work and his editorial skill has improved this thesis, as well as my other publications. I like to think that, under his influence, my first drafts are also improving.

It would not have been possible to complete this work in such a short time without the generous assistance in the experimental program from the people at the Lehrstuhl für Strömungsmechanik in Erlangen, West Germany. My thanks go the institute's director, Franz Durst, as well as Cam Tropea, Joachim Domnick and the many others who helped with my work while I was there.

Despite its disadvantages, sharing office space can enrich one's ideas. Much of what I've done and learned in the past few years has been clarified and expanded in discussions with my office mates in the Thermal Lab; Alex Breña, John Rapanotti and Beth Weckman.

Most important of all, this work would not have been possible without the support of my wife Peggy. She's had the strength to stand by me, explaining to our friends why I was doing this instead of a "real job", even when I was wondering myself. She has put up with a lot.

This work was supported by NSERC through the operating grant of Prof. T.A. Brzustowski and an NSERC Postgraduate Scholarship that I received for my final year of study.

Contents

List of Figures

List of Tables

Chapter 1

Introduction

The modelling of spray flames requires information on the joint drop size and velocity distribution of the fuel spray, and its variation over the spray volume. Its behaviour governs the distribution of the heat release over the combustion volume, as well as other phenomena important to the nature of the flame. Together with the gaseous flow field, the joint drop size and velocity distribution provides information of fundamental importance to the understanding of spray flames.

It is commonly suggested that a major area of uncertainty in spray modelling is in the definition of initial conditions. Until recently there has been no analytical basis for the distribution of drop size and velocity resulting from breakup. Recent work by the author [1,2,3] uses the maximum entropy formalism to analyze the breakup of a thin flat sheet of liquid, predicting a joint drop size and velocity distribution, and presents a simplified analysis of the downstream behaviour of the spray. The predicted distribution is similar to the Rosin–Rammler distribution in drop size and has a Gaussian distribution in velocity. However, the unrealistic flat sheet model requires the artificial inclusion of an arbitrary momentum

source term in the calculation of the velocity distribution. In real sprays produced by sheet-forming nozzles, the sheet does not remain flat prior to breakup, but develops undulations which contribute substantially to the breakup process.

1.1 Objectives

The objectives of this work are:

- to obtain a prediction of the form of the drop size and velocity distribution in a spray resulting from the breakup of an undulating liquid sheet.
- to make experimental measurements of such a spray, and compare them to the predictions.

To achieve these objectives this works builds on the previous work by:

- introducing a model for the behaviour of the undulating sheet.
- expanding the constraint equations to incorporate two components of velocity.
- introducing the additional constraint on the partition of surface energy.
- performing measurements for comparison with the results of the model.

1.2 Previous Work in Liquid Sheet Breakup

The importance of atomization in the combustion of liquid fuels has prompted a great deal of research. Nevertheless, there are still large gaps in the understanding of many of the mechanisms.

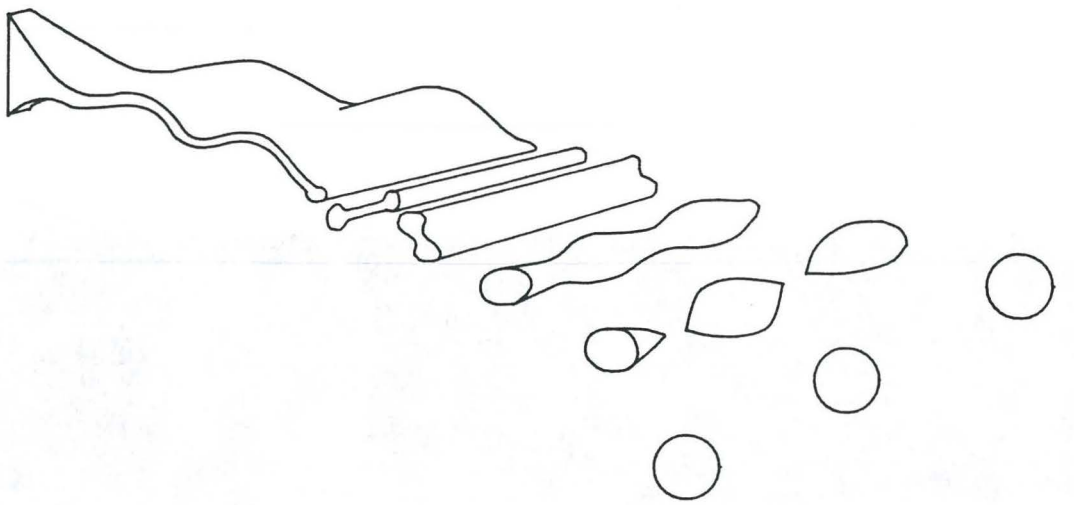

Figure 1.1: Idealized disintegration of a liquid sheet. After Dombrowski and Johns [4].

The research literature on atomization can be divided into two parts. By far the larger part is concerned with the description of sprays. This work is primarily empirical, usually involving the measurement of the drop size distributions produced by practical devices and fitting a distribution equation to the data. Practical parameters, such as the Sauter mean diameter (D_{32}), may then be extracted and correlations developed between the important features of the drop size distribution and the design and operating parameters of the atomizers used. Much of the modern work of this type has been reported in the proceedings of the *International Conferences on Liquid Atomization and Spray Systems (ICLASS-78, -82, -85)*.

The remaining research has focussed on the stability of liquid sheets and ligaments subject to some specific forms of disturbances. This work begins with Rayleigh's 1878 paper on the stability of cylindrical jets subject to sinusoidal disturbances [5]. It goes on to include the effects of liquid viscosity [6], deformation wavelength and asymmetry [7], aerodynamic

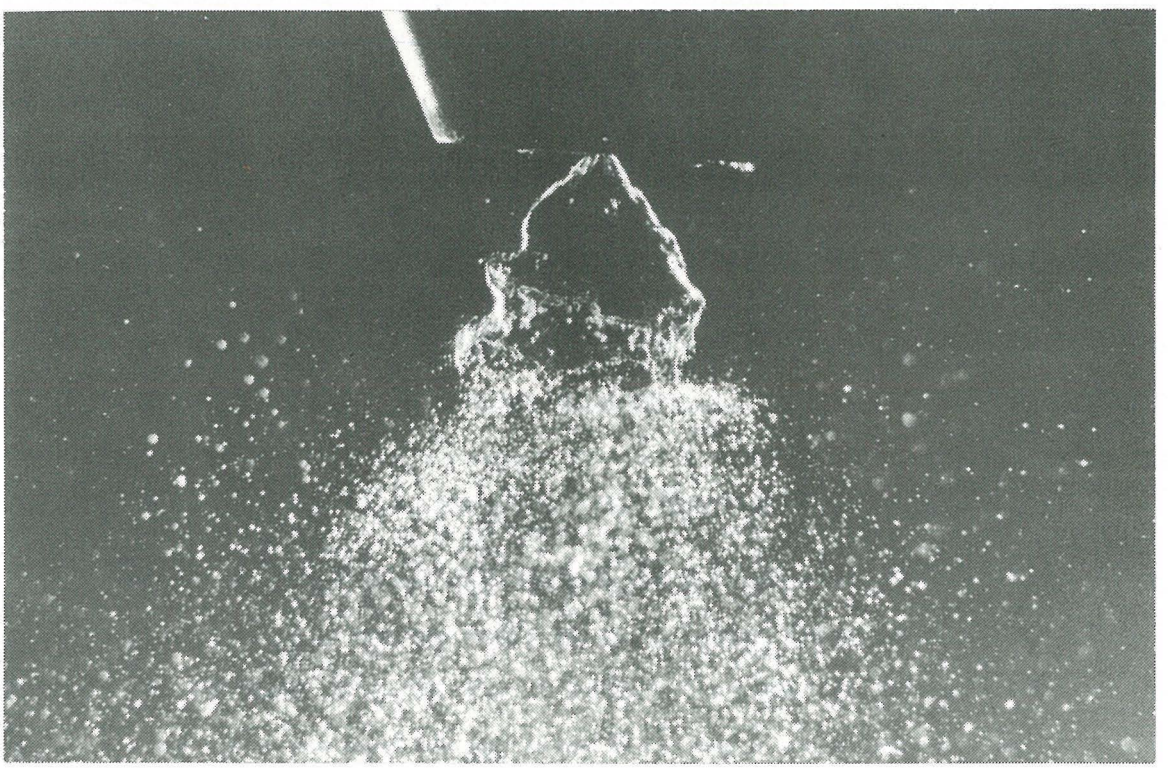

Figure 1.2: Disintegration of the conical sheet produced by a swirl jet nozzle. This photograph shows a spray of water from a Delavan 1.50 80 B nozzle. The water temperature was 20° C and the injection pressure was 345 kPa.

effects of relative gas-liquid velocity [6,7], growth and breakup of surface waves [8], liquid sheet breakup [4], and secondary breakup of drops at very high relative velocities [9]. These theoretical studies are well supported by many experimental studies. However, such work does not yield any description of the spray produced beyond some expression for an average or maximum drop diameter on the basis of the parameters of the disturbances which are most readily amplified. The main features of this research are well summarized by Rice [10].

The work of Dombrowski and Johns [4] on breakup of liquid sheets is of particular interest in the present work. It provides the background for the present model of the sheet behaviour prior to breakup.

Dombrowski and Johns consider the behaviour of a viscous liquid sheet in quiescent, inviscid, gaseous surroundings. The balance of aerodynamic, surface and liquid viscous forces governs the growth of sinuous disturbances on a sheet. It is assumed that the disturbances of maximum growth rate dominate the behaviour, thus simplifying the analysis.

The breakup length is reached when the troughs and crests of the undulations blow out, leaving segments of sheet, each one half a wavelength long. These segments then contract into ligaments and break up by the classical mechanisms of the unstable liquid cylinder. See figures 1.1 and 1.2 for the idealized and actual behaviour of a sheet respectively. Applying the ligament breakup model of Weber [6] to their theoretical predictions they predict a mean drop diameter that is in reasonable agreement with experiments. This suggests that, at least, their qualitative description of the process is reasonably accurate. That description will be used, in conjunction with basic conservation principles and the maximum entropy formalism, to predict the distribution of drop size and velocity in the present work.

Chapter 2

Maximum Entropy Formalism Applied to the Breakup of a Liquid Sheet

2.1 The Maximum Entropy Formalism

The maximum entropy formalism of Jaynes [11,12] and Tribus [13] is a method of statistical inference which has found substantial application in scientific and engineering problems. It was initially perceived as an alternative approach to statistical thermodynamics. However, it is now being recognized as a method of statistical inference which is generally applicable, rather than specifically a tool for thermodynamics.

The formalism provides a method for maximizing the Shannon entropy

$$S = -k \sum_{j=0}^{m} p_j \ln p_j \tag{2.1}$$

of a probability distribution, subject to constraints of the form

$$\sum_{j=0}^{m} p_j g_j =< g > \tag{2.2}$$

where g_j is the set of values of some state function and $< g >$ is the expectation value for that state function, which known to exist and have a single value. This results in the least biased distribution of probability which still satisfies the constraints of a particular physical problem.

The constraints define some average property of the system, or moment of the probability distribution. This form of constraint is ideal for expressing conservation equations. For example, if the state function g were energy, a conservation constraint might read: "The sum of the energy over the entire system is equal to the total energy". On this sort of basis one may make predictions of the probability distribution based on its known moments.

The author has shown [3] that, for a uniform discretization of the solution space ψ, the constraints of the formalism and the resulting probability distribution may be expressed in a continuous form.

$$\int_{\psi} f g_0 d\psi =< g_0 > \tag{2.3}$$

$$\int_{\psi} f g_1 d\psi =< g_1 > \tag{2.4}$$

$$\ldots$$

$$\int_{\psi} f g_n d\psi =< g_n > \tag{2.5}$$

$$f = \exp(-\lambda_0 - \lambda_1 g_1 - \lambda_2 g_2 - \ldots - \lambda_n g_n) \tag{2.6}$$

where f is a probability density function (PDF) such that $p_j = f d\psi_j$. The normalization constraint 2.3 arises from the restriction that the probabilities must sum to unity. The state

functions g_0 is defined as unity and therefore $< g_0 >= 1$. This allows the normalization constraint to be written in the same form as the other constraint equations. This form is well suited to the treatment of continuous variables such as the drop size and velocity, which form the solution space in this work.

The as-yet-undetermined Lagrange multipliers, λ_0, λ_1, λ_2,...,λ_n, may be found using a modified Newton–Rhapson type numerical solution. The method developed by the author for finding the multipliers [3] was an improvement over earlier methods. The critical step in the solution is the enforcement of the normalization constraint at every iteration. Without this requirement the solution is strongly divergent.

When the entropy of the distribution is at a maximum, subject to the constraints, the result is the least biased distribution which satisfies the physics embodied in the constraints. In the language of information theory, it contains the least amount of information, i.e. only the information embodied in the constraints. Any other distribution would be biased, because it would contain more information than the physics provides. Qualitatively, the result may be thought of as the smoothest distribution that satisfies the constraints. It reveals no non-uniformities except those required by the physics of the system, as expressed in the constraints.

For more detailed information on the maximum entropy formalism and its solution for a probability distribution refer to references [13] and [14], or reference [3] as excerpted in Appendix A.

2.1.1 Application Approaches for the Maximum Entropy Formalism

There are various ways to apply the maximum entropy formalism in problems involving probability distributions. There is the obvious approach which directly parallels the deriva-

tion. A set of constraints is known a priori and the maximum entropy principle is used to find the least biased distribution of probabilities that satisfies those constraints.

A more complex approach is the inverse problem. In this case the distribution is known, and the objective is to obtain a set of constraints which, in conjunction with the maximum entropy principle, would yield that distribution. There is no direct path to the solution of this type of problem. However, if a solution is found, it may offer insight into the fundamental principles which underlie the observed distribution.

The present work combines the two approaches. A set of fundamental conservation constraints is determined a priori to be of physical importance in the atomization process. The distribution resulting from the maximization of the entropy, subject to these constraints, is compared to the observed distributions in real sprays and some inconsistencies are evident. This observation drives the inverse process; a search for some physical aspect which has been overlooked. A further constraint is sought, and found, which will bring the distribution into line with the empirical evidence. This is one of the strengths of the formalism. An incomplete analysis can point the way to an improvement in the system of constraints, resulting in a better solution and increased understanding of the physical processes.

2.2 Conservation Constraints on Breakup

Many atomizers function by producing a thin sheet of liquid which develops instabilities, breaking up into ligaments and then into drops. The swirl jet atomizer, for example, produces a conical sheet in which the fluid is stretched by the initial radial momentum, until breakup occurs. This work begins with a sheet which has already been stretched to the point of breakup. The sheet has a thickness r, which is assumed to be uniform, and a mean velocity in the streamwise direction U. There are undulations on the surface of

the sheet which are growing as the sheet moves downstream. As a result of these growing undulations any small element of the sheet will have both streamwise and cross-stream components of velocity.

Constraints are developed by assuming that the breakup is a nearly conservative process. The collection of drops just downstream of the breakup zone are taken to have the same total mass, momentum, directed kinetic energy and surface energy as the portion of the sheet that broke up to form them. The techniques used to develop values for the average momentum and kinetic energy of the undulating sheet are described in a later section. The process is assumed to be isothermal, with constant fluid properties.

The probability is distributed over the drop diameter, δ, and two components of drop velocity, u and v, each of which are nondimensionalized as shown, using the mass mean diameter and the mean streamwise sheet velocity respectively.

$$\delta_* = \frac{\delta}{D_{30}} \qquad u_* = \frac{u}{U} \qquad v_* = \frac{v}{U} \tag{2.7}$$

The solution space consists of the three variables combined, so that $d\psi = d\delta_* du_* dv_*$.

2.2.1 Conservation of Mass

The mass conservation constraint for the liquid arises from the statement that the total mass M from the sheet must be equal to the sum of all the drop masses, plus any mass sources due to a nonconservative process. For example, evaporation would lead to a negative mass source. N is the total number of drops, so that $Nfd\psi$ is the number of drops in an incremental volume of solution space.

$$M = \iiint_{\psi} Nf\frac{\rho\pi\delta^3}{6}d\psi \quad - \quad \text{mass sources} \tag{2.8}$$

By recalling that

$$\frac{M \quad + \quad \text{mass sources}}{N} = \frac{\rho\pi D_{30}^3}{6} \tag{2.9}$$

the above expression may be recast in a dimensionless form.

$$\iiint_{\psi} f\delta_*^3 d\delta_* du_* dv_* = 1 \tag{2.10}$$

2.2.2 Conservation of Momentum

Similar methods may be used to develop equations for the components of linear momentum. Two components are considered. The x axis is aligned with the mean motion of the sheet, while the y axis is perpendicular to the sheet.

$$M\overline{u}_s = \iiint_{\psi} Nf\frac{\rho\pi\delta^3}{6} u d\psi \quad - \quad \text{x momentum sources} \tag{2.11}$$

and

$$M\overline{v}_s = \iiint_{\psi} Nf\frac{\rho\pi\delta^3}{6} v d\psi \quad - \quad \text{y momentum sources} \tag{2.12}$$

which relate the momentum of the sheet to the momentum of the drops in the resulting spray. Nondimensionalization then gives

$$\iiint_{\psi} f\delta_*^3 u_* d\delta_* du_* dv_* = \overline{u}_{s*} + S_{mu} \tag{2.13}$$

and

$$\iiint_{\psi} f\delta_*^3 v_* d\delta_* du_* dv_* = \overline{v}_{s*} + S_{mv} \tag{2.14}$$

for the x and y components respectively.

2.2.3 Conservation of Energy

Initially one would expect the conservation of energy to provide a single constraint. However, this would leave out important information concerning the physics of certain energy transformations, as well as the prior knowledge of the energy distribution before breakup. A single constraint would not account for the barriers to transformation between different modes of energy. The model must incorporate the fact that kinetic energy does not transform to surface energy unless there are deformation processes taking place that facilitate the transformation. Because of this each energy mode is separately conserved, with source terms to permit the exchange of energy between modes. The two energy modes of importance in the current study are surface energy and directed kinetic energy.

Conservation of Kinetic Energy

The directed kinetic energy of all the drops in the distribution must match the kinetic energy present in the sheet that broke up to form them. Balancing the two gives

$$M\overline{(u_s^2+v_s^2)} = \iiint_{\psi} N f \frac{\rho\pi\delta^3}{6}(u^2+v^2)d\delta_* du_* dv_* \quad - \quad \text{kinetic energy sources} \tag{2.15}$$

or, on nondimensionalization

$$\iiint_{\psi} f\delta_*^3(u_*^2+v_*^2)d\delta_* du_* dv_* = \overline{u_{s*}^2+v_{s*}^2} + S_{ke} \tag{2.16}$$

Conservation of Surface Energy

The surface energy is simply the surface tension, σ, multiplied by the surface area, so that balancing the surface area of the drops with that of the original sheet gives

$$\frac{2\sigma M}{\rho\tau} = \iiint_{\psi} \sigma N f \pi \delta^2 d\delta_* du_* dv_* \quad - \quad \text{surface energy sources} \tag{2.17}$$

for a sheet of locally uniform thickness τ. The factor of two allows for the two sides of the sheet. This becomes

$$\iiint_{\psi} f\delta_*^2 d\delta_* du_* dv_* = \frac{1}{3\tau_*} + S_s \tag{2.18}$$

on nondimensionalization. Alternately, since the net surface area in the resulting spray must be equal to the surface area of the sheet, plus any surface area sources,

$$\sigma A_{net} = \frac{2\sigma M}{\rho\tau} \quad + \quad \text{surface energy sources} \tag{2.19}$$

and equation 2.18 may be expressed in terms of the net surface area per unit mass.

$$\iiint_{\psi} f\delta_*^2 d\delta_* du_* dv_* = \frac{\rho D_{30}}{6(1+R_m)} \frac{A_{net}}{M} \tag{2.20}$$

where R_m is the mass source term expressed on a per unit mass basis. $(1 + R_m)M/\rho$ is the total volume of liquid in the spray. Examination of the definition of the Sauter mean diameter (D_{32}) shows that it is equal to 6 times the overall volume to surface area ratio. Thus, the constraint may be rewritten as

$$\iiint_{\psi} f\delta_*^2 d\delta_* du_* dv_* = \frac{D_{30}}{D_{32}}, \tag{2.21}$$

the form used in the model calculations of Chapter 5. This eliminates the need to obtain the surface energy source terms directly. The surface energy source term will be negative, representing the dissipation of a large portion of the surface energy in the processes of contraction that take place in the breakup region.

2.3 The Complete Set of Conservation Equations

When all of these constraint equations are combined with a normalization constraint they provide a complete description of all the information given by the conservation laws about the drop size and velocity distribution. This gives the following set of constraints on the distribution.

$$\text{Normalization} \qquad \iiint_{\psi} f d\delta_* du_* dv_* = 1 \tag{2.22}$$

$$\text{Surface Energy} \qquad \iiint_{\psi} f \delta_*^2 d\delta_* du_* dv_* = \frac{1}{3\tau_*} + S_s = \frac{\rho D_{30}}{6(1+R_m)} \frac{A_{net}}{M} = \frac{D_{30}}{D_{32}} \tag{2.23}$$

$$\text{Mass} \qquad \iiint_{\psi} f \delta_*^3 d\delta_* du_* dv_* = 1 \tag{2.24}$$

$$\text{X Momentum} \qquad \iiint_{\psi} f \delta_*^3 u_* d\delta_* du_* dv_* = \overline{u}_{s*} + S_{mu} \tag{2.25}$$

$$\text{Y Momentum} \qquad \iiint_{\psi} f \delta_*^3 v_* d\delta_* du_* dv_* = \overline{v}_{s*} + S_{mv} \tag{2.26}$$

$$\text{Kinetic Energy} \qquad \iiint_{\psi} f \delta_*^3 (u_*^2 + v_*^2) d\delta_* du_* dv_* = \overline{u_{s*}^2 + v_{s*}^2} + S_{ke} \tag{2.27}$$

The maximum entropy formalism then yields the PDF:

$$f = \exp\left(-\lambda_0 - \lambda_1 \delta_*^2 - \lambda_2 \delta_*^3 - \lambda_3 \delta_*^3 u_* - \lambda_4 \delta_*^3 v_* - \lambda_5 \delta_*^3 (u_*^2 + v_*^2)\right) \tag{2.28}$$

describing the joint distribution of drop size and velocity. The Lagrange multipliers must still be determined numerically for each individual case.

2.3.1 Inadequacy of the Previous Flat Sheet Model

Notice that, for a flat sheet moving in the x direction at a uniform velocity so that $u_* = U$ and $v_* = 0$, equation 2.26 becomes meaningless $(0 = 0)$ and equations 2.25 and 2.27 reduce to

$$\iiint_{\psi} f\delta_*^3 u_* d\delta_* du_* dv_* = 1 + S_{mu} \tag{2.29}$$

$$\iiint_{\psi} f\delta_*^3 u_*^2 d\delta_* du_* dv_* = 1 + S_{ke} \tag{2.30}$$

These are the equations used in the previous flat sheet work [1]. If the momentum and kinetic energy source terms are both set to zero, then the drops would all have one velocity. This is because, when both of the source terms are neglected, the constraint equations 2.29 and 2.30 taken in combination state that the variance of the velocity must be zero. Clearly this is not the case for real spray systems. To compensate for this shortcoming a small negative momentum source was arbitrarily included to produce an initial distribution of velocity. The current, more realistic model does not require this type of arbitrary modification to produce a qualitatively realistic result.

2.4 Addition of a Constraint on the Partition of Surface Energy

When the equations of section 2.3 are applied, a solution may be obtained. An example of such a solution is shown in figure 2.1. This solution is not in agreement with the characteristics of most experimental results. The probability associated with the smaller drop sizes is much larger than is generally observed.

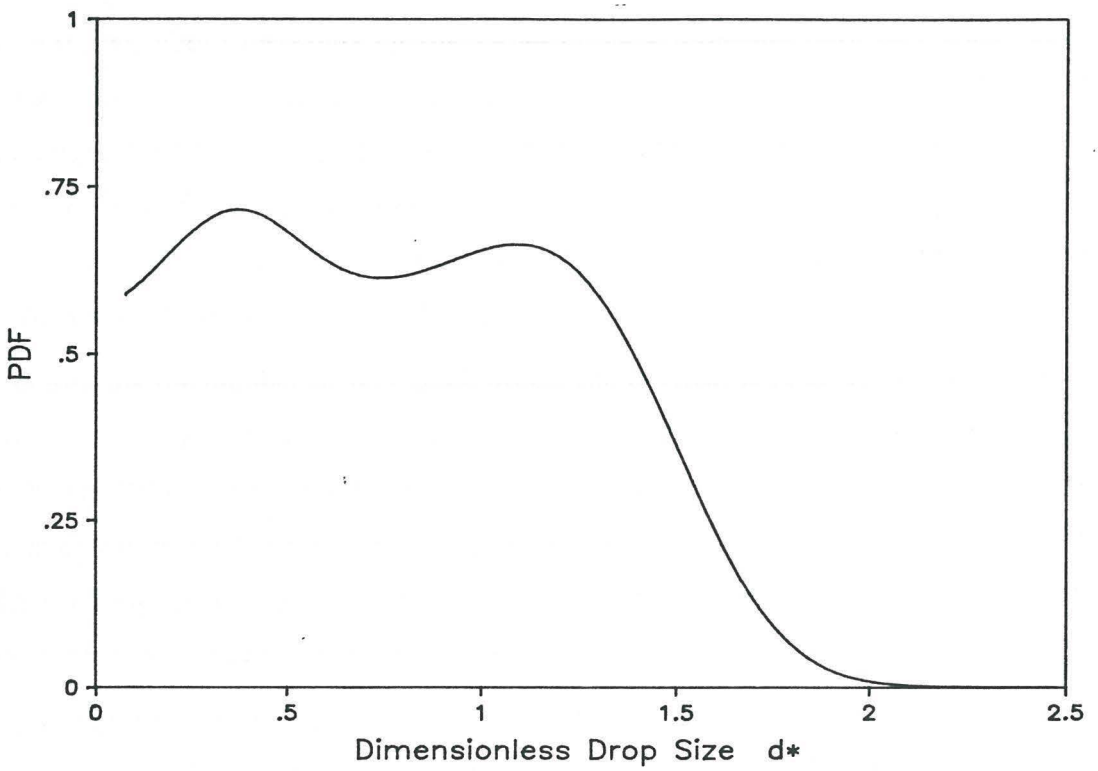

Figure 2.1: Sample solution of conservation constraints. This figure shows typical output from the model when only the conservation constraints are applied. The conservation constraints do not include a mechanism to suppress the probability at small drop sizes, hence the high values of the PDF at small drop sizes.

This high value of probability is due to a deficiency in the conservation constraints. All of these constraints are positive moments of the drop size, or drop size and velocity. The lowest order moment of drop size is the second moment that forms the surface area constraint. The smallest drop sizes make very little contribution to the values of these moments, therefore constraints on the values of these moments have very little effect on the nature of the distribution at small drop sizes. Where the constraints have little effect, the entropy maximization dominates the results. Thus the distribution at small drop sizes is simply the smoothest curve that can be accommodated by the rest of the distribution. This drives one to search for an additional physical constraint which will have some effect in reducing the PDF values at small drop sizes.

In limiting the number of very small drops, the physical process at work is a limitation of the concentration of surface energy. With fixed values of surface tension, flow velocities, etc. it is unlikely that sufficient deformation energy will be expended on an element of mass to reduce the drop size beyond a certain point. The critical quantity is the surface to mass ratio of a drop. It is limited by the amount of deformation energy that a small element of mass can absorb within that particular spray flow.

The simplest constraint that can be applied is the statement that the surface-area-to-volume ratio of the drops in the spray has some mean value – which need not be known in advance.

$$\text{Mean Surface to Volume Ratio} = \iiint_{\psi} f \pi \delta^2 \left(\frac{\pi \delta^3}{6} \right)^{-1} d\psi \tag{2.31}$$

For a given spray the mean surface to volume ratio exists, and this constraint may be rearranged as

$$\iiint_{\psi} f \delta_*^{-1} d\delta_* du_* dv_* = K_p \tag{2.32}$$

where the value of K_p expresses the strength of the partition constraint.

When this constraint is added to the system of conservation constraints, and the entropy is maximized, the resulting PDF is

$$f = \exp\left(-\lambda_0 - \lambda_1\delta_*^2 - \lambda_2\delta_*^3 - \lambda_3\delta_*^3 u_* - \lambda_4\delta_*^3 v_* - \lambda_5\delta_*^3(u_*^2 + v_*^2) - \lambda_6\delta_*^{-1}\right). \qquad (2.33)$$

The Lagrange multipliers must be determined individually for each case. This expression is the basis of the results presented in Chapter 5.

Chapter 3

Liquid Sheet Behaviour Prior to and During Breakup

In Chapter 2 constraints on the drop size and velocity distribution were developed based on a knowledge of the behaviour of an undulating sheet just before breakup. To provide that input, some of the sheet's behaviour must be modelled. This chapter presents a model of sheet behaviour, and the means for extracting mean velocity information from that model.

3.1 The Present Model

In the present work the sheet is modelled, following Dombrowski and Johns [4], as having sinusoidal undulations which are growing in amplitude as the sheet moves downstream. The undulations are taken as fixed on the sheet, so that both move together in the streamwise direction with an average velocity of U. This seems to be a reasonable assumption, as the driving aerodynamic forces are essentially symmetrical about the peaks and would not be

expected to drive the undulations along the sheet. Thus, as the sheet moves out and the undulations grow, the same element of mass remains at the same relative position on the disturbance. Elements on the axis remain on the axis. Elements at the peaks remain at the peaks. If the thinning of the sheet due to undulation growth is presumed to be uniform, then intermediate elements will maintain the same relative position between the axis and the peak, along the curve of the sheet.

These approximations result in an idealized model of the sheet which does not incorporate many of the small scale movements. However, the description of the large scale motion is sufficient to provide an estimate of the mean momentum and kinetic energy.

Expressed mathematically, the centerline of the sheet is taken to follow

$$y = \frac{A(x)}{2} \sin\left(\frac{2\pi}{\lambda}(x - Ut)\right) \tag{3.1}$$

where x is the streamwise direction, y is the cross-stream direction, t is time, λ is the wavelength of the disturbance and $A(x)$ is an amplitude function that grows with x. In this work an exponential amplitude function is used, as that is the form predicted by Dombrowski and Johns. Figure 3.1 shows such a sheet at two successive points in time, illustrating the motion of individual elements of fluid. Over a short period of time an element of fluid at the point B moves to the point B' which is the same relative distance between A' and C' as B is between A and C. This is a consequence of assuming a locally uniform sheet thickness. This assumption and equation 3.1 together allow the calculation of the velocity of each element of fluid in the sheet by defining the way they move with time.

Consider s as the dimension along the sheet, so that the relative distance from A to B

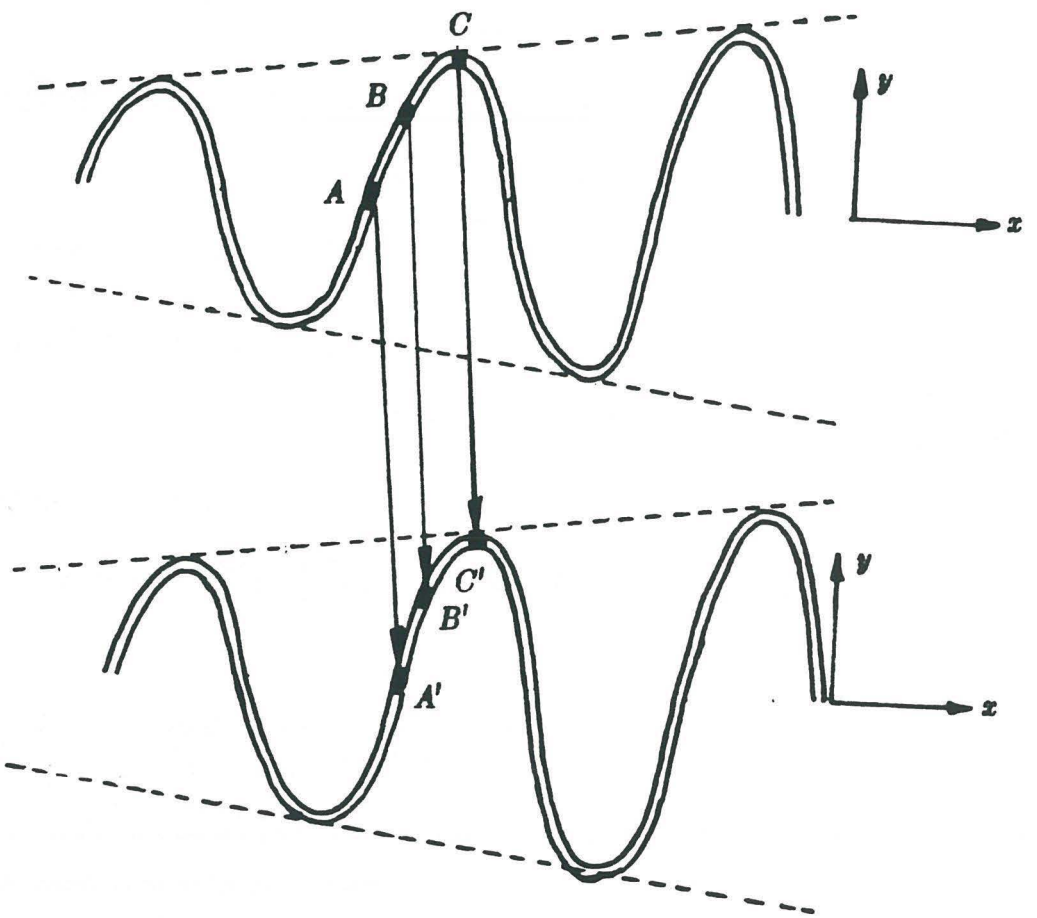

Figure 3.1: Development of the undulations with time.

is

$$\frac{\int_A^B ds}{\int_A^C ds}$$

Thus the points B and B' are correctly matched when

$$\frac{\int_A^B ds}{\int_A^C ds} = \frac{\int_{A'}^{B'} ds}{\int_{A'}^{C'} ds} \tag{3.2}$$

The problem is brought into the $x - y$ frame of reference by transforming coordinates.

$$(ds)^2 = (dx)^2 + (dy)^2 \tag{3.3}$$

From differentiation of equation 3.1

$$dy = \left(\frac{1}{2}\frac{dA(x)}{dx}\sin\left(\frac{2\pi}{\lambda}(x - Ut)\right) + \frac{\pi}{\lambda}A(x)\cos\left(\frac{2\pi}{\lambda}(x - Ut)\right)\right)dx \tag{3.4}$$

so that

$$ds = \left(1 + \left(\frac{1}{2}\frac{dA(x)}{dx}\sin\left(\frac{2\pi}{\lambda}(x - Ut)\right) + \frac{\pi}{\lambda}A(x)\cos\left(\frac{2\pi}{\lambda}(x - Ut)\right)\right)^2\right)^{\frac{1}{2}} dx \tag{3.5}$$

Because B' is the location of the element from point B a short distance in time later, the velocity of point B may be calculated as

$$u_s = \frac{x_{B'} - x_B}{\Delta t} \qquad v_s = \frac{y_{B'} - y_B}{\Delta t} \tag{3.6}$$

In addition, the mass averages for the region AC are

$$\overline{u}_s = \frac{\int_A^C \rho\tau u_s ds}{\int_A^C \rho\tau ds} \tag{3.7}$$

$$\overline{v}_s = \frac{\int_A^C \rho\tau v_s ds}{\int_A^C \rho\tau ds} \tag{3.8}$$

$$\overline{u_s^2 + v_s^2} = \frac{\int_A^C \rho\tau (u_s^2 + v_s^2) ds}{\int_A^C \rho\tau ds} \tag{3.9}$$

Since the sheet thickness and liquid density have been assumed constant over the segment in question, these expressions may simplified.

$$\overline{u}_s = \int_A^C u_s \, d\left(\frac{s}{s_{AC}}\right) \tag{3.10}$$

$$\overline{v}_s = \int_A^C v_s \, d\left(\frac{s}{s_{AC}}\right) \tag{3.11}$$

$$\overline{u_s^2 + v_s^2} = \int_A^C (u_s^2 + v_s^2) \, d\left(\frac{s}{s_{AC}}\right) \tag{3.12}$$

Thus, the values for the mass averages may now be calculated numerically. Due to the mathematics of the change in amplitude with x, the relative position of the peaks and zero crossings within a one wavelength segment changes slightly with downstream motion. To maintain the alignment of peaks and zero crossings specified by the model, the calculations must be made over a quarter wavelength segment, starting at either a peak or a zero crossing. Averaging over four segments will then provide an overall picture of a one wavelength segment of the sheet near breakup.

3.1.1 Numerical Calculation of Mass Averages

The values of the mass average quantities for a region of the sheet are calculated by the following procedure

- In order to examine an undulation immediately prior to breakup, a starting point A is selected with an x location near the breakup length, as determined from the photographic measurements. The time base is then adjusted so that point A is a positive going zero crossing. This locates the other end point C, one wavelength downstream, and the corresponding end points A' and C', Δt later.
- Calculations are made for each one of a set of points B. At each point
  - The relative distance from A to B is calculated by numerical integration using Simpson's rule.
  - A shooting algorithm is used to find the point B' which is the same relative distance from A'.
  - The coordinates of the two points and the time differential provide the velocity components and the sum of the squares.
- The values for the individual points in the set are then used for another integration over the length of the segment, yielding the mass average quantities for that segment of the sheet.

3.1.2 Source Terms in Breakup

Each of the conservation constraints includes a source term to reflect any deviation from a purely conservative breakup process. They are generally small but some will be significant

in the breakup of the sheet. The following paragraphs discuss each of the source terms briefly.

The mass source term is included to reflect any changes due to processes such as evaporation. Although evaporation is very important to the spray as a whole it is reasonable under most conditions to neglect the evaporation that takes place during the short breakup period. Exceptions would include situations such as sprays at temperatures above their flash point. In those cases a nonzero mass source term would change the numerical results, but the basic nature of the model would remain unchanged.

The source terms for momentum and kinetic energy will reflect any acceleration of the liquid through environmental interactions such as drag, and perhaps some surface effects. These source terms are set to zero on the assumption that the accelerations due to environmental interactions are small within the breakup region.

The surface source term accounts for changes in surface energy during breakup. As the liquid sheet breaks up its surface area is reduced, first by the contraction of sheet segments into ligaments, and then by the breakup of those ligaments into droplets. Dombrowski and Johns [4] provide a model for this reduction, however, in this case the experimental work provides a better indication of actual values.

Chapter 4

Experimental Procedures

The experimental work described here was performed in two parts. The assembly of the Phase / Doppler system and the measurements of the joint drop size and velocity distributions were carried out during the fall of 1986 at the Lehrstuhl für Strömungsmechanik (LSTM) in Erlangen, West Germany. The photographic work and the measurements of flow rates through the nozzles were done at the University of Waterloo in the winter and spring of 1987.

The theoretical work describes the breakup of a sheet in terms of the thickness of the sheet and the characteristics of the undulations. Because of this, it is desirable to work in a spray where these data may be easily measured, or estimated. Two common types of sheet producing nozzles are the fan spray nozzle, which produces a plane sheet of liquid, and the swirl jet nozzle, which produces a conical sheet.

4.1 The Spray Flow

The selected spray flow must satisfy several criteria:

- It must be suitable for application of the model. i.e. the nozzle must produce a thin liquid sheet subject to aerodynamic instabilities.
- It must be feasible to make measurements of both the spray and undulating sheet characteristics.
- It must be easily moved, as the spray measurements were to be made in Germany.

The simplest flow to which the model may be applied is a spray into a quiescent environment. This type of flow also satisfies the remaining constraints. Since no wind tunnel or flow enclosure is required, the important elements of the system are easily moved and there is no interference with the optical access necessary for measurements.

The area of interest in this work is the region in the immediate vicinity of the nozzle. In this region flow velocities are much higher than typical room air circulation velocities and the flow is driven by the nozzle momentum. Since the flow was dominated by the nozzle momentum, no special efforts were necessary to suppress the ambient air currents. This is not true in the far field, however no measurements were made at distances greater than 15 mm downstream from the nozzles.

Swirl jet nozzles were chosen for the experimental work on the basis of availability. Widely available domestic oil burner nozzles produce a thin conical sheet of liquid at moderate operating pressures. The only available fan spray nozzles produced thick liquid sheets that were unaffected by the aerodynamic instability and produced a very coarse spray. These nozzles are similar to those found in automatic car washes. Two commercial oil

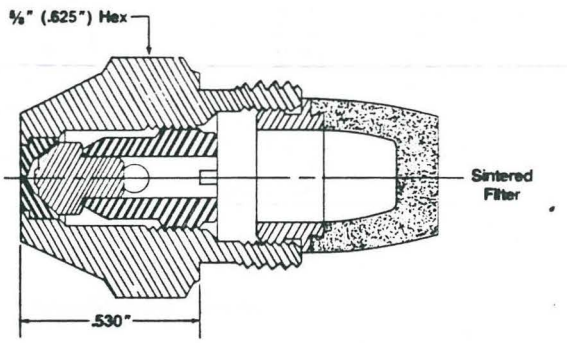

Figure 4.1: Basic design of Delavan oil burner nozzles. This drawing shows the basic design of the 1.50 80 B nozzle used in the experiments. The 3.00 80 A nozzle was of the same design, except that it was fitted with a mesh strainer rather than a sintered filter. Nozzle drawing courtesy of Delavan Inc [15].

burner nozzles were selected for the experiment. The nozzles are manufactured by Delavan Inc [15] and designated as nozzle types 3.00 80 A and 1.50 80 B. Their basic design is shown in figure 4.1

Clean, demineralized water was used as a working fluid.

4.1.1 Supply System

The flow rate through domestic oil burner nozzles is very low; typically of order $10^{-6}\,m^3/s$. Thus, an experimental system may be easily operated on a batch basis, with a small water supply tank. The arrangement of the supply system is shown in figure 4.2.

Water in a storage tank was put under pressure using compressed air from the lab supply system, controlled by a regulator. The volume of the air blanket in the top of the tank prevented pressure surging, and no pressure drift was observed during the experiments.

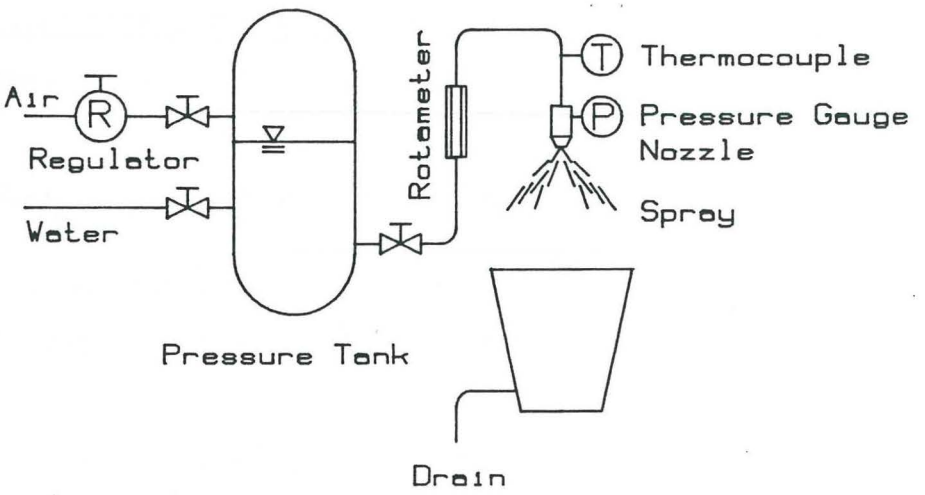

Figure 4.2: Schematic of spray flow supply system.

The water was fed from the tank to the nozzle assembly through flexible plastic hose, with control valves as indicated. The valves were used only in an on/off manner, so that the flow was governed by the tank pressure. Water temperature was measured near the nozzle assembly using a thermocouple and digital thermometer.

The nozzle assembly was composed of a Delavan nozzle adapter which would accept either nozzle, various pipe fittings and a pressure gauge to determine the supply pressure at the nozzle. The gauge was manufactured by US Gauge and graduated from 0 to 100 psi (approximately 0 to 700 kPa). The same gauge was used for both sets of experiments, and was observed to give repeatable results. The pressure measurements are used only to identify the different flow conditions and do not enter into the measurements or the model in a quantitative way.

There were minor variations between the supply systems used at the Lehrstuhl für Strömungsmechanik and at the University of Waterloo. The differences are detailed in the

following sections. Note that the same physical nozzles and pressure gauge were used at both locations.

System Used at the Lehrstuhl für Strömungsmechanik

The spray was supplied from a stainless steel tank of approximately 1 m^3 capacity. The tank was never operated at more than 3/4 full, so that a substantial air cushion was always present.

The nozzle assembly was mounted to a 0.50 m section of 1/4 inch pipe (9.2 mm inside diameter, 13.7 mm outside diameter). This in turn was fixed to the bed of a three dimensional traversing mechanism. Displacement gauges with 10^{-5} m graduations were fixed to the wall, so that the location of the traversing rig could be measured. The sensitivity of both the traversing mechanism and the displacement gauges provided positional accuracy much tighter than the dimensions of the sampling volume of the instrument.

System Used at University of Waterloo

The spray was supplied from a galvanized steel tank of approximately 0.1 m^3 capacity. The tank was never operated at more than 3/4 full, so that a substantial air cushion was always present. The nozzle assembly was clamped in a retort stand with no provision for traversing.

A rotameter was included in the system for the measurement of flow rate under different conditions. The meter was an SK type 1875 "LO-FLO" rotameter with 1/4 - 15 - G tube and 316 stainless steel float. Calibration was made using a mass reference technique. For each calibration data point the meter was read, and the resulting flow collected in a beaker. The mass of water collected and the length of time taken to collect it then give the mass

flow rate for a particular meter reading. A quadratic was fitted to the data using a least squares technique.

$$\dot{m} = -0.2968 + 0.3125X + 0.01138X^2 \tag{4.1}$$

This fit provides the mass flow in g/s as a function of the meter reading X. For flow rates between 0.5 and 2.5 g/s the error was estimated to be less than ± 0.04 g/s so that the maximum error in the flow rate measurements is $\pm 8\%$.

4.2 Photographic Measurements

Photographs of the sprays from each of the nozzles were taken to permit rough measurements of some parameters, as input for the model.

4.2.1 Arrangement of Photographic Equipment

The photographic equipment was arranged as shown in figure 4.3. The spray was illuminated using a mercury flash lamp connected to a microflash unit. This produced a flash pulse of less than 1 μs duration, which virtually froze the spray image.

A 35 mm Pentax camera was used, with a 90 to 250 mm zoom lens and a combination of extension tubes 175 mm long. This combination provided a film image that was slightly larger than the actual size of the spray, so that when printed on 100 by 150 mm paper the image is 4.5 times true size.

The camera was set horizontally, with the lens axis perpendicular to the axis of the flow. The flash lamp was placed on the opposite side of the spray from the camera, slightly off the lens axis both downward and to the left, as viewed through the lens. This geometry

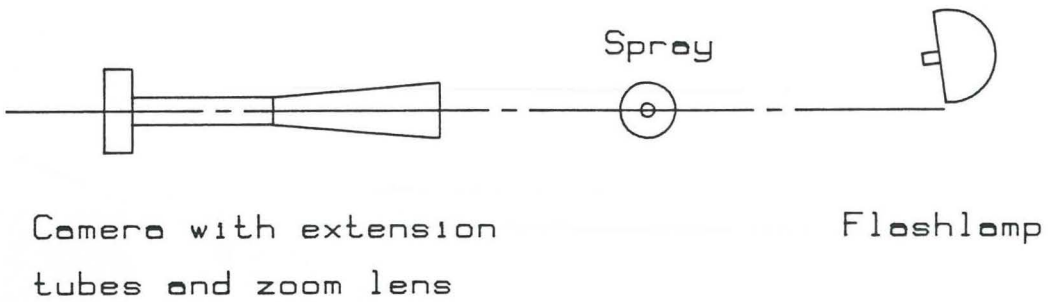

Figure 4.3: Schematic of photographic setup. This figure shows the arrangement of the photographic equipment, as seen from above. The camera was oriented horizontally, with the flash lamp situated slightly off axis and below camera level.

was established by trial and error to eliminate reflections from the inside of the extension tubes, while still maintaining adequate illumination.

Ilford XP1 film was exposed at $f8$ and the X flash setting (approximately 1/50 of a second). With the lab lights dimmed there was no visible effect from light other than the flash illumination. This is confirmed by the fact that frames where the flash failed to fire are completely blank.

4.2.2 Analysis of Photographs

One roll of film ($\sim$ 36 exposures) was shot for each of the six different conditions. The features of the undulating sheet shown in figure 4.4 were measured using a scale and protractor on the 4.5:1 scale prints. Measurements of breakup length, undulation wavelength and amplitude were made for each side of the sheet visible in profile. Those photographs where the undulations could not be distinguished were ignored. Figure 4.5 shows an example of the measurement technique, as applied to an actual photograph.

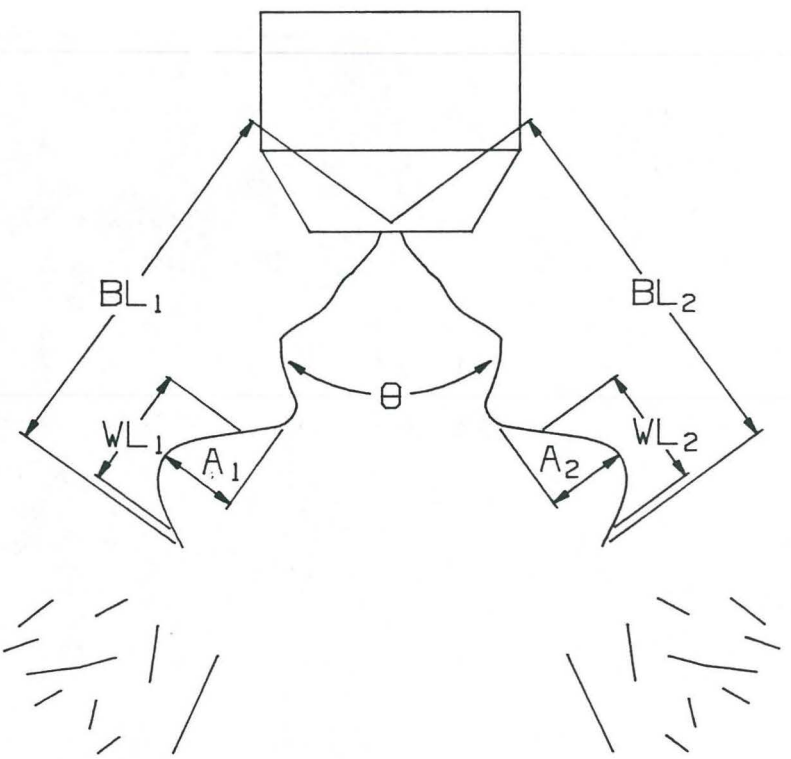

Figure 4.4: Quantities measured from spray photographs. This figure defines the geometrical quantities measured from the photographs. The results of these measurements are tabulated in table 5.1.

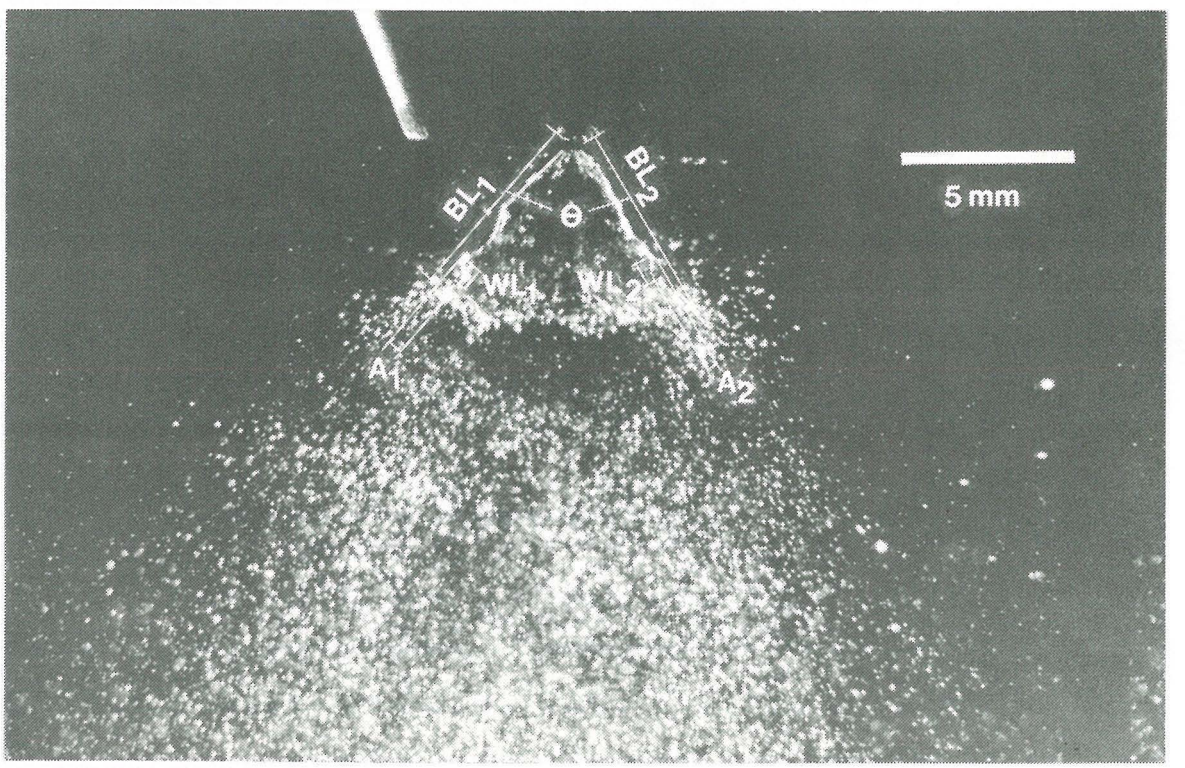

Figure 4.5: Sample photographic measurement. This photograph gives an example of the measurement process. The measured quantities are indicated in white.

The difficulty in recognizing and segregating the sheet features leads to high uncertainty in the results of these measurements. The best indicator of the magnitude of error is provided by the results in table 5.1. Although this flow is axi-symmetric, the average values for quantities measured on opposite sides of the spray differ by as much as 44% for the undulation amplitude. The figures for breakup length and undulation wavelength are in

better agreement from side to side, but it is clear that these values must be used with caution.

4.3 Drop Size and Velocity Instrumentation

There are various techniques available for taking simultaneous measurements of drop size and velocity. The simplest method is double flash photography. Two exposures are made in quick succession, freezing the spray at two points slightly separated in time. Drop sizes are measured directly from the photograph, while velocities are obtained by measuring the distance travelled by each drop in the short time between exposures. This type of measurement is very tedious, thus it is not feasible for taking substantial volumes of data. In addition, this method makes it difficult to take truly local measurements, and problems with depth of field can introduce errors in drop sizing. For these reasons, this method has been largely replaced by laser based optical techniques.

The Malvern Instrument [16,17,18,19] uses small angle diffraction theory to analyze the scattered light from a single laser beam. This results in a PDF for the drop size in the volume of the beam. This instrument has been widely used to obtain data on the characteristics of various atomizers. For further details on the theory and application of the Malvern see Breña de la Rosa's [20] work on unconfined spray flames. Although this instrument is available at Waterloo, it provides only a drop size distribution with no information on drop velocities. For complete data further instrumentation would be necessary.

Several techniques have been developed based on extensions of the basic laser doppler anemometry (LDA) systems used in single phase flows. The drops in the spray make excellent scattering particles, so it is possible to obtain drop velocities from conventional LDA practices. The system must then be extended to simultaneously measure some indicator

of particle size. Analysis of light scattering from particles yields a variety of signals that are in some way dependent on particle size, notably the intensity of scattered light and the modulation visibility of the signal. However, the complex nature of these signals makes it difficult to extract the information, and calibration is crucial, as any amplification or attenuation of the signal affects these amplitude based measurements. Timmerman [21] describes the development and testing of an instrument based on the visibility technique. Durst [22] and Chigier [23] both provide reviews of LDA based measurement techniques.

4.3.1 The Phase / Doppler Technique

Durst and Zare [24] have shown that the phase angle of a doppler burst from a particle varies, depending on the position at which the signal is collected and the size of the particle. If light scattered from a spherical particle is collected at two different places in space, the phase difference between the signals will be directly proportional to the size of the particle. The theory and application of this technique are described by several authors. See, for example, references [25,26,27,28,29]. The theoretical relations are developed using the principles of geometric optics. The resulting equations may then be tested, at specific operating points, using the more exact Mie scattering theory. Bachalo and Houser [25] have shown that the calculations based on geometric optics are in agreement with the Mie theory for water drops as small as three microns. At least two instruments based on this technique are commercially available, one from Aerometrics, Inc. [30] and one from Dantec Elektronik [31].

A major advantage of the phase-doppler technique lies in the nature of the signal. Rather than extracting information from the amplitude of a signal, the information is carried by the phase and frequency. Because of this the technique is insensitive to attenuating or amplifying influences in the system. In addition, the theory is sufficiently complete that

calibration of the instrument is not required. There are no unknown constants to be found.

4.3.2 Phase / Doppler Measurement Relations

A Phase / Doppler system uses the same arrangement of transmitting optics as a standard LDA system, with laser beams crossing at some angle θ. One or both of the beams may have some frequency shift to allow detection of negative velocities, as in standard LDA practice. Two photodetectors are located as indicated in figure 4.7. ϕ is the off-axis scattering, angle measured as a deviation from full forward scatter, and ψ is the elevation angle of the detectors above and below the measurement plane. The size, δ, of a spherical drop is then related to the signal phase shift Φ by

$$\delta = \frac{\lambda \Phi}{2\Delta \pi n_c}, \tag{4.2}$$

where λ is the laser wavelength in vacuum, n_c is the refractive index of the continuous phase and Δ is a function of the optical geometry of the system [28]. For ψ in the region around 70 degrees, transparent drops in a continuous gas phase scatter light almost exclusively by refraction and

$$\begin{aligned} \Delta \;=\; 2 \Bigg(& \left(1 + n'^2 - n'\sqrt{2} \left(1 + \sin\frac{\theta}{2} \sin\psi + \cos\frac{\theta}{2} \cos\psi \cos\phi \right)^{\frac{1}{2}} \right)^{\frac{1}{2}} \\ & - \left(1 + n'^2 - n'\sqrt{2} \left(1 - \sin\frac{\theta}{2} \sin\psi + \cos\frac{\theta}{2} \cos\psi \cos\phi \right)^{\frac{1}{2}} \right)^{\frac{1}{2}} \Bigg) \end{aligned} \tag{4.3}$$

where $n' \equiv n_d/n_c$ is the ratio of refractive index of the dispersed liquid phase to that of the continuous gas phase.

With only two detectors, there may be some ambiguity in the phase shift. For instance, it is impossible to tell the difference between some small phase shift and one that is 2π,

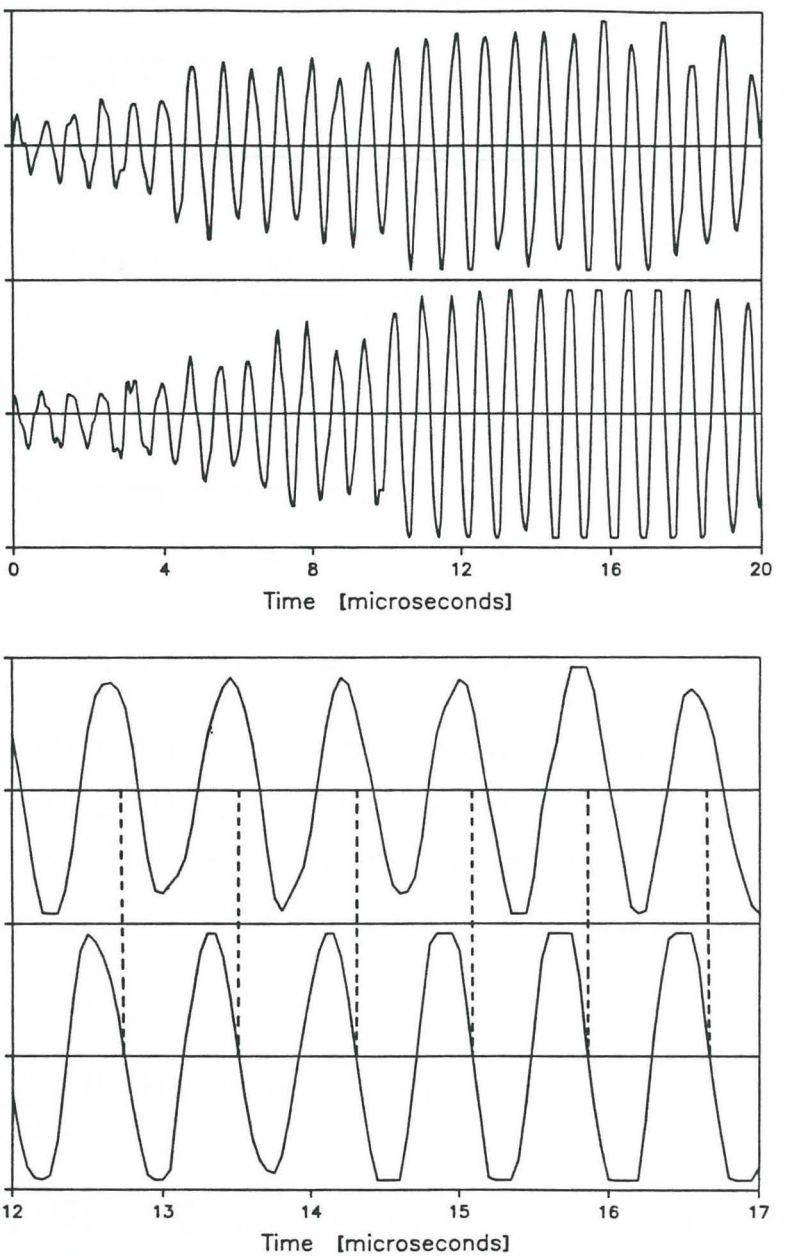

Figure 4.6: Typical signals from a Phase / Doppler system. The upper graph shows the onset of the burst, with traces for each of the channels. The lower graph shows a small section of the upper graph, enlarged to show the phase difference between signals.

or 4π larger. Although it was unnecessary in this work, this ambiguity can be resolved by introducing additional detectors to check the phase shift.

4.4 Phase / Doppler Experimental Apparatus

The measurements that form part of this thesis were made using a Phase / Doppler rig assembled by the author at LSTM in Erlangen. The rig is described in three parts, the optical sending system, the optical receiving system and the signal processing hardware and software. Error analysis and testing of the system are described in Appendix C.

4.4.1 Sending Optics and Control Volume

The Phase / Doppler system used at LSTM was based on an existing low power HeNe LDA sending system. The general layout of the system is shown in figure 4.7, while the sending optics are detailed in figure 4.8. The components of the sending system were mounted on an aluminum honeycomb optical bench. The system included:

- NEC 15 mW HeNe laser
- plane mirrors in adjustable mounts, allowing the laser to be mounted beside the sending optics.
- a rotating diffraction grating to provide both beam splitting and frequency shift, paired with a lens to make the split beams parallel.
- a 310 mm sending lens to direct the beams across one another inside the spray.

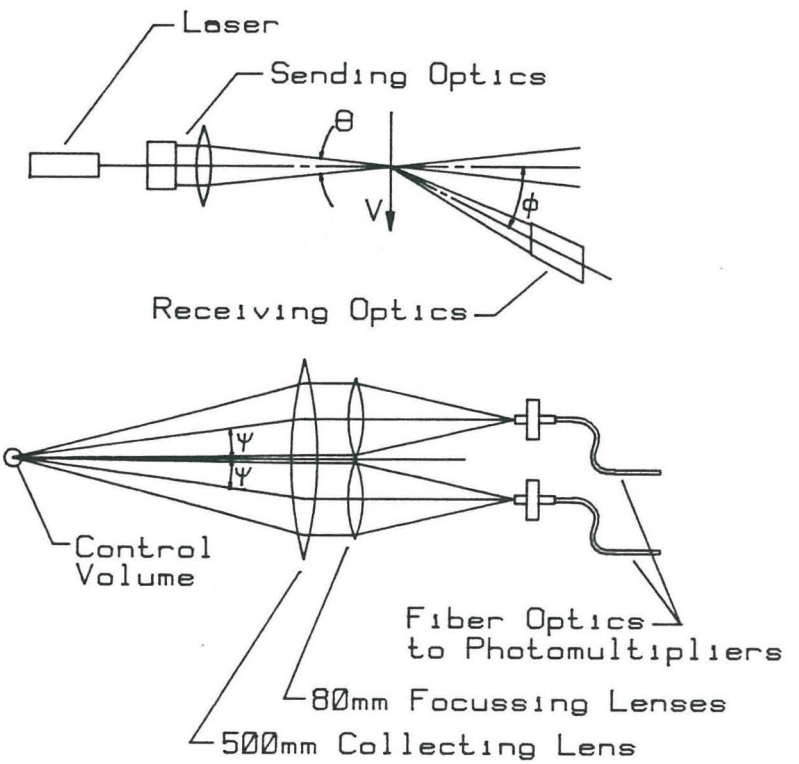

Figure 4.7: Basic Phase / Doppler arrangement and receiving optics. The upper portion of this figure shows the basic arrangement of the system in relation to the velocity component to be measured. The lower drawing shows the receiving optics in detail.

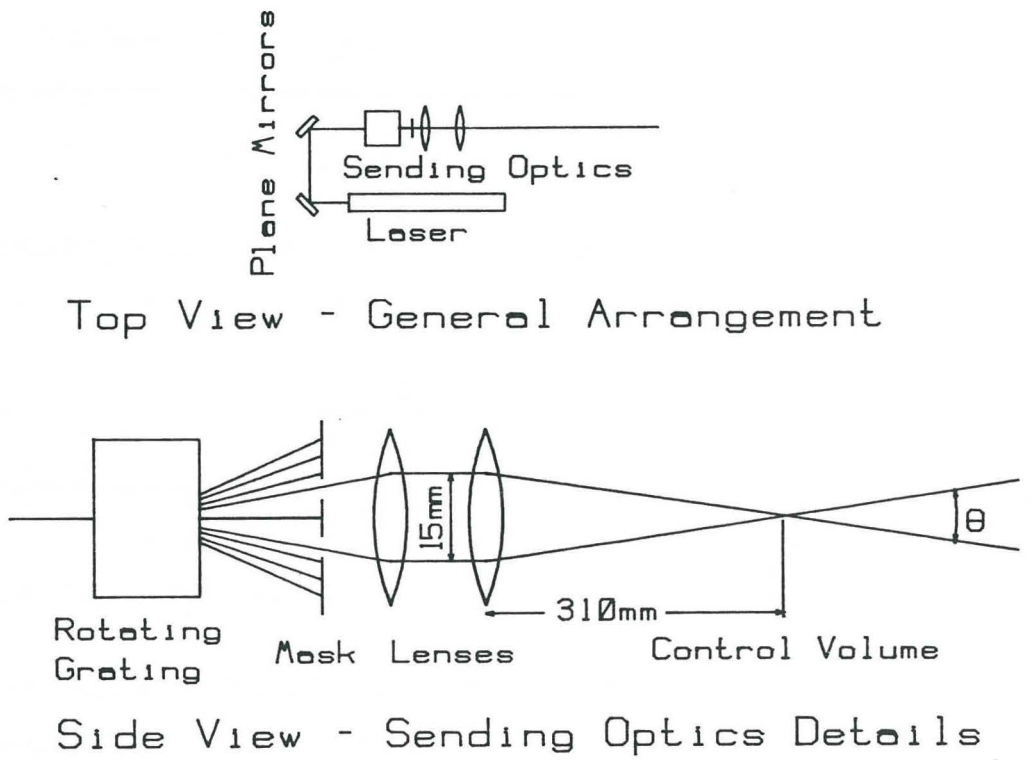

Figure 4.8: Phase / Doppler sending optics.

Table 4.1 gives full details of the system geometry. The control volume features are calculated from equations presented by Durst, Melling and Whitelaw [32] for the crossing of Gaussian profile laser beams. The beam waist diameter is

$$d_s = \frac{5}{\pi}\frac{\lambda f_s}{D} \tag{4.4}$$

where λ is the laser wavelength, f_s is the focal length of the sending lens and D is the initial laser beam diameter. When two such beams cross

$$l_m = \frac{d_s}{\sin(\theta/2)} \qquad \text{and} \qquad d_m = \frac{d_s}{\cos(\theta/2)} \tag{4.5}$$

give the length and diameter, respectively, of the measurement volume. The Doppler difference frequency, ν_D, is related to the perpendicular velocity, $U_\perp$, of the particle producing the signal by

$$\nu_D = \frac{2U_\perp \sin(\theta/2)}{\lambda} + \text{frequency shift.} \tag{4.6}$$

The phase angle conversion factor is calculated from equations 4.2 and 4.3.

4.4.2 Receiving Optics

The detailed arrangement of the receiving optics is shown in figure 4.7. The receiving system is composed of

- a 500 mm focal length receiving lens, approximately 100 mm in diameter.
- two 80 mm focal length lenses, 40 mm in diameter.
- two multi-mode, Phillips F&G fiber optic cables, in adjustable mounts.
- an optical rail and other hardware to support the components and maintain their orientation.

Laser Wavelength	λ	632.8	nm
Beam Diameter	D	1.10	mm
Beam Separation	x_s	15.0	mm
Sending Lens Focal Length	f_s	310	mm
Beam Crossing Angle	$\theta = 2\tan^{-1}(x_s/2f_s)$	2.77°	
Control Volume Length	l_m	11.7	mm
Control Volume Diameter	d_m	0.28	mm
Velocity / Frequency Factor		13.08	(m/s) / MHz
Scattering Angle	ϕ	70°	back from forward scatter
Receiving Lens Focal Length	f_r	500	mm
Receiver Separation	x_r	40.0	mm
Receiver Elevation Angle	$\psi = \tan^{-1}(x_r/2f_r)$	2.29°	
Refractive Index Ratio	$n' = n_{water}/n_{air}$	1.33	
Phase / Diameter Factor		1.16	degrees/μm

Table 4.1: Phase / Doppler system geometry and conversion factors.

The large receiving lens is placed at its focal length, 500 mm, from the control volume so that it collects the light scattered from the control volume and transforms it into a parallel beam. The two small lenses then collect light from different parts of this parallel beam, focussing that light on the receiving apertures of the two fiber optic cables.

The fiber optics transfer the light from the receiving optics to two photo-multiplier tubes mounted approximately 1 m away. Although fiber optics may introduce problems when used as part of a sending system, there are no particular difficulties when they are used as part of the receiving system. An LDA sending system must deliver highly coherent laser light to produce suitable signals. The variable optical path lengths in multi-mode fibers can reduce coherency, resulting in noisy or spurious signals. In the receiving optics, the Doppler difference frequency is of order 10^6 Hz, as compared to the laser frequency of order 10^{14} Hz. At the MHz level, any small variations in optical path length will not have an important effect on the signal.

4.4.3 Signal Processing – Hardware

The optical signals travel through the fiber optic cables to a pair of photo-multiplier tubes (PMTs). The PMTs convert the optical signal to a voltage signal which is fed to a pair of matched variable band pass filter banks. The filters were set to pass only frequencies between 0.5 MHz and 5 MHz. This eliminates the lower frequency signal pedestal and any high frequency noise from the signal, leaving only the Doppler difference signal, fluctuating about zero. Even though the filter banks and other equipment were matched, an inherent phase lag was found between the channels. Fortunately, this lag was constant, so it could be measured and a simple correction applied. For more detail on this and other elements of the system, see Appendix C.

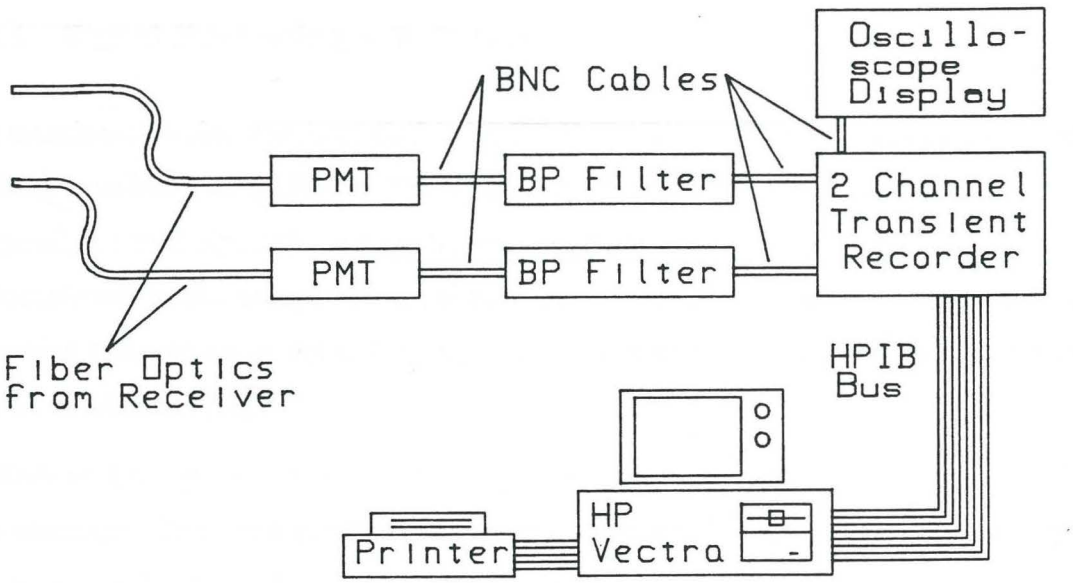

Figure 4.9: Schematic of signal processing hardware.

From the filter banks the signal goes to a two channel transient recorder. From the receiver to the transient recorder, the Phase / Doppler system is identical to a basic LDA system. The only exception is that there are two of each component, forming one path for each of the two signals collected. Until they reach the transient recorder the two signals remain completely separate.

The Datalab DL1080 transient recorder permits recording of 8 bit digital representations of two analog signals, with a maximum sampling rate of 20 MHz. The device is equipped with a level trigger which may be adjusted to detect and record particle events. The trigger level was set to give a balance between rejection rate and bias against low power signals from smaller drops. Some bias was accepted in order to obtain a reasonable rejection rate. See Appendix C for details.

4.4.4 Signal Processing – Software

The transient recorder was connected to an HP Vectra personal computer, using a Hewlett-Packard Interface Bus (HPIB or IEEE-488) interface. When the transient recorder was triggered, it would signal the computer, and the digital data representing that event would be transferred to the computer for processing. The code used for data acquisition and processing was written in the C language. It is not included in this thesis, but is available as part of reference [33].

Each of the signals was analyzed, using a band crossing technique, to find each of the zero crossings. The band crossing method avoids generating spurious multiple counts of zero crossings due to small noise fluctuations in the signal. This technique is illustrated in figure 4.10. When the time of each zero crossing is known the frequency may be estimated, since the time between zero crossings corresponds to half the period of the signal. Similarly, the phase difference between two signals may be determined by comparing the times at which positive going zero crossings occur for each of the separate signals.

After the data for one event were transferred, the transient recorder was rearmed and the entire process repeated; each event being tallied as a part of the distribution. After the desired number of data points had been taken the results were printed in summary, and the tally matrix recorded on disk for future processing.

Signal Verification

The method described above will yield some result for any signal, including system noise. Additional verification tests are required before an event is recorded as valid data. The testing used here verifies that the signal frequencies and phase shift are consistent within the

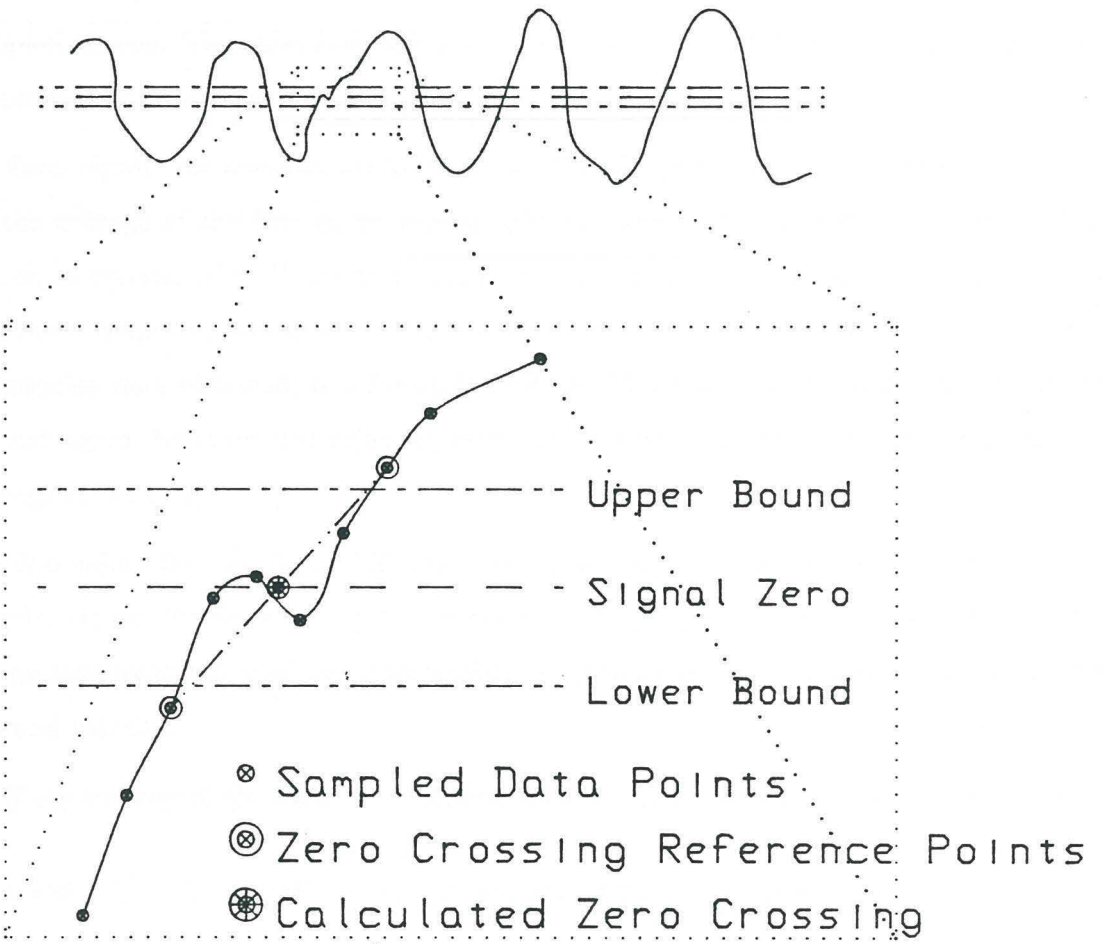

Figure 4.10: Location of zero crossings. This figure graphically illustrates the process used to determine the location of each of the zero crossings in a signal. The lower section of the figure is an enlargement of a small part of the upper section. To qualify as a zero crossing, the signal must pass through a band about zero, so that small glitches in the signal will be ignored. The location of the crossing is then estimated from a linear interpolation between the two points closest to, but outside, the limits of the band.

sampled signals. This effectively eliminates random noise and "garbage" signals produced by multiple scattering or reflections.

Each signal was sampled for 15 periods. Two frequencies were calculated: one based on the average of the first seven wavelengths and the other based on the average of the last eight wavelengths. If the two values did not agree the event was rejected, otherwise an overall frequency was calculated from the average of the two. Thus two self consistent frequencies were obtained, one for each channel. These were then compared, and if they did not agree the event was rejected, otherwise a final frequency was calculated from the average of the two.

Two values for the phase difference were then obtained: one for the first seven wavelengths and one for the next eight. If these did not agree, the event was rejected, otherwise the average frequency and the average phase difference were recorded as indicators of drop size and velocity.

If the two signal channels are represented as A and B, the verification process was:

- test different parts of signal A for self consistency in frequency.
- test different parts of signal B for self consistency in frequency.
- compare the frequencies obtained for A and B for consistency in frequency between signals.
- test the phase difference between signals A and B for consistency at different points in time.

If any one of these tests failed, the event was rejected. The frequencies were tested for agreement to within 4%. The phase shift was tested for agreement to within 1 transient

recorder time step (50 ns). Typical measurements resulted in overall rejection rates of 25 to 40 percent. See reference [33] for details of individual measurements.

4.4.5 Phase / Doppler System Performance

A sample size of 10,000 validated drops was found to give good repeatability on the drop size distribution, however even larger sample sizes were needed to provide reasonable values for mean and variance of velocity. For increasing drop sizes there are fewer and fewer drops within a given drop size range, so the corresponding velocity measurements show large scatter. Due to limitations of time, most measurements were made with a sample size of 10,000 validated drops. Some measurements were made with sample sizes of 20,000 or 30,000 drops for comparison.

The combined hardware / software system described above was able to process approximately 8 to 10 events per second, so that a distribution composed of 10,000 validated events could take over half an hour to obtain. (The 8 to 10 event per second rate includes both validated and rejected events.) The primary bottleneck in the system was the HPIB. Although an HPIB channel is suitable for data transmission rates of up to 250,000 bytes per second, this particular system ran at a data rate of about 10,000 bytes per second. Clearly, a major improvement in performance is available, if a faster interface board and/or software can be installed.

Measurement errors are estimated in Appendix C. With a 95% confidence, the errors are estimated as follows:

- Systematic errors due to uncertainty in system geometry could be as high as $\pm 4\%$ of the measured velocity, and as high as $\pm 3\%$ of the measured drop size. These errors

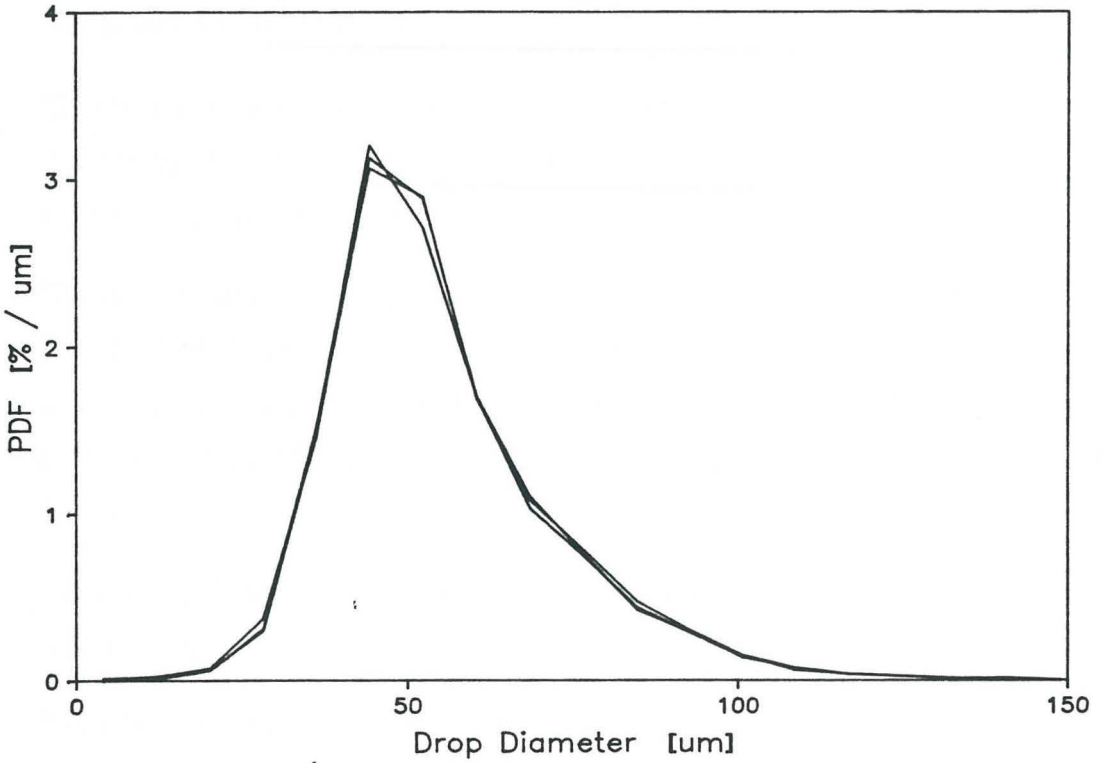

Figure 4.11: Effects of errors on drop size distributions. This figure shows drop size distributions taken under identical conditions, except for the variation in the phase shift validation parameter. Values of 0.5, 1 and 2 were used, so that a fourfold increase in error should be expected. The only differences observed were in the error rates of 47%, 20% and 26% respectively, based on fraction of total events detected. Each distribution is based on a measurement of 10000 verified events. It appears that the actual error in measurement of individual drop sizes is low enough to prevent significant errors in the resulting drop size distributions.

appear as scaling errors, through the conversion factors used to get from frequency and phase angle to velocity and drop size.

- The random error in a single velocity measurement is dependent on the magnitude of the velocity. It varies almost linearly from an error of ± 0.34 m/s at zero velocity to an error of ± 0.59 m/s at a velocity of 16 m/s.

- The random error in a single drop size measurement is also dependent on the drop velocity. This is due to the fact that the phase shift is measured as a time, rather than as a phase angle. The Doppler frequency enters as a multiplier in converting between the two. The estimated error varies linearly from a value of 19 μm at zero velocity to a value of 45 μm at a velocity of 16 m/s.

- There is a systematic bias against drops smaller than about 50 μm due to the trigger level setting.

- There is an ambiguity error in the phase shift, making it impossible to differentiate between very small drops and drops in the range of 310 μm. This manifests itself in the results as a clump of drops with both small diameter and high velocity. These are, in fact, much larger drops. All of the small drops move at slower velocities, very close to the velocity of the surrounding air. This error also has little effect above a drop size of 35 to 50 μm.

The random error in velocity is small when compared with the RMS velocities encountered. The maximum standard error value of 0.29 m/s (half the 95% confidence value) would combine with a typical true RMS velocity of 1 m/s to give a measured RMS of 1.04 m/s. Thus, the measured velocities and their RMS values may be directly compared with the predicted values, without any correction for errors in measurement.

The estimated random error in drop size is very large, and would be expected to strongly influence the results. As discussed in Appendix C, this estimate represents a worst case. Actual errors should be much lower. Figure 4.11 shows drop size distributions taken under the same conditions, but using three different values for the phase shift verification parameter. As there is no substantial variation in the drop size distributions, it appears that the actual error in the drop size measurement is not sufficient to alter the measured drop size distribution.

Chapter 5

Results and Discussion

This chapter presents the results of the experimental procedures described in Chapter 4 and Appendix C, and compares them to the predictions of the physical model described in Chapters 2 and 3.

5.1 Sheet Parameters Obtained Photographically

The results of the photographic measurements are shown in table 5.1. At 207 kPa the "conical" sheet formed by the 1.50 80 B nozzle shows a great deal of inward curvature, primarily due to the effects of surface tension acting around the cone. (See figure 5.1.) Thus it is unrealistic to measure a cone angle for this case. A value of 60° was used in transforming from the perpendicular velocity component of the measurements to the streamwise velocity and back again.

Typical photographs of the sprays produced at different pressures are show in figures 5.1 through 5.3. The difficulty in obtaining accurate values for the sheet parameters should be

	BL_1	BL_2	WL_1	WL_2	A_1	A_2	θ
1.50 80 B							
207 kPa	7.5	7.3	1.1	1.2	0.48	0.48	(60°)
276 kPa	6.4	6.5	1.1	1.2	0.71	0.64	66°
345 kPa	6.1	5.8	1.1	1.2	0.74	0.65	69°
3.00 80 A							
207 kPa	7.4	6.6	1.5	1.4	0.76	0.43	96°
276 kPa	7.7	7.5	1.6	1.5	0.90	0.57	85°
345 kPa	8.1	8.4	1.6	1.6	0.68	0.80	70°

Table 5.1: Results of photographic measurements. This table lists the average values obtained for each of the quantities measured from the photographs. All dimensions are given in mm, except the angle, θ, which is expressed in degrees.

clear from these photographs.

5.1.1 Predictions of Sauter Mean Diameter

Using the photographic information, it is possible to make a crude prediction of the mean drop diameter in the spray. This calculation is similar to that made by Dombrowski and Johns [4]. The mean diameter is obtained by considering the surface to mass ratio, and how it changes as the sheet goes through the transformations of an idealized breakup. Since the calculation is based on the surface to mass ratio, the resulting mean diameter should be compared to the D_{32}, which represents the surface to mass ratio of the spray as a whole.

In the idealized breakup, each half wavelength segment forms a toroidal ligament. Balancing the volume contained in these ligaments against the volume flow rate through the nozzle gives

$$Q = \frac{\pi d_{lig}^2}{4} 2\pi \, BL \, \sin\left(\frac{\theta}{2}\right) \frac{U}{WL}. \tag{5.1}$$

Q is the volume flow rate through the nozzle, obtained from the rotameter measurements. The volume of each ligament is obtained from the cross-sectional area multiplied by the cone circumference at breakup, and U/WL gives the number of ligaments produced per unit time. Rearranging this expression, the diameter of the ligament would be

$$d_{lig} = \sqrt{\frac{2\,WL\,Q}{\pi^2\,U\,BL\,\sin(\theta/2)}}. \tag{5.2}$$

If that ligament then breaks up due to the Rayleigh mechanism, with a most readily amplified disturbance wavelength of 4.508, the estimated drop size is obtained by setting the drop volume equal to the volume of a cylinder, d_{lig} in diameter and $4.508\,d_{lig}$ long.

$$\frac{\pi D_{32}^3}{6} = 4.508\,d_{lig}\frac{\pi d_{lig}^2}{4} \qquad \text{or} \qquad D_{32} = 1.89\,d_{lig} \tag{5.3}$$

The mean large drop velocity, defined in section 5.2.1, is used as an estimate of the perpendicular component of the sheet translational velocity. As with the other modelling, the translational velocity U was estimated from the measured $U_\perp$ values by trigonometry.

$$U = \frac{U_\perp}{\cos(\theta/2)} \tag{5.4}$$

The results of these calculations are shown in table 5.2, along with measured values of the D_{32}. Dombrowski and Johns compare their predicted values to an unspecified mean diameter, presumably either the D_{30} or the D_{32}. They find that the measured mean diameter is typically smaller than the predicted diameter and suggest a linear relation between them, although the data show substantial scatter. This trend is consistent with the results presented here. Dombrowski and Johns found a constant of proportionality of 0.676. This compares well with 0.71, the average value in these results. This is discussed further in section 5.4.

5.2 Drop Size and Velocity Distributions

The drop size and velocity distributions obtained using the Phase / Doppler technique all showed similar characteristics. Six individual measurements have been chosen as a representative sample; one for each of the two nozzles, at each of three operating pressures. These joint drop size and velocity distributions are shown as surface plots in figures 5.4 through 5.9. The same results are presented in a different form in figures 5.11 through 5.16, where they are compared with the output from the model. For experimental references, the dimension y is measured along the nozzle axis, with $y = 0$ at the face of the nozzle. The dimension x is the radial distance from the nozzle axis.

Nozzle and Pressure	Meter Reading	Flow Rate g/s	Flow Rate mm^3/s	$U_\perp$ m/s	U m/s	Ligament Diameter μm	D_{32} predicted μm	D_{32} measured μm
1.50 80 B								
207 kPa	2.8	.667	668	6.56	7.57	74.2	140	111
276 kPa	2.9	.705	706	6.78	8.07	74.8	141	101
345 kPa	3.2	.820	821	7.79	9.45	77.6	147	101
3.00 80 A								
207 kPa	4.4	1.30	1301	7.00	10.5	83.2	157	121
276 kPa	4.85	1.49	1489	8.68	11.8	87.1	165	113
345 kPa	5.15	1.61	1617	10.0	12.2	93.9	178	106

Table 5.2: Estimation of D_{32} from photographic measurements. This table compares photographic estimates of D_{32} with the measured values for each of the different spray conditions.

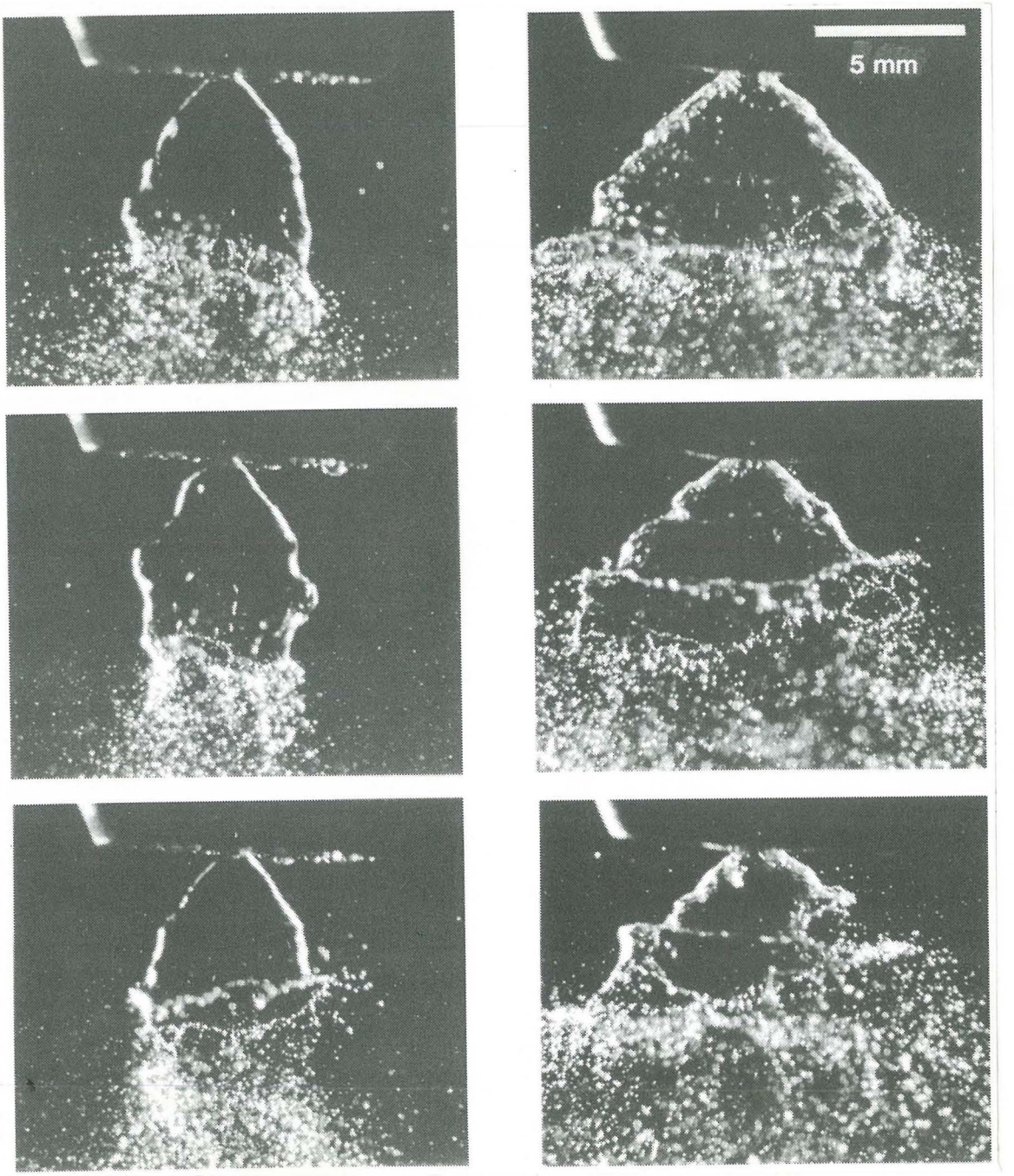

1.50 80 B

3.00 80 A

Figure 5.1: Typical spray photographs 207 kPa.

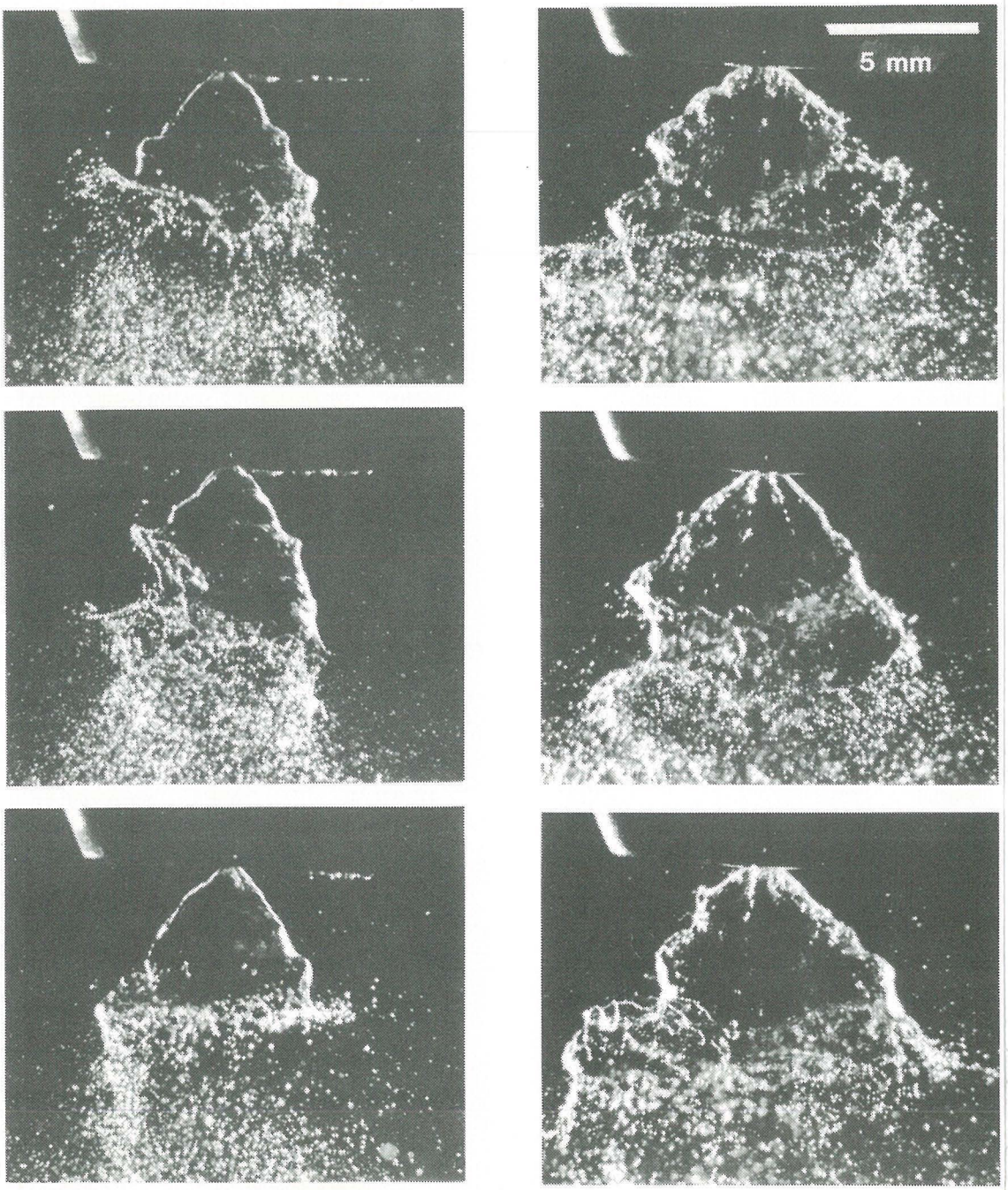

1.50 80 B

3.00 80 A

Figure 5.2: Typical spray photographs 276 kPa.

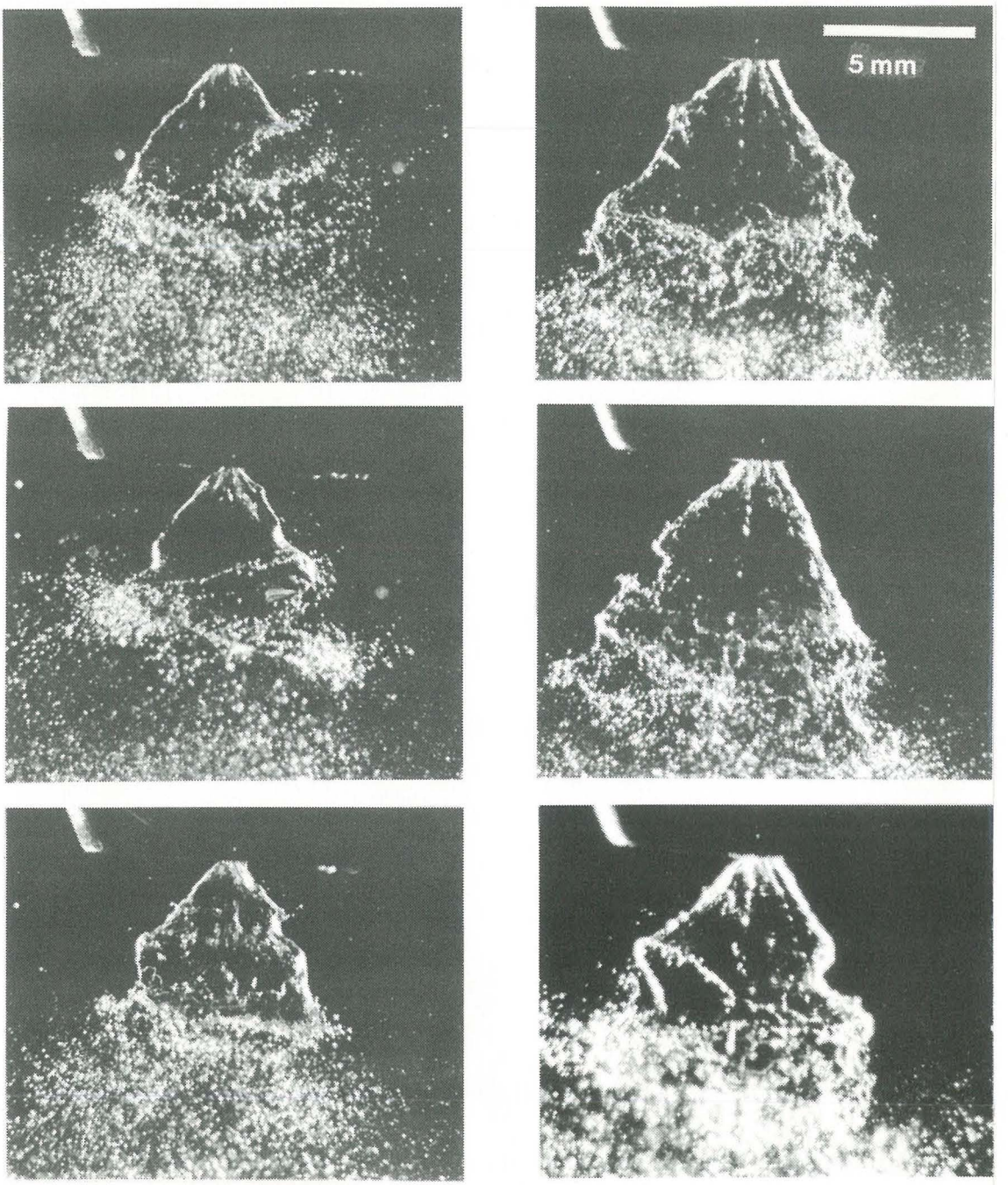

1.50 80 B

3.00 80 A

Figure 5.3: Typical spray photographs 345 kPa.

5.2.1 The Mean Velocity of Large Drops

In all of the measured cases the mean drop velocity seems nearly constant at larger drop sizes. This is also consistent with the model. The larger drops have not yet been affected by aerodynamic drag, and therefore provide a good indicator of the velocities at the point of breakup. In order to quantify this velocity, the mean large drop velocity is defined as the arithmetic mean of the four mean velocity readings covering the range from 120 μm to 160 μm. Figure 5.10 shows the variation in the value of the mean large drop velocity as a function of distance out from the nozzle centerline.

5.3 Model Results

Although the surface plots presented previously provide an overall impression of the data, they are not suitable for making quantitative comparisons. In this section the same data are presented in a different form. Figures 5.11 through 5.16 show the drop size PDF, the mean drop velocity and the variance of the drop velocity, all plotted as a function of drop size. The PDF is dimensionless, expressed as probability per unit δ_*. Both the mean velocity and the variance are plotted in dimensionless form – nondimensionalized with the modelled mean sheet velocity U. The equivalent results from the model are plotted on the same graphs. The model results are plotted with broken lines, while the experimental results are plotted with solid lines. In all cases:

- The drop size distributions are the curves that show a central peak.
- The mean velocity curves show nearly constant values at larger drop sizes, with typical values of $\overline{u}_*$ near 0.8.

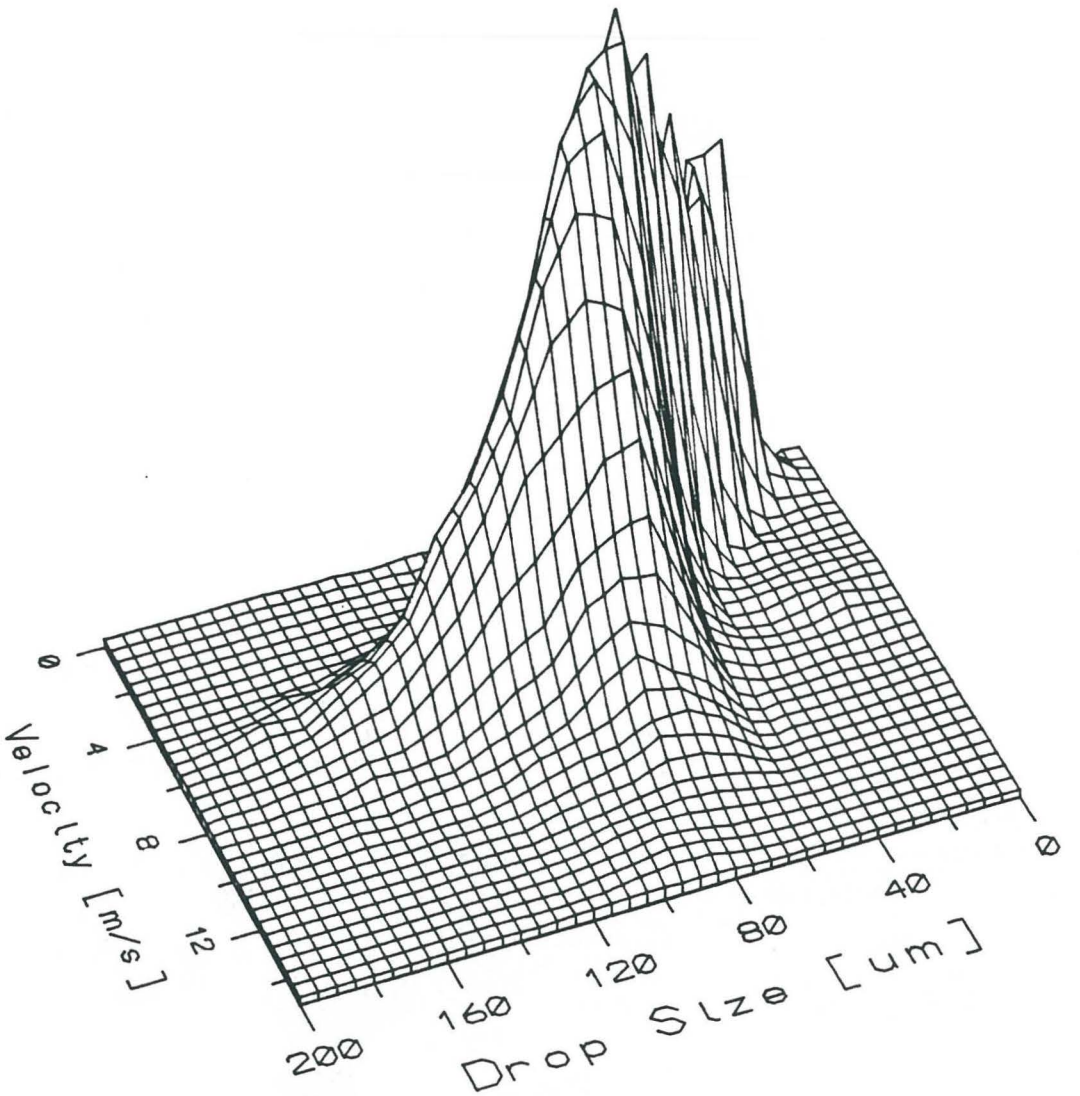

Figure 5.4: Size / Velocity PDF 1.50 80 B 207 kPa $y = 10\,\text{mm}$ $x = 6\,\text{mm}$.

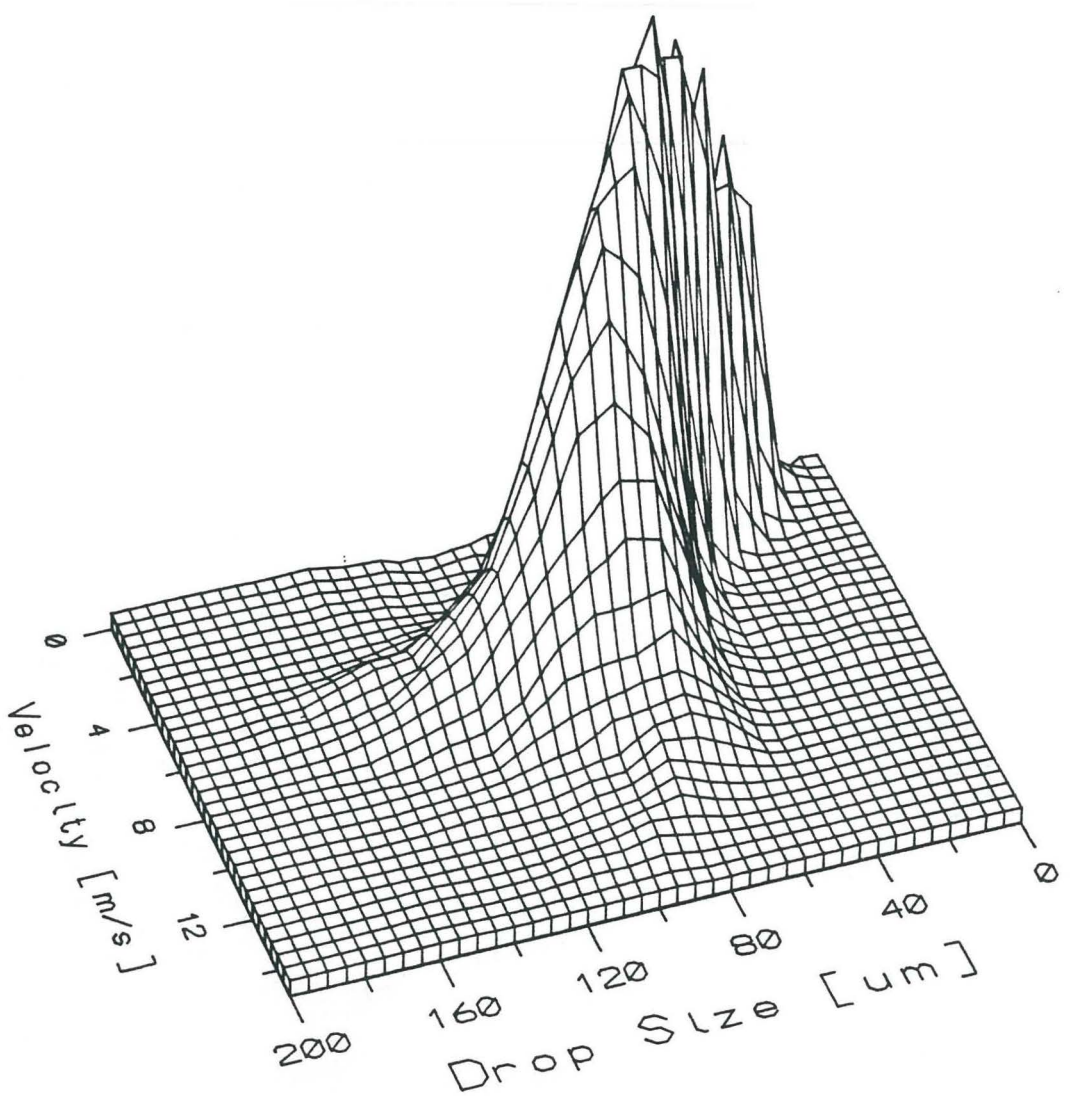

Figure 5.5: Size / Velocity PDF 1.50 80 B 276 kPa $y = 10\,\text{mm}$ $x = 10\,\text{mm}$.

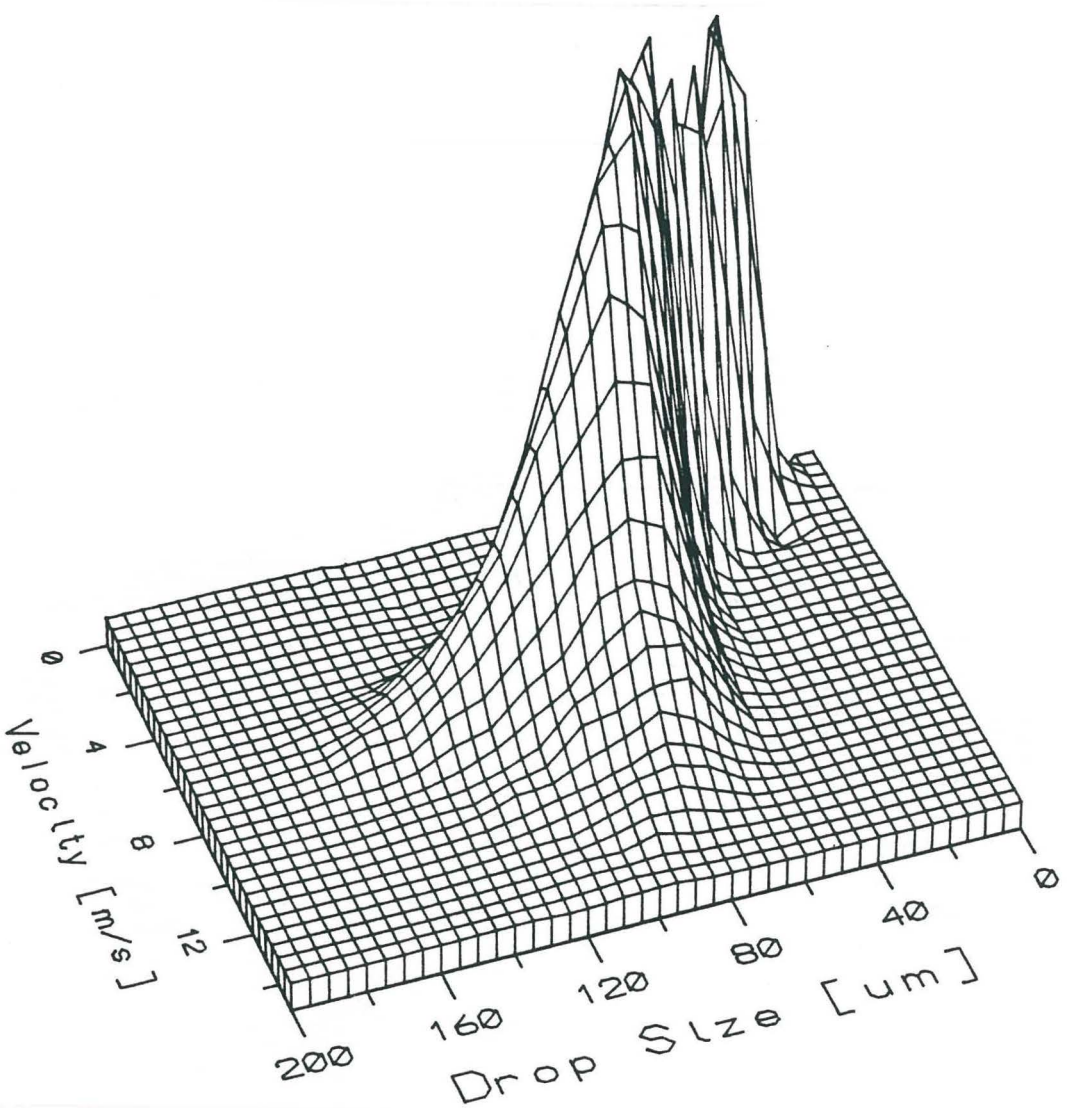

Figure 5.6: Size / Velocity PDF 1.50 80 B 345 kPa $y = 10\,\text{mm}$ $x = 10\,\text{mm}$.

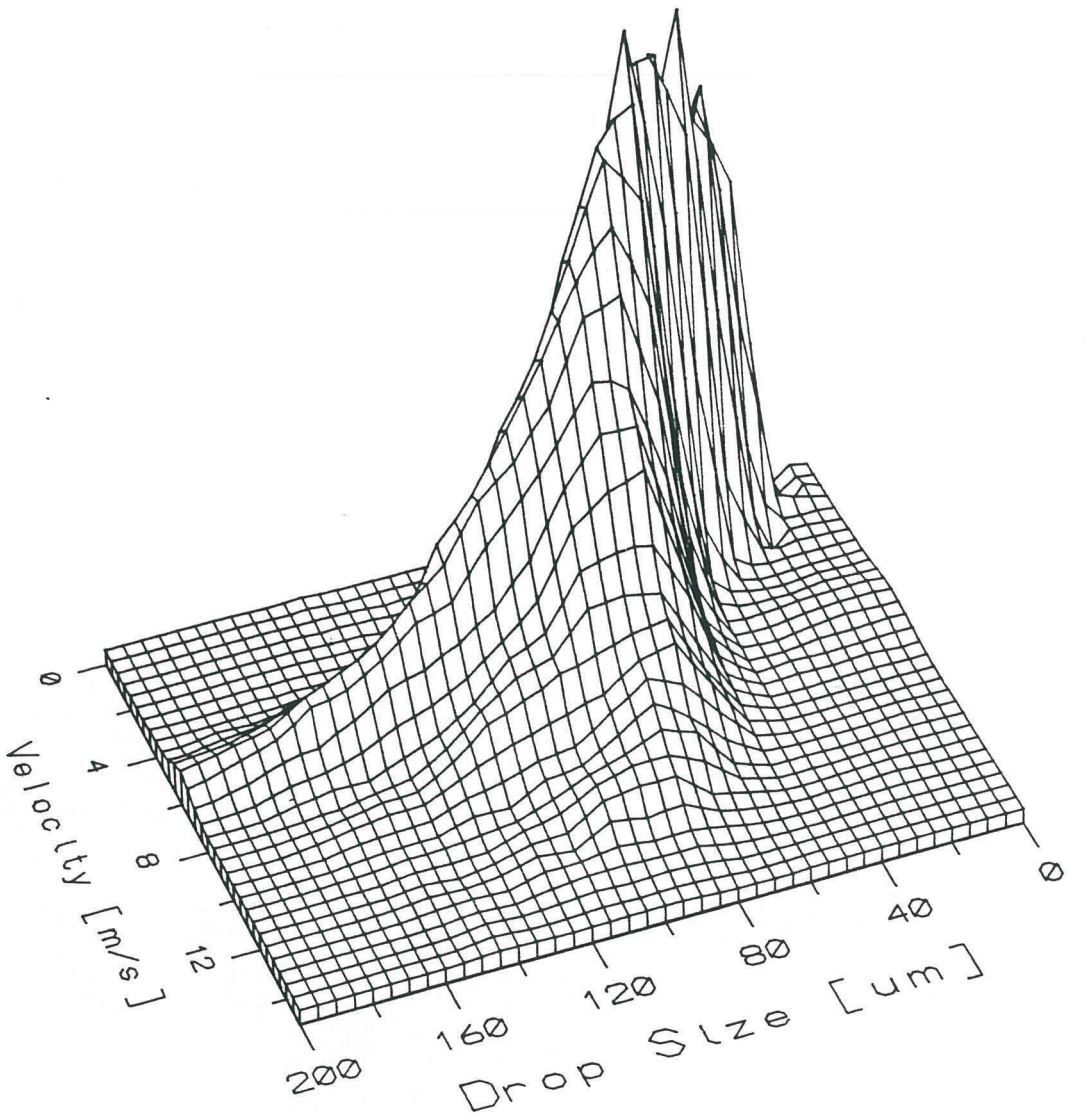

Figure 5.7: Size / Velocity PDF 3.00 80 A 207 kPa $y = 10\,\text{mm}$ $x = 10\,\text{mm}$.

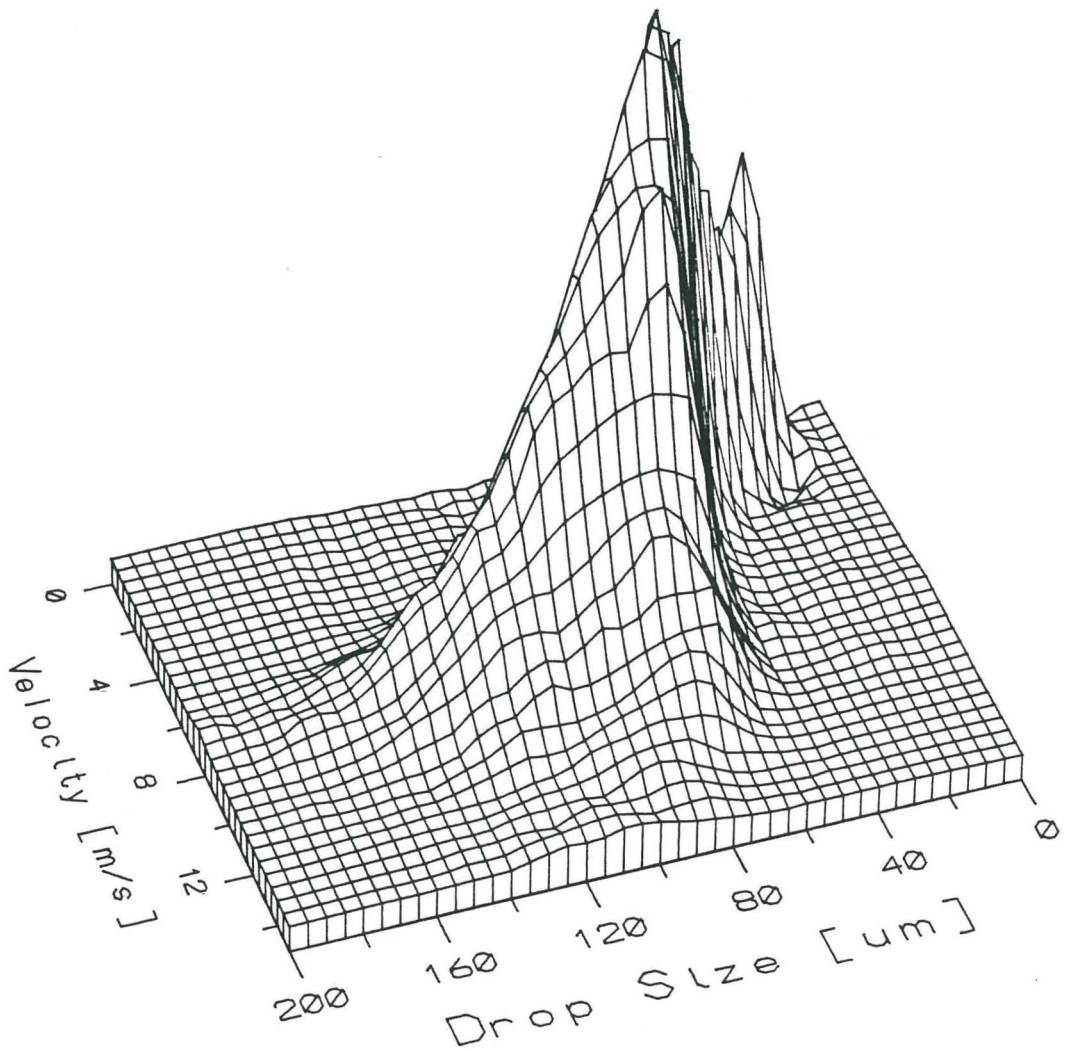

Figure 5.8: Size / Velocity PDF 3.00 80 A 276 kPa $y = 10\,\text{mm}$ $x = 10\,\text{mm}$.

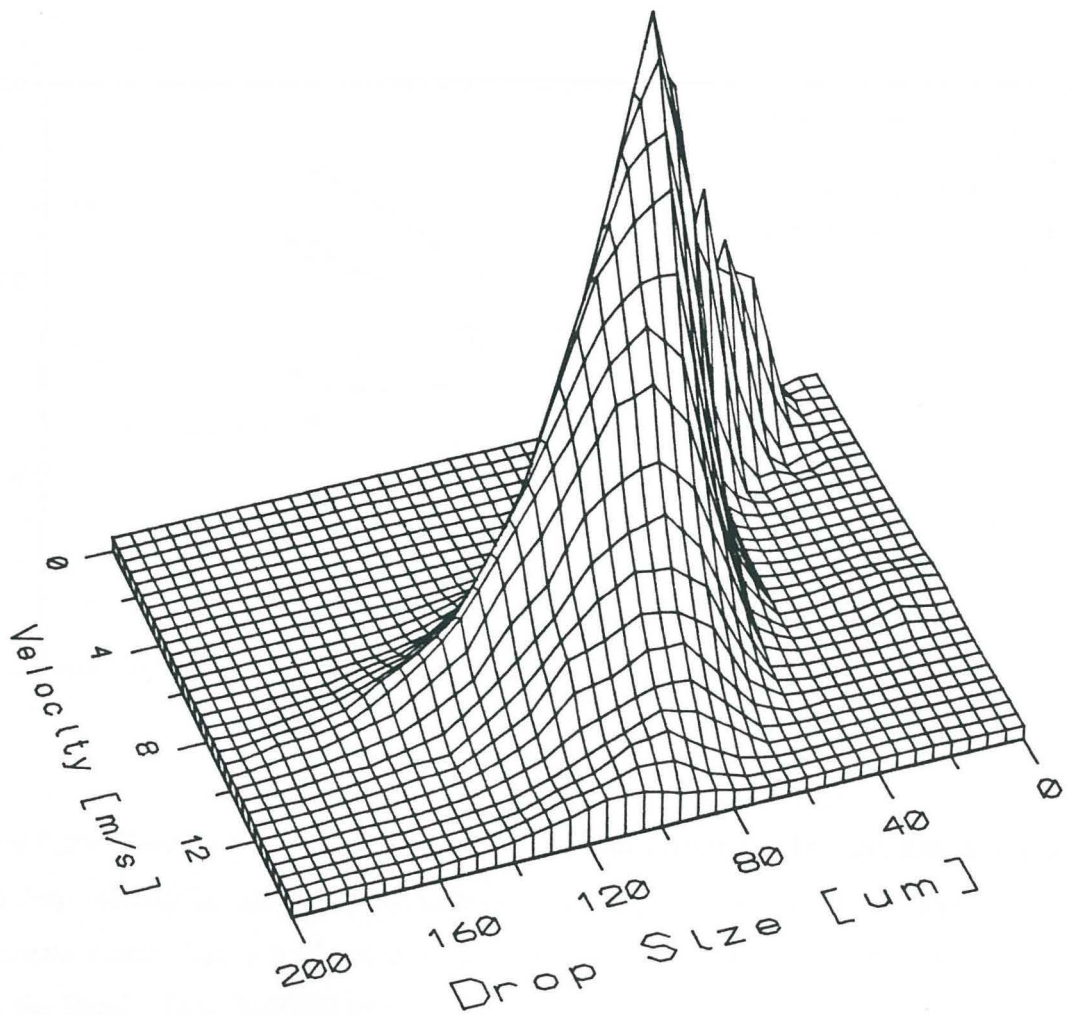

Figure 5.9: Size / Velocity PDF 3.00 80 A 345 kPa $y = 10\,\text{mm}$ $x = 10\,\text{mm}$.

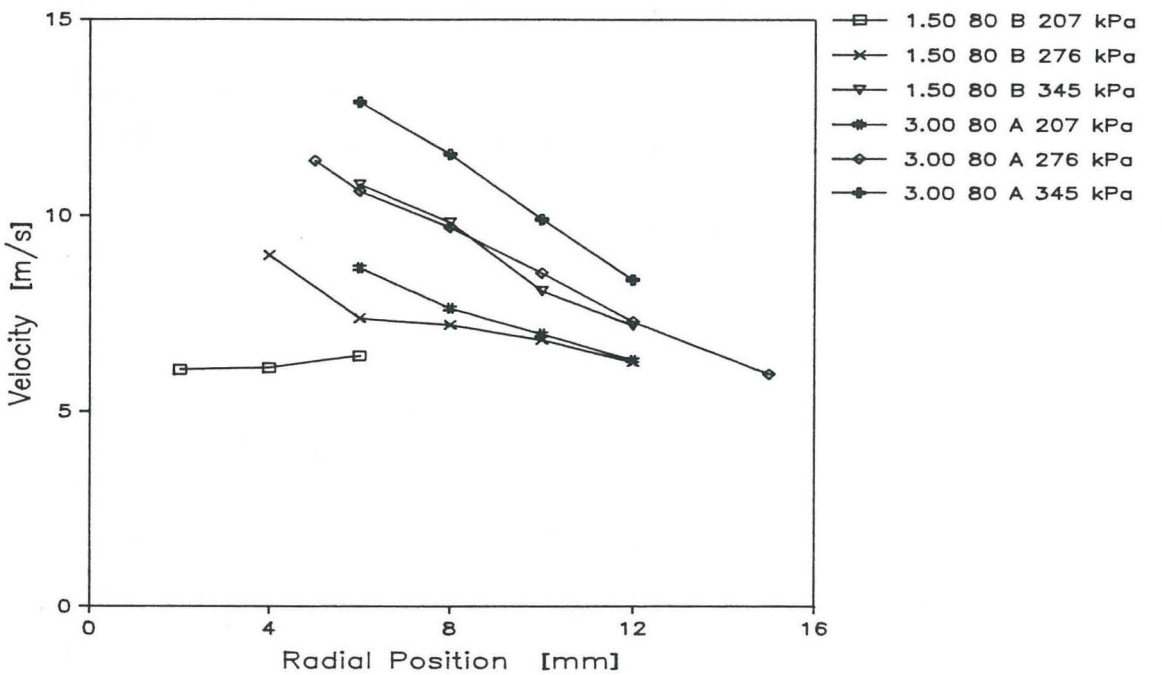

Figure 5.10: Positional variation of mean large drop velocity. This plot shows the mean large drop velocity for each of the six flow conditions, plotted as a function of distance from the nozzle center line. All of the measurements were taken at points 10 mm downstream from the nozzle. ($y = 10$ mm)

- The curves showing variance of velocity decrease towards zero with increasing drop size. They are scaled up by a factor of ten to allow all the information to be displayed on a single plot.

The input for the model was established from the quantities measured in the spray.

- The mean sheet velocity could not be measured in the experimental flow. It is estimated from the measured "large drop" velocities and the angle of the spray cone.
- The undulation wavelength, amplitude and the breakup length are taken directly from the photographic measurements. In each case the mean of the two measured values was used.
- The value used in the surface energy constraint was taken from the spray measurements as the ratio D_{30}/D_{32}.
- A kinetic energy source term was used to obtain agreement with the data. This term accounts for uncertainties in the amplitude measurements, as well as other disruptive processes that were not modelled.
- Appropriate values of the partition coefficient, K_p, were determined by trial and error.

Table 5.3 shows the values used as input to the model.

5.3.1 Velocity Distributions

In addition to the information on mean and variance of velocity presented in the previous sections, the model predicts that the distribution of velocity will be Gaussian in shape. Figure 5.17 shows measured distributions of velocity at different drop sizes. Although

Nozzle and Pressure	U m/s	Breakup Length mm	Wave-length mm	Amplitude mm	D_{30}/D_{32}	K.E. Source J/kg	K_p
1.50 80 B							
207 kPa	7.57	7.40	2.28	0.481	0.852	3.50	1.30
276 kPa	8.07	6.46	2.21	0.677	0.869	3.50	1.30
345 kPa	9.45	5.96	2.31	0.699	0.878	3.50	1.30
3.00 80 A							
207 kPa	10.50	6.98	2.87	0.592	0.827	3.50	1.40
276 kPa	11.77	7.61	3.04	0.735	0.868	4.00	1.30
345 kPa	12.22	8.27	3.13	0.740	0.885	5.50	1.25

Table 5.3: Input parameters for model predictions. This table shows the values used to obtain the model results shown in figures 5.11 through 5.16.

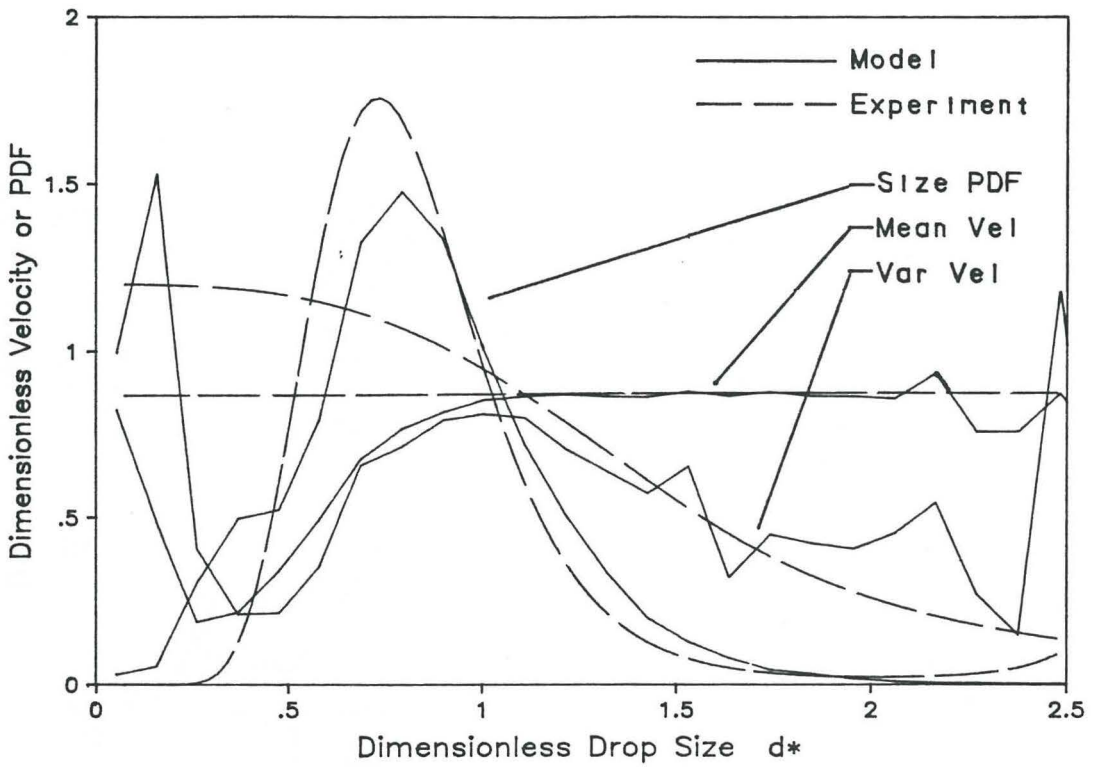

Figure 5.11: Comparison: model vs. experiment 1.50 80 B 207 kPa $y = 10\,\text{mm}$ $x = 6\,\text{mm}$. See the text of section 5.3 for explanation.

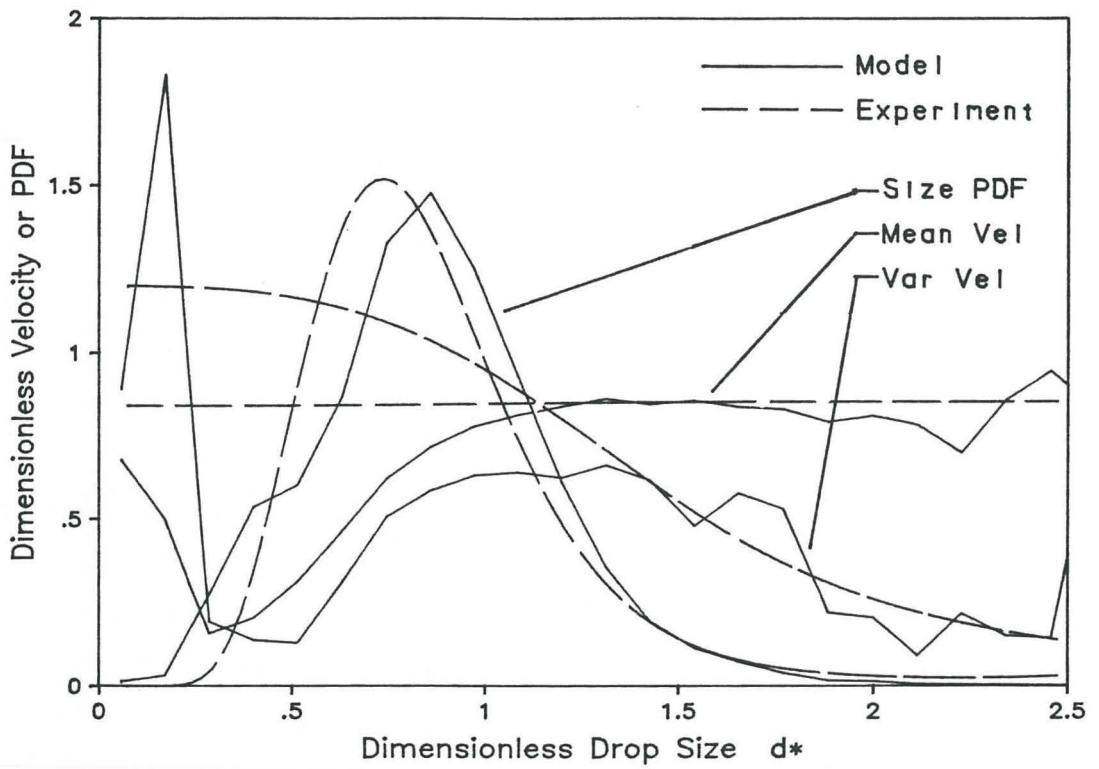

Figure 5.12: Comparison: model vs. experiment 1.50 80 B 276 kPa $y = 10\,\text{mm}$ $x = 10\,\text{mm}$. See the text of section 5.3 for explanation.

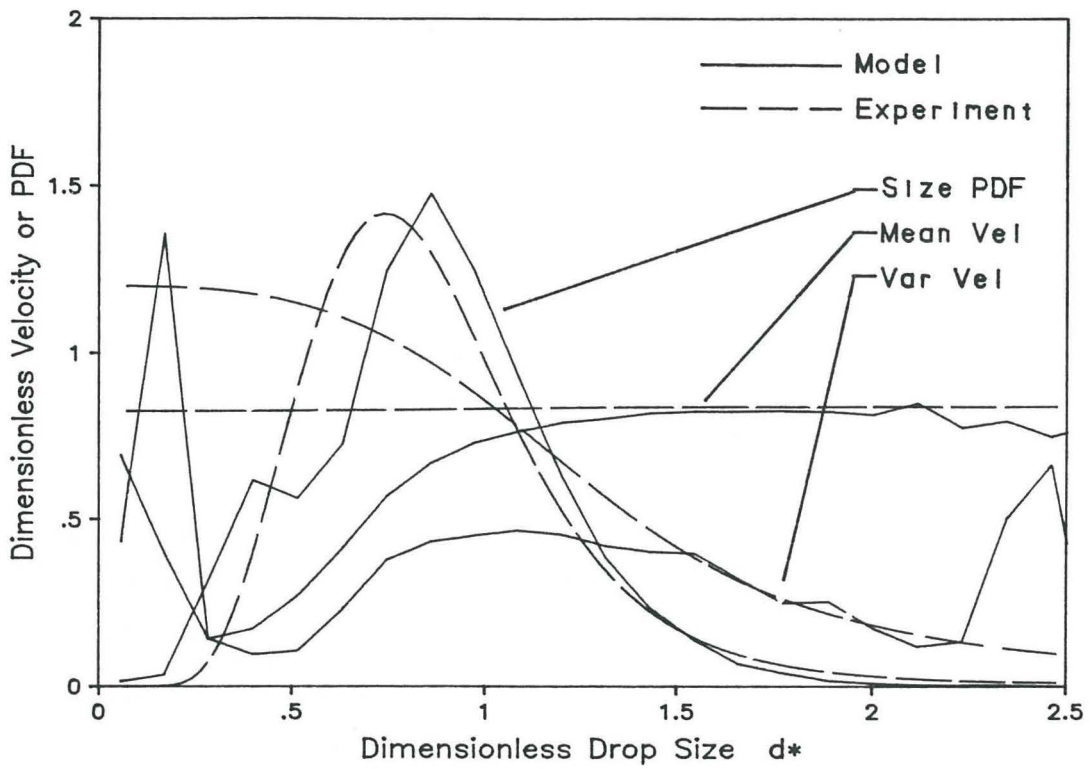

Figure 5.13: Comparison: model vs. experiment 1.50 80 B 345 kPa $y = 10\,\text{mm}$ $x = 10\,\text{mm}$. See the text of section 5.3 for explanation.

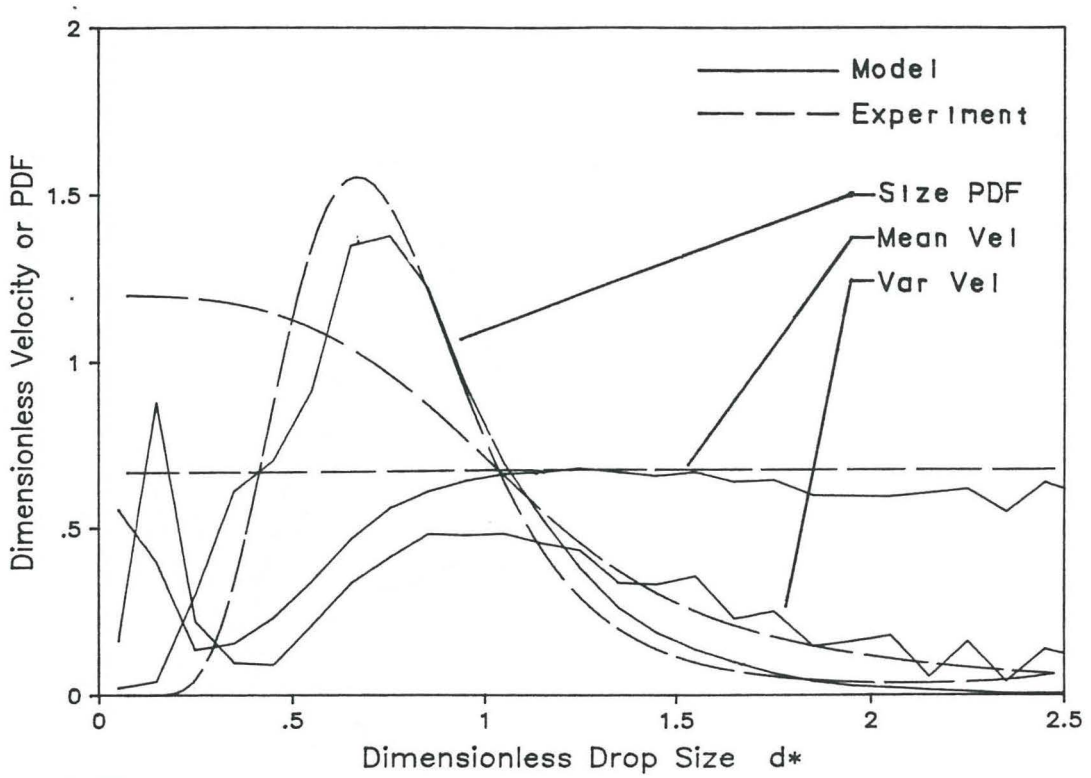

Figure 5.14: Comparison: model vs. experiment 3.00 80 A 207 kPa $y = 10\,\text{mm}$ $x = 10\,\text{mm}$. See the text of section 5.3 for explanation.

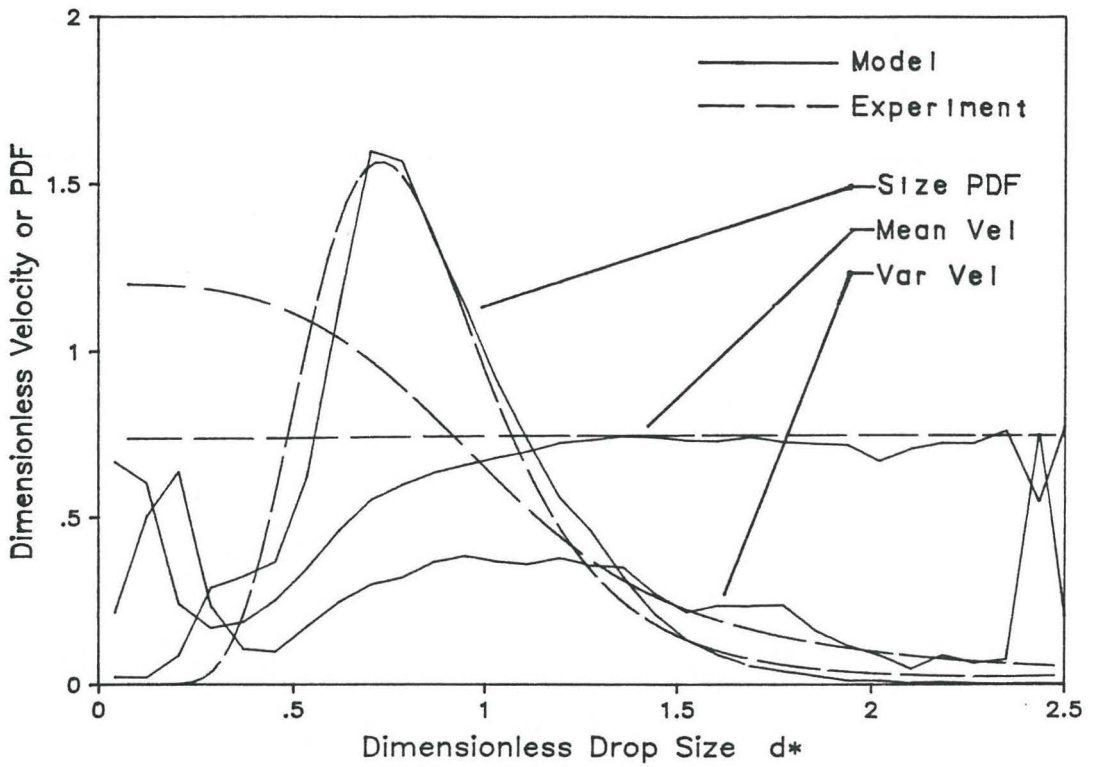

Figure 5.15: Comparison: model vs. experiment 3.00 80 A 276 kPa $y = 10\,\text{mm}$ $x = 10\,\text{mm}$. See the text of section 5.3 for explanation.

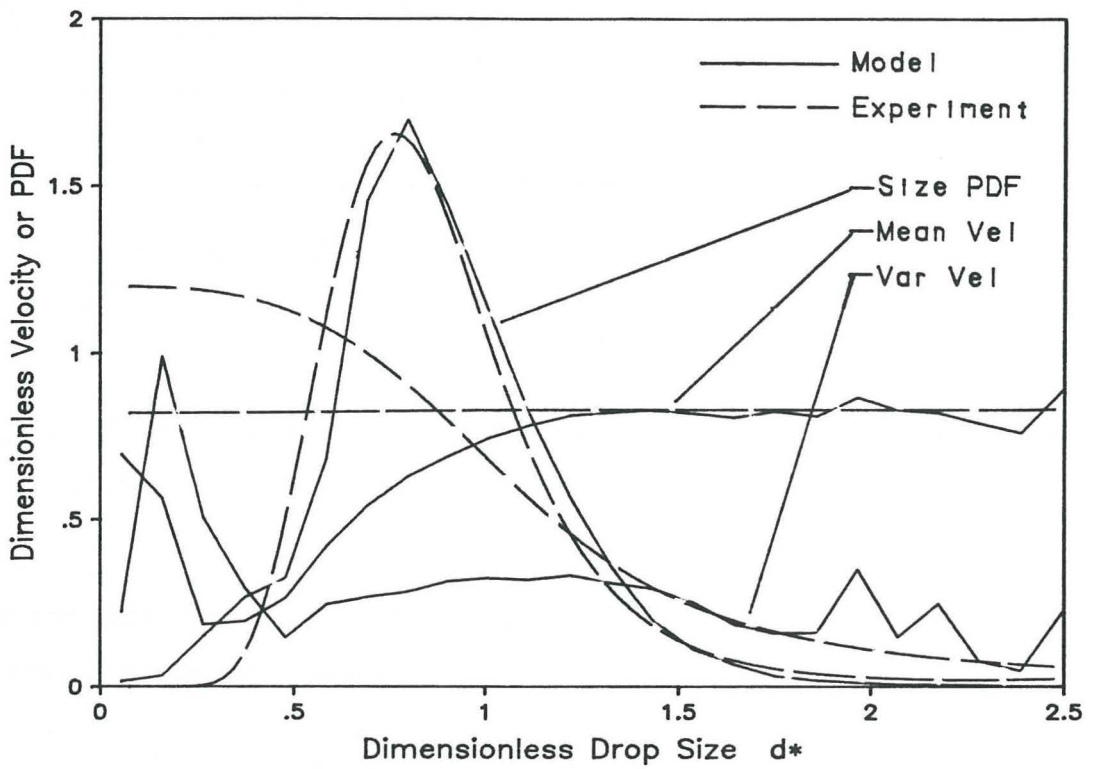

Figure 5.16: Comparison: model vs. experiment 3.00 80 A 345 kPa $y = 10\,\text{mm}$ $x = 10\,\text{mm}$. See the text of section 5.3 for explanation.

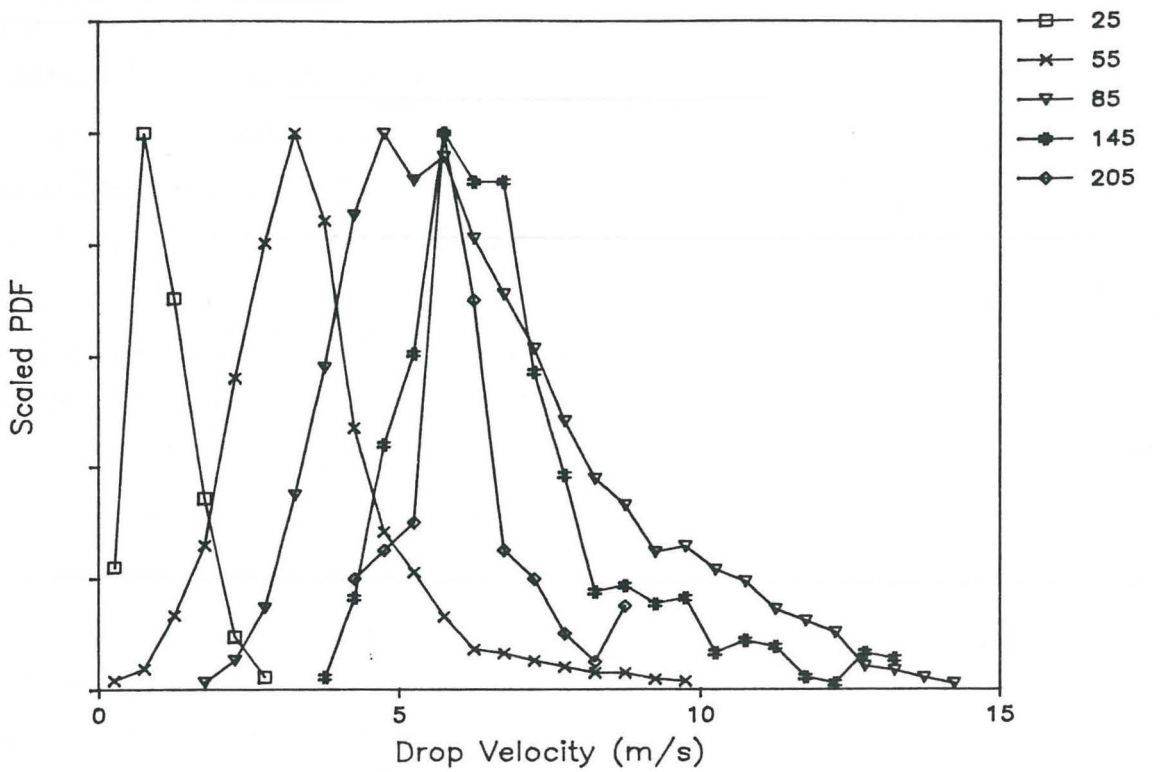

Figure 5.17: Velocity distributions at different drop sizes. These results are for the 3.00 80 A nozzle, operated at 207 kPa. The drop sizes listed in the legend are in μm.

the grid dimensions and sample size prevent a detailed assessment, the shape of these distributions is consistent with the Gaussian prediction.

5.4 Discussion

As is evident from the spray photographs, the measurements of the sheet properties are subject to a large uncertainty. This is amply demonstrated by the discrepancies between

measurements of the same quantities taken from opposite sides of the cone. In this axi-symmetric flow the results should be the same on both sides. Considering the crudeness of both the measurements and the theoretical treatment, the agreement between the D_{32} values is quite good, and the similarity to the results of Dombrowski and Johns [4] is remarkable. The fact that the predicted values are consistently higher than the measured values suggests that there is some additional disruptive mechanism, beyond the model of breakup based on the decay of surface area through contraction of the sheet into ligaments and those ligaments into drops. One would expect this mechanism to have more effect when the relative velocities in the spray are higher. This could explain the opposite trends seen in the D_{32} between the predictions and the measurements.

Comparing the spray photographs to the idealization of the breakup process also suggests additional mechanisms, as the contraction into ligaments is not necessarily completed, and may not include the entire half wavelength segment. Also, small drops break loose from the edges of the sheet as the segments contract, reducing the resulting D_{32}.

All of the measured distributions show basically the same characteristics. At large drop sizes the mean velocity is reasonably constant, while the variance decreases with increasing drop size. As the drop size decreases, both the mean and variance of the velocity start to drop. This is due to the onset of drag effects. Aerodynamic drag affects smaller drops much more strongly than large drops. The effects of drag on the distribution can be clearly seen in the surface plots in figures 5.4 through 5.9, where a sharp, cliff-like portion of the distribution faces towards the region of small size and high velocity. Drag effects have displaced all of the drops from this region of the distribution, forcing them to a lower velocity.

At very low drop sizes, there is some effect due to the phase ambiguity errors which show the signals of very large drops as very small drops as the scale wraps around. In this work

the liquid was sprayed into a quiescent environment, so that the velocity of the surrounding gas stream is much slower than the spray velocity. Due to differences in drag effects, the large drops generally move at much higher velocities than the small drops. This leads to a false increase in the indicated values of both the mean and variance of velocity. This is simply an artifact of the measurement technique, which could be eliminated if an additional detector were added to resolve the phase angle ambiguity. These large drops are visible on the surface plots as a small hill of high velocity drops in the small drop size region.

Contrary to expectation, the mean velocity in the spray was very much dependent on the radial position in the spray. This variation would be expected in the far field, where the effects of entrainment and aerodynamic drag would be more strongly felt. In this region, very close to the nozzle, these effects should not have materially altered the velocities of the larger drops. This expectation is consistent with the form of the drop size and velocity distributions measured, which do not show substantial effects of drag on the larger drops. This variation in velocity must therefore be due to some dynamic effect in the breakup process, such as a "drag" force on the sheet. If this effect takes place before the sheet breaks up into drops, it will not show up as a function of drop size. Only the drag forces that act on individual drops after breakup is complete will show effects that are dependent on drop size. This possibility is consistent with the observed results, but no conclusions may be drawn from this limited information.

Figures 5.11 through 5.16 show very good agreement between the measured and predicted values, except in the smaller drop size range where drag effects have been substantial. The six cases selected from the measured data are a reasonable representation of the overall data. Except for variations in velocity, little difference in results was seen with variation in the radial position. These distributions, taken from the central region of the spray sheet, represent a reasonable estimate of the overall integral distribution function. It is this inte-

gral distribution function that is predicted by the model, which does not account for any local variations.

This good agreement suggests that this model will perform well as a basis for estimating initial conditions in spray flows where complete experimental data is unavailable. However, the detailed information required for input to the model may also be unavailable in these cases. It may be possible to correlate the input parameters with easily obtained experimental variables, as discussed in section 5.4.1. If so, this model would provide an easy to use method of estimating initial conditions in sprays of this type.

Although the results at small drop sizes are suspect due to biasing errors, an interesting discrepancy between the predicted and measured size distributions is evident in all of the cases. There is a "shoulder" present in the measured distributions at a δ_* value of about 0.5. Rather than showing the smooth reduction present in the predicted PDF as it approaches zero, the measured PDF shows more small drops than would be expected. This can be explained by entrainment effects in the spray. The injection of the spray into a quiescent environment induces an air flow in and near the spray cone. The positive velocity at the base of the cone requires an entrainment velocity through the sides of the cone to satisfy continuity. Thus, the air velocity in the developing spray includes a radial component moving inwards towards the axis. This air flow exerts a drag force on the water drops in the spray, accelerating them toward the axis. Because this drag effect is more pronounced on smaller drops, there is a preferential transport of small drops towards the center of the spray cone. The increased incidence of small drops in the measured data could be the result of this transport bringing small drops from the outer edges of the spray in to the more central region where the measurements were made. If an integral measurement was made, covering the complete range of radial position, this effect would average out. The integration would eliminate any observable effects of radial transport.

5.4.1 Distribution Parameters

All of the parameters that go into the physical model are physically meaningful. They represent the physical characteristics of the spray system. However, not all of the parameters can be obtained from an examination of the liquid sheet. Three parameters are obtained from a knowledge of the spray:

- the kinetic energy source term.
- the D_{30}/D_{32} ratio for the surface energy constraint.
- the partition coefficient K_p.

Figures 5.18 through 5.20 show the effects of variation in these parameters. The model solution for the 3.00 80 A nozzle operating at 345 kPa is used as the base case about which the parameters are varied.

The kinetic energy source term is a correction for the sheet model. It covers two inadequacies. Firstly, it corrects for any errors associated with the sheet amplitude measurement, or the modelling of the sheet behaviour. Secondly, it accounts for any of the features of breakup which act to increase the distribution of drop velocity. The values used here represent increases of between 5.7 and 12 percent of the total kinetic energy in the sheet. A positive source term value will produce a higher variance of velocity than would be seen without the source term. The consistent requirement for a positive source term indicates that further distributive processes are taking place, beyond the "surface area decay" processes incorporated in the model. This is consistent with the discrepancies between measured and predicted values of the D_{32}, which indicate a further disruptive process which reduces the average drop size beyond that predicted by the simple model of section 5.1.1.

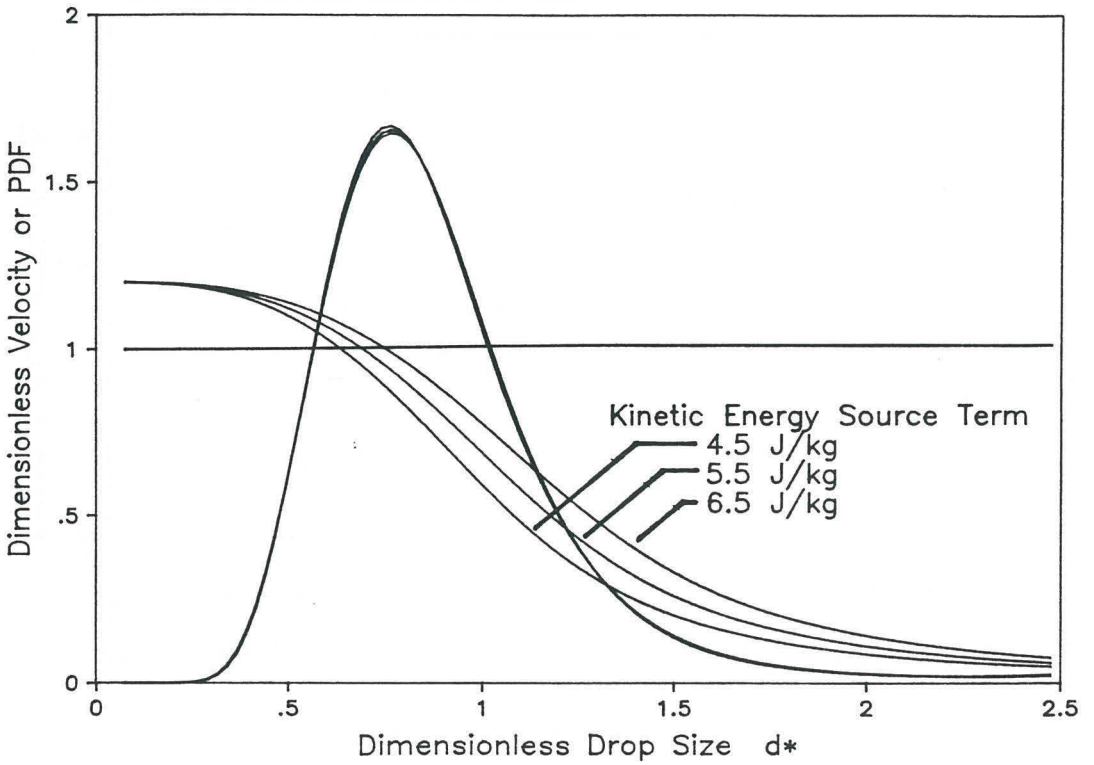

Figure 5.18: Effects of varying the kinetic energy source term. Only the variance of velocity shows significant change. The drop size distribution and mean velocity are unaffected.

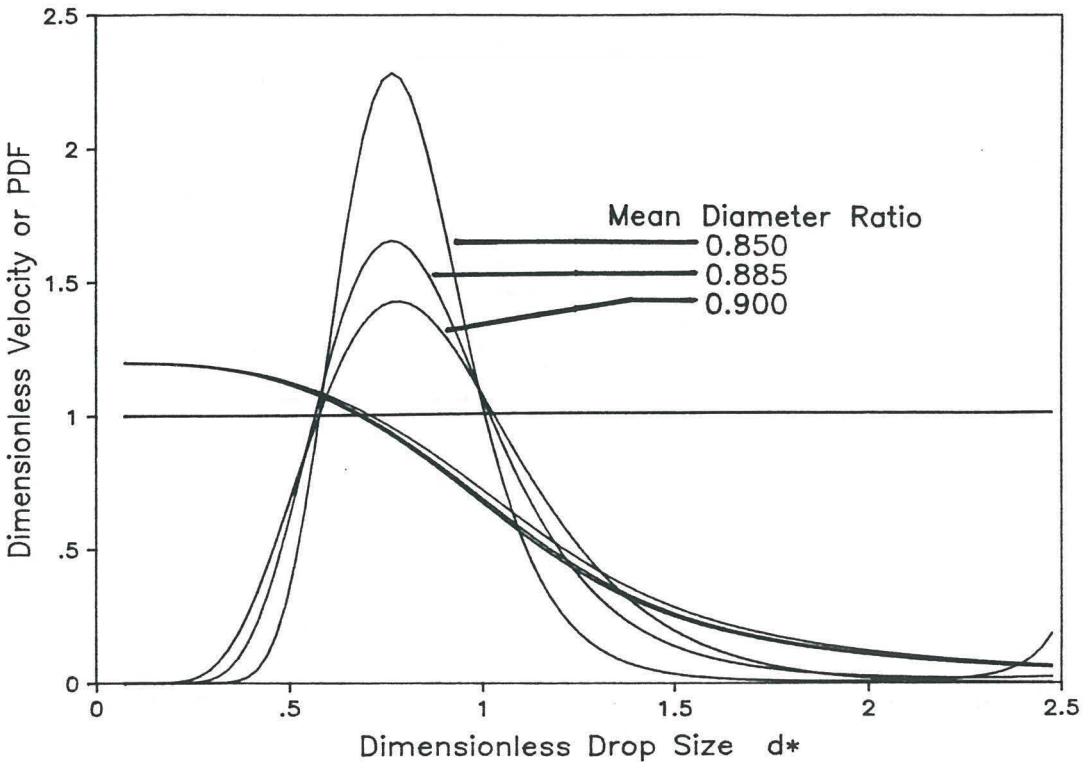

Figure 5.19: Effects of varying the D_{30}/D_{32} ratio. Only the drop size distribution is affected by this parameter.

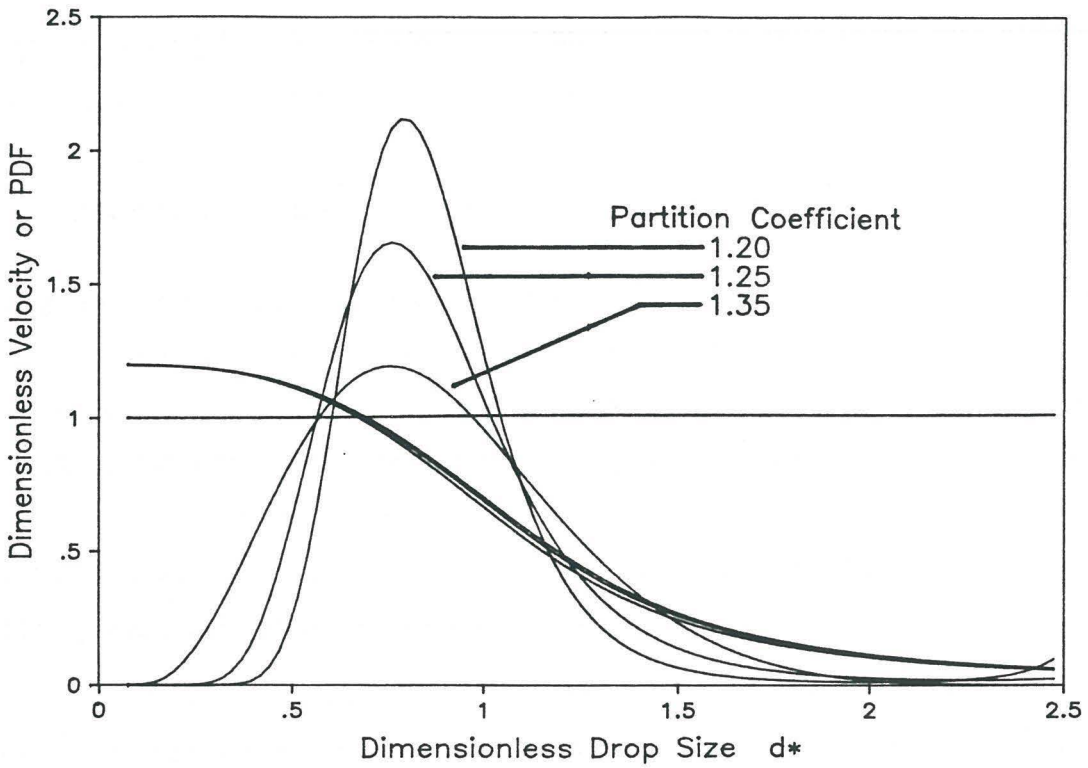

Figure 5.20: Effects of varying the partition coefficient K_p. Only the drop size distribution is affected by this parameter.

There is nothing in the global conservation argument that permits an estimate of the D_{30}/D_{32} ratio, or the partition coefficient. Together they are responsible for the broadness of the drop size distribution. In both cases, values closer to unity result in narrower distributions. Neither of these parameters show large variations in the sprays under study. With a larger experimental study it might be possible to correlate these values with atomizer parameters, perhaps a Weber number plus some description of atomizer geometry.

5.4.2 Potential for Application to Other Modes of Atomization

Although the present work is directed towards a specific mode of atomization, the technique is suited for wider application. The case of liquid sheet breakup was chosen for this work due to the ease with which conservation constraints may be formulated. This is primarily due to the fact that the production of surface energy by sheet stretching is separated from the breakup process, allowing a reasonable estimate of the surface energy present in the spray to be made. In more complex modes of atomization the various processes are not so readily separable and constraints would be correspondingly more difficult to obtain.

One example of a more complex system is the breakup of a cylindrical, turbulent jet. (Diesel injectors provide a transient, cylindrical, turbulent jet, the behaviour of which is not well understood.) One mechanism postulated for the breakup of such jets is the interaction of the jet turbulence with the surface of the jet. The energy of the turbulence would act to break out elements of the jet as individual particles. In this instance, it might be possible to formulate similar constraints based on the transfer of the kinetic energy of the turbulence to the surface energy and kinetic energy of the drops. The following paragraphs outline the approach that might be taken to formulate the constraints.

At the nozzle exit there is a jet of known dimensions, velocity and turbulent kinetic

energy. This allows the formulation of constraints on the mass, linear momentum and kinetic energy. The momentum and kinetic energy constraints would include source terms to accommodate physical knowledge of the breakup process. To formulate a model analogous to the present one, an additional constraint is required for the surface energy.

If the breakup mechanism is as described above, then some fraction of the kinetic energy of turbulence is transformed into surface energy, some into directed kinetic energy of individual drops, while the remainder is dissipated at some point in the process. Before constraints can be formulated, this partition of turbulent kinetic energy must be known, or modelled. For the present, though, it will be assumed known. Taking the initial surface energy of the jet and adding the surface energy produced by the turbulence provides a constraint on the surface energy of the spray. The kinetic energy imparted to individual droplets during breakup adds to both the kinetic energy and momentum of the resulting spray. While the momentum contributions could be expected to cancel out due to directional uniformity, there would be a small, but potentially important contribution to the kinetic energy.

The constraints formed in this way would be mathematically equivalent to the constraints for the undulating sheet. The differences would lie in the numerical values associated with the constraints, and thus the resulting distributions could have a different character.

Chapter 6

Conclusions

This thesis presents a physical model of the breakup of a two dimensional undulating liquid sheet in a quiescent environment, based on a combination of integral conservation constraints and the maximum entropy formalism. This model yields a physically reasonable prediction of the joint drop size and velocity distribution in a spray. The drop size distribution shows the same qualitative characteristics that are present in the widely used empirical distributions. The velocity distribution is Gaussian in cross-section, with both the transverse and streamwise components of velocity showing the same variance. The mean velocities do not vary substantially with drop size, however the variance of velocity decreases with increasing drop size.

The physical model is in close agreement with experimental data obtained using the Phase / Doppler measurement technique in a simple spray. The agreement includes

- Similarity of drop size distribution.

- Similarity of mean velocity at different drop sizes, except where drag has had a substantial effect.
- Similarity of the variance of velocity at different drop sizes, except where drag has had a substantial effect.
- Measured drop velocity distributions that are not inconsistent with the predicted Gaussian profile. However, the small sample sizes and coarse grid do not provide conclusive evidence.

The physical model detailed here is unique in the study of sprays. The entire approach differs from previous work, which has been based on deterministic rather than statistical approaches. The success of this model provides substantial insight into the nature of atomization mechanisms, creating a foundation for future work on the nature of a variety of sprays.

This work suggests that global conservation is sufficient to explain the nature of the atomization process. It is unnecessary to describe the processes that lead to the formation of each drop. Only the overall quantities and their distribution are important. As should be expected, global information is sufficient to predict global characteristics.

Nomenclature

A	surface area, or undulation amplitude measured from photographs
$A(\,)$	amplitude function in the sheet model
A, B, C	points on the undulating sheet
A', B', C'	the points corresponding to A, B, C a short time later
BL	breakup length measured from photographs
D	laser beam diameter
D_{30}	mass or volume mean diameter
D_{32}	Sauter mean diameter
d_{lig}	ligament diameter
d	laser beam waist diameter
f	a probability density function, or a focal length
f_δ	drop number probability density function over size space only

g	some function of location in the solution space
$< g >$	the average or expectation value of g
K_p	a coefficient of partition of surface energy
k	Boltzmann constant
l	length
M	total mass of liquid in the sheet
m	cumulative mass fraction or the mass of a drop
$\dot{m}$	mass flow rate
N	total number of drops in the system
n	cumulative number fraction
n_c	refractive index of the continuous phase
n_d	refractive index of the dispersed phase
n'	ratio of refractive indices, $n' \equiv n_d/n_c$
p	probability of a particular discrete event
Q	volume flow rate
R	dimensional source term – per unit mass basis(subscripted)
S	Shannon entropy, or a dimensionless source term (subscripted)
s	distance along the sheet for line integrals in the sheet model

t	time
U	bulk velocity in the downstream direction
$U_\perp$	perpendicular component of velocity (relative to LDA measurement axis)
u	local or drop velocity in the downstream direction
V	bulk velocity in the cross-stream direction
v	local or drop velocity in the cross-stream direction
WL	one half of the undulation wavelength, measured from the spray photographs.
X	rotameter reading
x	downstream spatial dimension, or beam separation
y	cross-stream spatial dimension
Δ	geometric factor in Phase / Doppler relations
δ	drop diameter
θ	laser crossing angle, or spray cone angle
λ	arbitrary Lagrange multiplier (subscripted), undulation wavelength, or wavelength of laser light
ν_D	Doppler difference frequency
ρ	density

σ	surface tension
τ	sheet thickness
Φ	Phase / Doppler signal phase shift – angle
ϕ	Phase / Doppler elevation angle
ψ	solution space (usually $d\psi = d\delta_{\cdot} du_{\cdot} dv_{\cdot}$), or Phase / Doppler collection angle

Subscripts

a	air
f	pertaining to a flat sheet, rather than an undulating one
ke	kinetic energy
l	liquid
m	mass for a PDF or source term, or measurement volume
mu	x momentum
mv	y momentum
net	remaining after application of sources and sinks
r	receiving optics
s	sheet, surface energy for a source term, or sending optics

$*$	normalized by D_{30} for a length or U_s for a velocity
1,2	measurements from the two different sides of the cone seen in the spray photographs
$0, 1, 2, ..., j, ...$	association with a particular discrete state
$0, 1, 2, ..., i, ..., n$	association with a particular constraint number

Superscripts

$'$	prime indicates a corresponding position, some small time later

References

[1] Sellens, R.W. and Brzustowski, T.A. A Prediction of the Drop Size Distribution in a Spray from First Principles, *Atomisation and Spray Technology*, **1**, 89-102, 1985.

[2] Sellens, R.W. and Brzustowski, T.A. A Simplified Prediction of Droplet Velocity Distributions in a Spray, *Combustion and Flame*, **65**, 273-279, 1986.

[3] Sellens, R.W. *A Prediction of the Droplet Size and Velocity Distribution in a Spray From First Principles*, M.A.Sc. Thesis, University of Waterloo, Waterloo, Ontario, Canada, 1985.

[4] Dombrowski, N. and Johns, W.R. The Aerodynamic Instability and Disintegration of Liquid Sheets, *Chem. Eng. Sci.*, **18**, 203-214, 1963.

[5] Rayleigh, Lord On the Instability of Jets, *Proc. London Math. Soc.*, **10**, 4-13, 1878.

[6] Weber, C. *Z. Angew. Math. Mech.*, **11**, 138-145, 1931.

[7] Levich, V.G. *Physicochemical Hydrodynamics*, Prentice-Hall Inc., Englewood Cliffs, New Jersey, 1962.

[8] Mayer, E. Theory of Liquid Atomization in High Velocity Gas Streams, *ARS J.*, **31**, 1783, 1961.

[9] Hinze, J.O. *Appl. Sci. Res.*, **A. 1**, 273, 1948.

[10] Rice, E.J. Section 2.2.3 Mechanisms of Atomization, *Liquid Propellant Rocket Combustion Instability*, NASA SP-194, NASA, Cleveland, Ohio, 49-55, 1972.

[11] Jaynes, E.T. Information Theory and Statistical Mechanics, I, II, *Physical Review*, 106, 620-630, 108, 171-190, 1957. Reprinted in *E.T. Jaynes: Papers on Probability, Statistics and Statistical Physics* (R.D. Rosenkrantz, Ed.), D. Reidel Publishing Company, Dordrecht, Holland, 1983.

[12] Jaynes, E.T. Where Do We Stand On Maximum Entropy?, *The Maximum Entropy Formalism* (R.D. Levine and Myron Tribus, Eds.), The MIT Press, Cambridge, Massachusetts, 15-118, 1979.

[13] Tribus, Myron *Thermostatics and Thermodynamics*, D. Van Nostrand Company, Inc., Princeton, New Jersey, 1961.

[14] Tribus, Myron *Rational Descriptions Decisions and Designs*, Pergamon Press, New York, 1969.

[15] Delavan Inc. *Oil Burner Nozzles and Accessories for residential and industrial applications* (catalog), Fuel Metering Products Operation, P.O. Box 969, Bamberg, SC, USA, 1984.

[16] Malvern Instruments Limited, Spring Lane Trading Estate, Malvern, Worcestershire, England WR14–1AQ

[17] Swithenbank, J., Beer, J.M., Taylor, D.S., Abbot, D. and McCreath, G.C. A Laser Diagnostic Technique for the Measurement of Droplet and Particle Size Distribution, *Progress in Astronautics and Aeronautics*, B.T. Zinn, Ed., A.I.A.A., **53**, 421-447, 1977.

[18] Negus, C. and Azzopardi, B.J. *The Malvern Particle Size Distribution Analyzer: Its Accuracy and Limitations*, U.K. Atomic Energy Authority, Harwell, Report AERE-R9075, 1978.

[19] Meyer, P. and Chigier, N. Dropsize Measurements Using a Malvern 2200 Particle Sizer, *Atomisation and Spray Technology*, **2**, 261-298, 1986.

[20] Breña de la Rosa, A. *The Influence of Drop Size Distribution on the Structure of Unconfined Spray Flames*, Ph.D. Thesis, University of Waterloo, Waterloo, Ontario, Canada, 1986.

[21] Timmerman, M. Laser Particle Size Velocimeter, *First International Symposium on Applications of Laser Anemometry to Fluid Mechanics*, Lisbon, Portugal, 1982.

[22] Durst, F. Review – Combined Measurements of Particle Velocities, Size Distributions, and Concentrations, *Trans. ASME, J. Fluids Eng.*, **104**, 284-296, 1982.

[23] Chigier, N. Drop Size and Velocity Instrumentation, *Prog. Energy Combust. Sci.*, **9**, 155-177, 1983.

[24] Durst, F. and Zare, M. *Proc. LDA Symposium*, p. 403, Copenhagen, Denmark, 1975.

[25] Bachalo, W.D. and Houser, M.J. Phase/Doppler spray analyzer for simultaneous measurements of drop size and velocity distributions, *Optical Engineering*, **23**, 583-590, 1984.

[26] Bachalo, W.D. and Houser, M.J. Spray Drop Size and Velocity Measurements Using the Phase/Doppler Particle Analyzer, *International Conference on Liquid Atomisation and Spray Systems (ICLASS-85)*, The Institute of Energy, London, England, paper VC/2, 1985.

[27] Bauckhage, K. and Flögel, H.H. Simultaneous Measurement of Droplet Size and Velocity in Nozzle Sprays, *Second International Symposium on Applications of Laser Anemometry to Fluid Mechanics*, Lisbon, Portugal, 1984.

[28] Bauckhage, K., Flögel, H.H., Fritsching, U., Hiller, R. and Schöne, F. Analysis of Particle Sizes With the Aid of Laser–Doppler–Anemometry: The Influence of Specific Geometrical and Optical Properties of Particles, *Third International Symposium on Applications of Laser Anemometry to Fluid Mechanics*, Lisbon, Portugal, 1986.

[29] Saffman, M., Buchave, P. and Tanger, H. Simultaneous Measurement of Size, Concentration and Velocity of Spherical Particles by a Laser Doppler Method, *Second International Symposium on Applications of Laser Anemometry to Fluid Mechanics*, Lisbon, Portugal, 1984.

[30] Aerometrics, Inc. P.O. Box 308, Mountain View, California, USA, 94042.

[31] Dantec Elektronik Mileparken 22, DK-2740 Skovlunde, Denmark.

[32] Durst, F., Melling, A. and Whitelaw, J.H. *Principles and Practice of Laser-Doppler Anemometry*, Academic Press, London, 1976.

[33] Sellens, R.W. *Code Listings and Raw Data Associated with the Thesis: Drop Size and Velocity Distributions in Sprays, A New Approach Based on the Maximum Entropy Formalism*, Mechanical Engineering Report, University of Waterloo, Waterloo, Ontario, Canada, 1987.

[34] Shannon, Claude *Bell System Tech. J.*, **27**, 1948. Reprinted in Shannon, C.E. and Weaver, W., *The Mathematical Theory of Communication*, University of Illinois Press, Urbana, 1949.

[35] Agmon, N., Alhassid, Y. and Levine, R.D. An Algorithm for Determining the Lagrange Parameters in the Maximal Entropy Formalism, *The Maximum Entropy Formalism*, (Ed. R.D. Levine and Myron Tribus), pp. 207-209, The MIT Press, Cambridge, Massachusetts, 1979.

[36] Barford, N.C. *Experimental Measurements: Precision, Error and Truth, Second Edition*, John Wiley & Sons, New York, 1985.

Appendix A

The Maximum Entropy Formalism and Its Solution

This section first appeared as Chapter 1 in Sellens' Master's thesis [2]. It is included here for completeness. It has been reformatted, references adjusted to match the References section in this work, and an irrelevant section on doubly truncated Gaussian distributions has been omitted, but it is otherwise unchanged.

A.1 The Shannon Entropy

In 1948 Claude Shannon [34] proposed a definition of entropy as it relates to communication theory as:

$$S = -k \sum_j p_j \ln p_j \tag{A.1}$$

This entropy is a measure of the information present in a message. Consider a communication line whose state (perhaps voltage) is varying with time so as to transmit information.

If the state remains constant then the minimum amount of information is transmitted and the entropy from equation A.1 is a maximum. Any deviation from a uniform state provides some information, either message or noise, and correspondingly reduces the entropy. The more unlikely the event (smaller probability), the greater the amount of information carried by such an event.

If the entire signal is of interest, then both the noise and message components of the signal provide information. The former provides information about the noise sources in the system, while the latter provides information about the message sent. However, the noise content is usually not of interest and acts only to mask the message. The base, or maximum entropy, state must then be taken as a constant null message state with a statistical representation of the noise superimposed. In this case any message signals must be larger, or contain greater redundancy, in order to be discernible from the noise. Only the discernible portions of the message will provide any additional information, and thus a reduction in entropy.

Shannon applied this idea to the design of communications hardware, calculating such things as the channel capacity of a communications link in the presence of different noise conditions. The effect of his work has, however, been felt over a far wider range of subjects.

A.2 Edwin Jaynes and Myron Tribus

The work of Edwin Jaynes [11] starting in 1957 builds on Shannon's information theory and shows that the methods of statistical mechanics are in fact a special case of statistical inference based on the entropy measure of information. Jaynes proposed a formalism for the maximization of entropy subject to constraints which can be applied in any type of problem with incomplete information. Myron Tribus has done substantial work in applying

this formalism and making it available to the engineering profession as it relates to thermodynamics [13] as well as problems in design and resource management [14] The following section presents the maximum entropy formalism in much the same form as it is presented by Tribus in references [13] and [14].

A.3 The Maximum Entropy Formalism

The maximum entropy formalism is useful when the information available describing the system under consideration is macroscopic in nature, describing some average or moment of the system. Examples of this type of information include:

- the temperature of a system of molecules as a statement of the average kinetic energy of molecules in that system.
- the mean and variance of a part's diameter over a production run as information on a set of quality control measurements.
- any other measure which is the average of some property over all the elements in the system.

Any information of this type can be written as a constraint on the probability distribution of the form

$$\sum_j p_j g_j = < g > \tag{A.2}$$

where p_j is the probability of some state j, g_j is some function of state evaluated at state j and $< g >$ is the (known) expectation or average value of the function g over the entire system. The summation is over some range of j so that all possible states of the system are evaluated.

If a set of such constraints is combined with a normalization constraint requiring the sum of the probabilities to be unity, this system of equations results:

$$\sum_j p_j = 1 \tag{A.3}$$

$$\sum_j p_j g_{ij} = < g_i > \qquad i = 1, 2, 3, \ldots, n \tag{A.4}$$

In cases of interest there are generally many more possible states than there are constraints available, making this system of equations indeterminate. A method is needed to choose the most appropriate solution which satisfies the constraints. The Shannon Entropy provides the criterion.

If a solution is found to fit the constraints, then all the information that is present in the constraints must be present in the resulting solution, for each of the constraints may be obtained by taking the appropriate moment of the distribution. By maximizing the entropy, subject to the constraints, one obtains the distribution of probabilities containing the least amount of information, while still containing all the information present in the constraints. This solution will be the most appropriate because it conveys all the available information without adding any unjustified bias in the form of additional information.

The solution of the system of equations which produces the maximum entropy can be found using the method of Lagrange multipliers. Differentiation of equation A.1 with respect to the p_j yields

$$dS = -k \sum_j (\ln p_j + 1) dp_j \tag{A.5}$$

and setting $dS = 0$ for a maximum gives

$$\sum_j (\ln p_j + 1) dp_j = 0 \tag{A.6}$$

Similar differentiation of equations A.3 and A.4, noting that the $< g_i >$ are constant, yields

$$\sum_j dp_j = 0 \tag{A.7}$$

$$\sum_j g_{ij} dp_j = 0 \qquad i = 1, 2, 3, \ldots, n \tag{A.8}$$

To obtain the solution the above $n + 1$ equations are multiplied by some set of arbitrary multipliers. For simplicity in solution the first equation is multiplied by $(\lambda_0 - 1)$ and the rest by the set λ_i; $i = 1, 2, 3, \ldots, n$. If these multiplied equations are then summed in combination with the previous equation the result is

$$\sum_j (\ln p_j + 1) dp_j + \sum_j (\lambda_0 - 1) dp_j + \sum_{i=1}^{n} \sum_j \lambda_i g_{ij} dp_j = 0 \tag{A.9}$$

or, combining terms,

$$\sum_j \left[\ln p_j + \lambda_0 + \sum_{i=1}^{n} \lambda_i g_{ij} \right] dp_j = 0 \tag{A.10}$$

To ensure that this equation is satisfied for arbitrary dp_j, the quantity within the square brackets is set to zero.

$$\ln p_j + \lambda_0 + \sum_{i=1}^{n} \lambda_i g_{ij} = 0 \tag{A.11}$$

so that, after dropping the state index j

$$p = \exp(-\lambda_0 - \lambda_1 g_1 - \lambda_2 g_2 - \ldots - \lambda_n g_n) \tag{A.12}$$

where values of the probability p and the functions g_i vary with the state point being evaluated and the λ_i are constant. Equation A.12 is the solution to the problem. It is the probability distribution which maximizes the entropy under the given constraints. However, the Lagrange multipliers are still undetermined. They must be chosen in such a way as to satisfy the constraint equations.

Substituting equation A.12 into the normalization constraint equation A.3 gives

$$\sum p = \sum \exp(-\lambda_0 - \lambda_1 g_1 - \lambda_2 g_2 - \ldots - \lambda_n g_n) = 1 \qquad \text{(A.13)}$$

or with rearrangement

$$\lambda_0 = \ln\left(\sum \exp(-\lambda_1 g_1 - \lambda_2 g_2 - \ldots - \lambda_n g_n)\right) \qquad \text{(A.14)}$$

which permits the direct evaluation of λ_0, given the values of the other multipliers. This is simply a restatement of the normalization constraint and λ_0 is a normalization parameter which alters only the magnitude of the probabilities, not their relative distribution.

Since equation A.12 can be used to replace p_j in all the constraint equations the system is now a set of $n+1$ equations in $n+1$ unknowns. The equations are the n physical constraints derived from the problem and set in the form of equation A.4, plus the normalization constraint expressed as either equation A.3 or equation A.14. The $n+1$ variables are the Lagrange multipliers λ_0, λ_1, λ_2, ..., λ_n.

These summation equations are not easily solved, except in trivial cases. The problem can be simplified by translating these discrete summation equations and their solution to some equivalent continuous form where the familiar methods of calculus can be applied.

A.3.1 "Extension" of the Maximum Entropy Formalism to a Multi-Dimensional Solution Space

It is easy to see how the previously derived formalism can be applied to a one dimensional problem. One simply maps the state index j directly onto the one dimensional variable in question. Many problems in thermodynamics involve quantum states and are easily viewed as an ensemble of possible discrete states. Even if the problem concerns a variable that is continuous in one dimension, it can be readily discretized to match the formalism.

It is important to note that in the derivation of the formalism there is no assumption of the "shape" of the solution space. It is said only that the summations are over the set of possible state points and that each g_i is some function of which state point j is being considered. The j is an index only, and need not have any correlation with the physical parameters of the solution space. The index j can map into a one, two, or even n dimensional solution space with equal validity. The index need not map into the solution space completely, or even in a contiguous manner. There may be states which are in general possible, but which are excluded from a specific solution because of the nature of the problem. These excluded states may be those beyond some maximum or minimum bound, or they may be "forbidden" states which lie within the general domain.

This can be verified by deriving the formalism with a different number of index parameters. If the number of index parameters was significant one would not obtain the same results using two parameters as one. However, the only difference in results is that which was introduced explicitly: the requirement for two index subscripts instead of one.

A.4 An Equivalent Continuous Formalism

Many physical problems do not naturally lend themselves to solution in a space consisting of a finite number of discrete states. On a macroscopic level the physical variables are usually continuous rather than discrete. This can be handled in two ways; either the continuous physical space can be discretized to give a solution space which matches the formalism, or an equivalent formalism can be developed for the continuous solution space. The latter is preferable both because it provides a more natural representation of the physical problem and because it leads to the more familiar continuous mathematics and integrals rather than discrete mathematics and summations.

Consider a solution space having m dimensions represented by the independent variables $x_1, x_2, x_3, \ldots, x_m$. The solution space is discretized into elements which are uniform with respect to some set of monotonically increasing or decreasing functions $h_1(x_1)$, $h_2(x_2)$, $h_3(x_3), \ldots, h_m(x_m)$ so that for any mesh element

$$h_i(x_i + \Delta x_i) - h_i(x_i) \;=\; \text{a constant} \tag{A.15}$$

If Δx_i is small, one can make the approximation

$$\frac{\partial h_i}{\partial x_i} \approx \frac{h_i(x_i + \Delta x_i) - h_i(x_i)}{\Delta x_i} \tag{A.16}$$

which, in combination with equation A.15, gives the relation

$$\Delta x_i \propto \left(\frac{\partial h_i}{\partial x_i}\right)^{-1} \tag{A.17}$$

Now define $\Delta\psi$ as a small element of the solution space ψ so that

$$\Delta\psi \equiv \Delta x_1 \Delta x_2 \Delta x_3 \ldots \Delta x_m \tag{A.18}$$

and define some base set of discretization volumes $\{\Delta\psi_b\}$ to work from so that

$$\{\Delta\psi_b\} \;=\; \frac{C_b}{\left\{\frac{\partial h_1}{\partial x_1}\right\}\left\{\frac{\partial h_2}{\partial x_2}\right\}\left\{\frac{\partial h_3}{\partial x_3}\right\}\cdots\left\{\frac{\partial h_m}{\partial x_m}\right\}} \tag{A.19}$$

where C_b is a proportionality constant. A proportionality constant K is used to define a corresponding set of smaller volumes with the same discretization shape as $\{\Delta\psi_b\}$.

$$\{\Delta\psi\} \equiv \frac{\{\Delta\psi_b\}}{K} \tag{A.20}$$

From application of the maximum entropy formalism over $\{\Delta\psi_b\}$

$$p_b \;=\; \exp(-\lambda_{0b} - \lambda_{1b} g_1 - \lambda_{2b} g_2 - \ldots - \lambda_{nb} g_n) \tag{A.21}$$

is the probability associated with a particular $\Delta\psi_b$ where $g_1, g_2, \ldots, g_n$ are functions of location in ψ. If the probability density is continuous and $\{\Delta\psi_b\}$ is fine enough to resolve it, then

$$\{p\} \approx \frac{\{p_b\}}{K} \tag{A.22}$$

is a good approximation for the set of probabilities associated with the smaller volumes $\{\Delta\psi\}$. Substituting in equation A.21 yields the following expression for the probability.

$$p = \exp(-(\lambda_{0b} + \ln K) - \lambda_{1b}g_1 - \lambda_{2b}g_2 - \ldots - \lambda_{nb}g_n) \tag{A.23}$$

Define a set of probability densities and rewrite the above equation for f, a probability density function or PDF, rather than p, a probability.

$$\{f\} \equiv \frac{\{p\}}{\{\Delta\psi\}} \tag{A.24}$$

$$f = \exp(-(\lambda_{0b} + \ln K + \ln \Delta\psi) - \lambda_{1b}g_1 - \lambda_{2b}g_2 - \ldots - \lambda_{nb}g_n) \tag{A.25}$$

Recalling that $K = \Delta\psi_b/\Delta\psi$, or $\ln K = \ln \Delta\psi_b - \ln \Delta\psi$, the above expression can be reduced to

$$f = \frac{1}{\Delta\psi_b} \exp(-\lambda_{0b} - \lambda_{1b}g_1 - \lambda_{2b}g_2 - \ldots - \lambda_{nb}g_n) \tag{A.26}$$

Substituting in from equation A.19 and redefining the Lagrange multipliers as

$$\lambda_0 = \lambda_{0b} + \ln C_b \qquad \lambda_1 = \lambda_{1b} \qquad \lambda_2 = \lambda_{2b} \quad \ldots \quad \lambda_n = \lambda_{nb}, \tag{A.27}$$

gives the final expression for the equivalent continuous probability density function.

$$f = \frac{\partial h_1}{\partial x_1}\frac{\partial h_2}{\partial x_2}\frac{\partial h_3}{\partial x_3}\ldots\frac{\partial h_m}{\partial x_m} \exp(-\lambda_0 - \lambda_1 g_1 - \lambda_2 g_2 - \ldots - \lambda_n g_n) \tag{A.28}$$

If the original solution space was discretized uniformly over each of the independent variables then each of the $\partial h_i/\partial x_i$ will be constant over the solution space. If these constants

are absorbed into λ_0 in the same way that C_b was, the result is an expression for the PDF over a continuous field, equivalent to a discrete formulation with uniform discretization over each of the independent variables.

$$f = \exp(-\lambda_0 - \lambda_1 g_1 - \lambda_2 g_2 - \ldots - \lambda_n g_n) \tag{A.29}$$

Examination shows that equation A.29 gives the PDF f in the same form that equation A.12 gives the discrete probability p_j. The only difference is in the value of λ_0, and this difference reflects a constant of proportionality between p_j and f which will depend on the magnitude of the grid used in the discrete solution.

A.4.1 The Meaning of a Non-Uniform Discretization

In the previous section a continuous formalism was developed based on some potentially non-uniform discretization of the solution space. What does it mean to use a non-uniform discretization with the maximum entropy formalism?

Discretization is the first task required in applying the formalism. It must be done on some rational basis. What is the most reasonable way to divide a continuous field? In the absence of information to the contrary, any field should be divided into uniform elements based on the unit of measure being applied. To do anything else would imply further information that allows one part of the field to be differentiated from another on some basis other than the applied unit of measure. If one has such information it would be preferable to apply it as a constraint, through the usual means of the formalism.

In some cases, however, the field might best be described physically by some other unit of measure, but for practical reasons it is desirable to represent it in the chosen units. (i.e. it may be appropriate to consider specific kinetic energy as the best physical description,

rather than velocity, but velocity is the desired scale for reasons of presentation.) In this one may apply a discretization which is non-uniform in the scale units to provide a discretization which is uniform in the units which are felt to be most physically representative.

In any event, the use of a non-uniform discretization implies prior information of some sort which is not necessarily present in the constraints. In the absence of all physical constraints each state is equally probable and a non-uniformity of discretization puts more divisions, or states, in one area of the field than another. This results in a non-uniform probability density which has some information content beyond the minimum for the definition of the field.

A.5 Solution of the Equations in the Continuous Form

The transformation to a continuous solution space yields a system of integral equations which take the form

$$\int_{\psi} f g_0 d\psi = < g_0 > \tag{A.30}$$

$$\int_{\psi} f g_1 d\psi = < g_1 > \tag{A.31}$$

$$\int_{\psi} f g_2 d\psi = < g_2 > \tag{A.32}$$

$$\int_{\psi} f g_n d\psi = < g_n > \tag{A.33}$$

$$f = \exp(-\lambda_0 - \lambda_1 g_1 - \lambda_2 g_2 - \ldots - \lambda_n g_n) \tag{A.34}$$

$$\lambda_0 = \ln \left[\int_{\psi} \exp(-\lambda_1 g_1 - \lambda_2 g_2 - \ldots - \lambda_n g_n) d\psi \right] \tag{A.35}$$

where g_0 and $< g_0 >$ are defined as equal to one to put the normalization constraint equation in the same form as the other constraint equations.

Agmon, Alhassid and Levine [35] give a method for solution of a discrete maximum entropy formalism problem. They dismiss the use of an iterative method of the Newton - Rhapson type as generally non-convergent, even in a system with only a single constraint. In this section a slightly modified solution method of the Newton - Rhapson type is developed for the continuous problem. The new method converges well, even in a system of four constraints.

The constraints can be rewritten as functionals $q_0, q_1, q_2, \ldots, q_n$ with values of zero.

$$q_0 = \int_\psi f g_0 d\psi - < g_0 > = 0 \tag{A.36}$$

$$q_1 = \int_\psi f g_1 d\psi - < g_1 > = 0 \tag{A.37}$$

$$q_2 = \int_\psi f g_2 d\psi - < g_2 > = 0 \tag{A.38}$$

$$\ldots$$

$$q_n = \int_\psi f g_n d\psi - < g_n > = 0 \tag{A.39}$$

Consider q_i as a general constraint functional and a quantity $q_i' = q_i(\lambda_0', \lambda_1', \lambda_2', \ldots, \lambda_n')$ where the prime indicates values which are used as a guess in the current iteration. Taking a first order Taylor series expansion about q_i' gives

$$q_i = q_i' + (\lambda_0 - \lambda_0')\frac{\partial q_i}{\partial \lambda_0} + (\lambda_1 - \lambda_1')\frac{\partial q_i}{\partial \lambda_1} + (\lambda_2 - \lambda_2')\frac{\partial q_i}{\partial \lambda_2} + \ldots + (\lambda_n - \lambda_n')\frac{\partial q_i}{\partial \lambda_n} \tag{A.40}$$

and setting q_i equal to zero to satisfy the i^{th} constraint yields:

$$\frac{\partial q_i}{\partial \lambda_0}\lambda_0 + \frac{\partial q_i}{\partial \lambda_1}\lambda_1 + \frac{\partial q_i}{\partial \lambda_2}\lambda_2 + \ldots + \frac{\partial q_i}{\partial \lambda_n}\lambda_n = - q_i' + \frac{\partial q_i}{\partial \lambda_0}\lambda_0' + \frac{\partial q_i}{\partial \lambda_1}\lambda_1' + \frac{\partial q_i}{\partial \lambda_2}\lambda_2' + \ldots + \frac{\partial q_i}{\partial \lambda_n}\lambda_n' \tag{A.41}$$

Applying this approach to each of the constraints in turn gives a system of $n+1$ linear equations in $n+1$ unknowns. This system is shown in Figure A.5.

As the solution space, the g_i values, and the expectation values are independent of the Lagrange multipliers it is a simple matter to evaluate the derivatives.

$$q_i = \int_{\psi} f g_i d\psi - < g_i > \tag{A.42}$$

$$\frac{\partial q_i}{\partial \lambda_j} = \int_{\psi} \frac{\partial f}{\partial \lambda_j} g_i d\psi = - \int_{\psi} f g_j g_i d\psi \tag{A.43}$$

The derivatives $\partial q_i / \partial \lambda_j$ can be evaluated at q_i'. It would be convenient if this system of equations converged nicely over a few iterations to a solution. However, as observed by Agmon et al, this system is unstable and generally does not converge without intervention.

In fact, this system can be stabilized by using equation A.35 after each iteration to ensure that normalization is maintained. On reflection it is clear that the definition of the PDF is fundamental, and that if normalization is not maintained the system will fall apart. The Newton - Rhapson approach by itself does not ensure normalization at all stages of solution.

$$\left[\begin{array}{ccccc|c} \frac{\partial q_0}{\partial \lambda_0} & \frac{\partial q_0}{\partial \lambda_1} & \frac{\partial q_0}{\partial \lambda_2} & \cdots & \frac{\partial q_0}{\partial \lambda_n} & \lambda_0 \\ \frac{\partial q_1}{\partial \lambda_0} & \frac{\partial q_1}{\partial \lambda_1} & \frac{\partial q_1}{\partial \lambda_2} & \cdots & \frac{\partial q_1}{\partial \lambda_n} & \lambda_1 \\ \frac{\partial q_2}{\partial \lambda_0} & \frac{\partial q_2}{\partial \lambda_1} & \frac{\partial q_2}{\partial \lambda_2} & \cdots & \frac{\partial q_2}{\partial \lambda_n} & \lambda_2 \\ \vdots & \vdots & \vdots & \ddots & \vdots & \vdots \\ \frac{\partial q_n}{\partial \lambda_0} & \frac{\partial q_n}{\partial \lambda_1} & \frac{\partial q_n}{\partial \lambda_2} & \cdots & \frac{\partial q_n}{\partial \lambda_n} & \lambda_n \end{array}\right]$$

$$= \left[\begin{array}{l} -q_0' + \frac{\partial q_0}{\partial \lambda_0}\lambda_0' + \frac{\partial q_0}{\partial \lambda_1}\lambda_1' + \frac{\partial q_0}{\partial \lambda_2}\lambda_2' + \ldots + \frac{\partial q_0}{\partial \lambda_n}\lambda_n' \\ -q_1' + \frac{\partial q_1}{\partial \lambda_0}\lambda_0' + \frac{\partial q_1}{\partial \lambda_1}\lambda_1' + \frac{\partial q_1}{\partial \lambda_2}\lambda_2' + \ldots + \frac{\partial q_1}{\partial \lambda_n}\lambda_n' \\ -q_2' + \frac{\partial q_2}{\partial \lambda_0}\lambda_0' + \frac{\partial q_2}{\partial \lambda_1}\lambda_1' + \frac{\partial q_2}{\partial \lambda_2}\lambda_2' + \ldots + \frac{\partial q_2}{\partial \lambda_n}\lambda_n' \\ \vdots \\ -q_n' + \frac{\partial q_n}{\partial \lambda_0}\lambda_0' + \frac{\partial q_n}{\partial \lambda_1}\lambda_1' + \frac{\partial q_n}{\partial \lambda_2}\lambda_2' + \ldots + \frac{\partial q_n}{\partial \lambda_n}\lambda'_n \end{array}\right]$$

Figure A.1: Matrix of linear equations used to solve for the Lagrange multipliers.

Appendix B

Numerical Solution Technique

Numerical solutions to the model were obtained on a personal computer. The primary computer was an IBM PC/AT compatible machine with a floating point processor. The program will also run on a basic IBM PC with a floating point processor, but at lower speeds. A complete calculation, at reasonable error levels, required about an hour of computing on the AT. This computing time varied in both directions, depending on the convergence properties of the particular solution and on the solution parameter settings.

B.1 The Algorithms

The computational model exists as two distinctly separate modules that combine to produce results. The first module uses information on the sheet geometry to compute the motions of the sheet just before breakup, and integrates those motions to obtain estimates of the mean sheet momentum and kinetic energy. The second module uses the output of the first to formulate the constraints for the maximum entropy formalism and solves the equations

for the Lagrange multipliers. Both modules produce reports and graphic output.

When integration is required, either Simpson's one third rule, or Simpson's rule with end correction are used. The choice depends on whether the required derivatives are readily available. All of the functions involved are well behaved, with smooth transitions and no singularities. No difficulty was encountered in obtaining accurate results for the integrations.

B.1.1 The Sheet Model

The procedure followed by the sheet model was:

1. Initialize variables, loading sheet data from an input file.
2. Starting at a positive going zero crossing, half a wavelength behind the breakup length, calculate the sheet behaviour over a one wavelength region in four steps, using quarter wavelength segments. (When the entire wavelength was calculated as one section, small numerical errors produced anomalous results near the zero crossings. Breaking the solution into four segments keeps everything on track, eliminating the errors.)
   (a) Set the end points of the segment and calculate the total length by line integration.
   (b) Using the relations of Chapter 3 for each of the elements in the segment, calculate and store each of the following quantities:
      i. Initial x and y location of the element.
      ii. Initial relative position along the segment.
      iii. x and y location of the same relative position along the segment some short time later. This is the new location of that element.

iv. Components of velocity, based on a displacement over time calculation.

v. The sum of the squares of the velocity components.

3. Calculate the mean velocities and the mean of the sum of the squares by integration. These are averages based on the sheet dimension, which will be mass averages if the sheet thickness is a constant.

4. Print Results.

B.1.2 The Maximum Entropy Formalism Solution

The procedure followed by the MEF solver was:

1. Initialize variables, reading parameters from a data file.

2. Set the streamwise momentum and kinetic energy constraints from the values generated by the sheet model, adjusted for input source terms, if any.

3. Set the cross-stream momentum constraint to zero, as any nonzero value predicted by the sheet model will alternate positive and negative, depending on whether a positive or negative going zero crossing is used for the base point in the calculation.

4. Calculate λ_0 to provide normalization in the initial distribution.

5. Repeat the following steps until a convergence test is met.

   (a) Calculate the components for the Newton-Rhapson solution matrix shown in figure A.5. This is done by integration, based on the current estimate of the distribution function

   (b) Solve the matrix of linear equations.

(c) Set the new values of the Lagrange multipliers based on the old values, the matrix solution and a relaxation parameter.

(d) Reduce the magnitude of the relaxation parameter to avoid oscillation of the solution as it nears convergence.

(e) Calculate λ_0 to enforce normalization of the distribution. This step is critical in obtaining a stable, convergent solution.

6. Calculate check values for each of the constraints to test how well the solution satisfies the constraints. These integrations are performed on the solution grid and on a grid with twice the number of divisions to demonstrate grid independence.

7. Print results.

B.2 The Code

The actual computer code is written in the C language, using the DeSmet C Development Package. C was chosen for its portability, speed, and because of the author's prior familiarity with the language. Although not as commonly used in numerical work as Fortran, C provides better control of I/O functions, dynamic memory allocation, etc., while covering the numerical requirements as well as most Fortran compilers. On microcomputers, C is widely used in operating system development. Thus, the development of C compilers for any given architecture usually leads the development of Fortran compilers. Even in the fairly mature IBM PC world, the selection and performance of C compilers is still ahead of comparable Fortran compilers.

The actual code is not provided as part of the thesis, but is available as part of a University of Waterloo Mechanical Engineering Report [33].

Appendix C

Testing of Phase Doppler System and Error Analysis

This appendix describes the setup and testing procedures used with the Phase / Doppler system assembled at LSTM in the fall of 1986. It goes on to develop estimates of error in individual particle measurements, based on the information found in the testing.

C.1 System Setup and Alignment

The system arrangement is described in section 4.4. Once assembled, the optical components must be aligned to provide proper signals, or for that matter, any signals at all. With the laser and rotating grating fixed in horizontal positions, the plane mirrors were adjusted so that

- the laser beam was horizontal, measured with respect to the table.

- the beam struck the centre of the first order band on the rotating diffraction grating.

The separation between the parallel beams leaving the lens of the rotating grating system were measured. The 310 mm sending lens was fixed in place, locating the laser crossing volume within the range of the nozzle traversing system.

The optical rail for the receiving optics was bolted to the table with its axis going through the known location of the crossing volume. The angle between the rail and the plane of the laser beams was set to 70°. The large collecting lens was mounted on the rail, 500 mm from the crossing volume. The collection assembly was then mounted immediately behind the main lens.

With the laser on and the nozzle spraying, a faint image could be seen at the focal plane of the small receiving lenses. The following procedure was used to align the two channels so that the control volume was in view, and insure that both channels were focussed on the same region within the crossing volume.

- Adjust both of the fiber optic apertures so that they are at approximately the crossing location in the laser image.
- Select one of the two channels for first adjustment. With the aid of the transient recorder and oscilloscope, determine the limits within which signals may be found for different aperture locations. Locate the aperture at the centre of this region, so that it is centred on the crossing volume. (With the long, narrow crossing volume that results from this geometry there is much more play in the horizontal direction than there is in the vertical.)
- Adjust the second channel so that it receives the same signals as the first channel. When two bursts are frozen by the transient recorder, it is easily seen that they result

from the same particle. When the two channels are aligned to view the same location a burst on one channel will always have a corresponding burst on the other channel.

The two channels are now optically aligned. If they are poorly aligned, only those drops that pass through the overlap region will generate signals on both channels. Those particles that are seen by only one channel will produce "orphan bursts", appearing only on that channel. With patience the channels may be very closely aligned by trial and error. The exactness of this alignment is important in reducing the error rate, but does not impact on the measurements, as any "orphan bursts" will be rejected by the verification logic.

The filter settings were adjusted to remove the signal pedestal and high frequency noise, without interfering with the observed signal frequencies. The transient recorder trigger level was set to maintain sensitivity, while providing a reasonable error rate. This is discussed further in section C.3.

With these steps complete, the system was functional, producing signals from the spray that could be analyzed to give drop size and velocity information. However, the meaning and accuracy of that information was not fully known.

C.1.1 System Phase Shift Testing

Despite the use of identical filter banks and similar connecting cables and photomultipliers, there was a difference in the propagation time between the two channels. This resulted in an apparent phase shift for the system, which was present in addition to any true phase shift due to the optical effects.

Initial testing was done by connecting the output of one PMT to both of the filter bank inputs. Thus the same signal was fed into each of the two trains of electronics. With both

filter banks set at the same cutoff frequencies, a phase difference of approximately 100 ns was observed between the two channels. The phase difference was not a function of signal magnitude or frequency, allowing this error to be eliminated by a correction constant.

The values for the correction constant were determined as follows.

- The system was set up in the final measurement configuration.
- Both filter bank inputs were connected to the same PMT.
- A modified version of the measurement program was run, collecting data on the measured phase shift between the two channels.

Since both channels saw the same signal, this yielded a measure of the time lag between signals due to discrepancies between the two channels, downstream of the photomultiplier tubes. The time lag between channels was measured to be 2.164 transient recorder time steps, based on actual spray signals for input. (Each transient recorder time step corresponds to 50 ns.) This value was incorporated into the measurement program as a correction constant for the phase lag between signals. When the same test was repeated after all spray measurements were complete the time lag was 2.07 time steps, with an RMS of 0.59 time steps.

No significant time lag was expected for the fiber optic cables. The speed of light is $c = 3 \times 10^8$ m/s, so that a 1 m variation in optical path length corresponds to a 3.3 ns time lag. As the fiber optics were identical, there should be no significant difference in optical path length, thus no significant time lag. It was not possible to test this assumption.

It was also expected that the PMTs would not introduce a time lag. This was tested by using an LDA burst simulator available at LSTM. It produces a high frequency signal,

within a lower frequency envelope. The signal is available as both analog voltage output, and as an optical burst from a photo diode. If the photo diode is applied to the PMT and the analog output connected to the second transient recorder channel, a propagation delay may be measured for the system. When one photomultiplier was substituted for the other, no difference in the propagation delay was found. Thus it was concluded that both PMTs introduced the same time lag, probably near zero.

C.1.2 Rotating Grating Frequency Shift Measurements

A frequency difference between the two laser beams was introduced by the rotating diffraction grating, making it possible to distinguish positive and negative drop velocities. The controller for the rotating grating was not calibrated, so that measurements of the resulting frequency shift were required.

A short piece of hair was fixed to a glass slide and held stationary in the control volume, providing a strong signal from which the frequency shift could be measured. The value obtained by a modified version of the measurement program was 0.907 MHz with an RMS of 0.0103 MHz. This value was used in the measurement program. The grating controller was left undisturbed for the duration of the measurements. On completion of all measurements the frequency shift was again measured, yielding a value of 0.907 MHz with an RMS of 0.0105 MHz.

C.2 Selection of Verification Parameters

Sensitivity tests were made to determine the effects of using different values for the verification parameters. Testing was done separately for each of the parameters; band size for

zero crossings, phase verification time and frequency verification, both within a signal and between channels. In each case, the parameter was varied both above and below the final value by a factor of two. The resulting measurements were compared for similarity of drop size distribution and rejection rate. Only the rejection rate was found to vary significantly. Tighter tolerances on agreement between signals resulted in much higher rejection rates. All other values showed variations no larger than the statistical variation seen between equivalent measurements using the same parameters.

The values chosen for the verification parameters represent a compromise between rejection rate and tolerance for individual measurements. A lower rejection rate shortens the time required to make a measurement, and reduces the possibility of a bias being introduced by the verification logic. As noted above, no biasing effect was apparent around the values used for the verification parameters.

C.3 Selection of Transient Recorder Trigger Level

The strength of the optical signals from a drop varies with the scattering cross-section of the drop, roughly proportional to square of drop diameter. Thus for a one order of magnitude variation in drop size, the resulting signal strength could vary by two orders of magnitude. For this optical arrangement the strength of signals from the smaller drops approaches the strength of the noise in the system. (This is largely due to the low laser power used in this rig.) As a result, signals cannot be effectively segregated from noise by a level trigger.

The lower the trigger level is set, the more readily it is tripped by spikes of noise, so that at very low levels signals are found only by accident. The bursts of noise are rejected by the verification logic, so that a low trigger level will yield a very high rejection rate. This makes it virtually impossible to complete a measurement.

At higher trigger levels, noise is effectively screened out, however some of the lower strength signals will also be missed. Since signal strength is in part dependent on drop size, this will result in a bias against the recording of smaller drops. Thus, the small end of the drop size spectrum will be under-represented in the measured drop size distribution.

Ideally, there would be a gap between these two trigger levels, so that the system could trigger on virtually all signals, while ignoring the noise. In this system, this was not possible. Figure C.1 shows drop size distributions obtained at different trigger levels. At the trigger level which was used for these measurements, it appears that there is no significant bias against drops larger than 50 μm. Drops below that size are under-represented. This is not a significant problem in this study, as the shape of the drop size distributions at larger drop sizes may be directly compared.

C.4 Estimate of Errors

This section provides an estimate of both the systematic and random errors inherent in these measurements. Standard statistical techniques are used in the estimation. See, for example, reference [36].

C.4.1 Systematic Error in Size and Velocity Measurements

Calculated factors were used to convert the measured frequency and phase shift data into equivalent drop size and velocity data. These factors are functions of the optical system geometry and laser wavelength, as described in section 4.3.2. As such, these calculated factors include any error that was made in measurement of the system geometry. The cumulative effects of these errors are shown in table C.1.

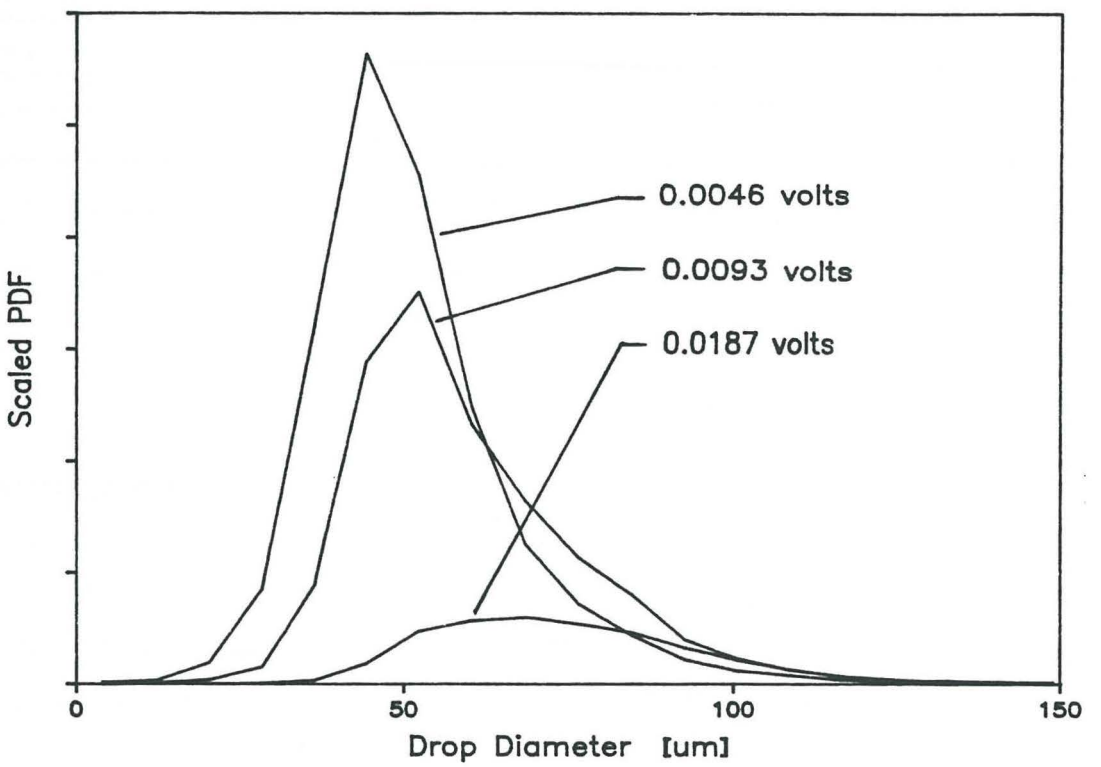

Figure C.1: Trigger level biasing effects. This figure shows drop size distributions taken under the same conditions, but using different transient recorder trigger levels. The PDFs have been scaled for comparison purposes. The trigger level was set at the value used in the measurements (0.0093 volts), as well as at half and twice that value. Notice that at the high trigger level there is an almost complete elimination of small drops from the distribution. The distributions for the other two trigger levels do not show marked differences above a drop size of about 50 μm. Thus it is assumed that there is no important size bias, except against drops of less than 50 μm diameter.

Quantity		Value Used		Tolerance
Laser Wavelength	λ	632.8	nm	~ 0
Beam Separation	x_s	15.0	mm	± 0.25
Sending Lens Focal Length	f_s	310	mm	± 6.2
Beam Crossing Angle	$\theta = 2\tan^{-1}(x_s/2f_s)$	2.77°		$\pm 0.10°$
Velocity / Frequency Factor		13.08	(m/s) / MHz	± 0.49
Scattering Angle	ϕ	70°		$\pm 1°$
Receiving Lens Focal Length	f_r	500	mm	± 10
Receiver Separation	x_r	40.0	mm	± 0.25
Receiver Elevation Angle	$\psi = \tan^{-1}(x_r/2f_r)$	2.29°		$\pm 0.03°$
Refractive Index Ratio	$n' = n_{water}/n_{air}$	1.33		~ 0
Phase / Diameter Factor		1.16	degrees/μm	± 0.03

Table C.1: Geometric factors influencing systematic errors. This table shows error estimates for the measured system geometry, combining to give estimates of the total systematic error present in the size and velocity conversion factors.

The errors in lens focal length are based on a standard 2% tolerance on biconvex, research quality lenses. The error in scattering angle is an estimate, consistent with the lens tolerances. The other values in the table are obtained by propagating those errors through the relations given in section 4.3.2.

Thus, systematic error in velocity should be less than 4%, while the systematic error in the drop size is less than 3%. Because these errors come in through the constants used in linear conversion relations, they are percentages of the actual measured values, rather than percentages of some full scale values.

C.4.2 Error in Individual Velocity Measurements

In addition to the systematic error, error in the velocity measurements came from two different sources. First there is an error due to the inability to accurately determine the frequency of the Doppler signal. In addition, there is an error associated with the uncertainty of the shift frequency of the laser beams.

The verification logic performs three tests of frequency consistency; one on each channel and one between the two. Figure C.2 illustrates this procedure. For each group of four measurements, the standard error in the measurements is

$$S_n = \frac{1}{6}\sqrt{(f_m - a_1)^2 + (f_m - a_2)^2 + (f_m - b_1)^2 + (f_m - b_2)^2} \qquad \text{(C.1)}$$

This is the best estimate of the standard deviation of the measured values about the true values. Since all of the verification logic is based on percentages of the measured frequency, this is better expressed in that form.

$$\frac{S_n}{f_m} = \frac{1}{6}\sqrt{\left(\frac{f_m - a_1}{f_m}\right)^2 + \left(\frac{f_m - a_2}{f_m}\right)^2 + \left(\frac{f_m - b_1}{f_m}\right)^2 + \left(\frac{f_m - b_2}{f_m}\right)^2} \qquad \text{(C.2)}$$

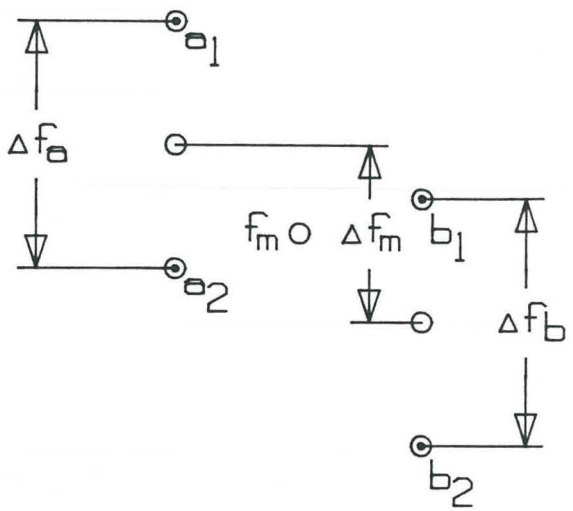

Figure C.2: Errors in velocity measurements. This figure shows the four different frequencies measured, their relation to the mean, measured frequency and forms the basis for the error analysis described in the text.

In the extreme case, where the observations have maximum spread, this has a value of 0.94% standard error. This corresponds to the condition

$$\frac{\Delta f_a}{f_m} = \frac{\Delta f_b}{f_m} = \frac{\Delta f_m}{f_m} = 4\% \tag{C.3}$$

with all deviations at the full value of their tolerances. It seems more reasonable, however, to consider an average over the many possible verified cases. For example, if all of the deviations were to be one half of their tolerance value, the standard error would be 0.47%. The conservative value of 0.94% will be used here, although the actual standard error may be expected to be much lower.

The second indicator of error comes from the RMS of the shift frequency, measured as 0.01 MHz with a sample size of 1000 points. This gives a value for the standard error due to fluctuations in the shift frequency.

Drop Velocity m/s	95% Confidence Interval on Drop Velocity m/s	Linear Approximation m/s
0	±0.344	±0.344
4	±0.397	±0.404
8	±0.456	±0.465
12	±0.519	±0.525
16	±0.586	±0.586

Table C.2: Random error bounds on velocity measurements as a function of velocity. This table shows the bounds of 95% confidence in the measurements of velocity. Because one of the components is linearly dependent on the frequency, the error is larger for larger velocities. As can be seen from the last column, the error is nearly linear.

The velocity is obtained from the formula

$$U_{\perp m} = 13.08(f_m - f_{shift}) \tag{C.4}$$

When two measurements are summed, the standard error of the result is the square root of the sum of the squares of the two standard errors of the individual measurements.

$$U_{\perp m} = 13.08\left((f_t - 0.907) \pm \sqrt{(0.0094 f_t)^2 + 0.01^2}\right) \tag{C.5}$$

gives the standard error of the measurements, neglecting the systematic error described in section C.4.1, above. The 95% confidence interval is twice the standard error. Table C.2 shows the bounds of the 95% confidence interval about the calculated velocity, for different measured frequencies.

C.4.3 Error in Individual Drop Size Measurements

Two measurements of phase shift were obtained for each drop measured. All were in agreement to within one transient recorder time step. Thus the maximum possible standard error on any measurement is 0.5 time steps. This corresponds to 25 ns. In addition there is a small error due to uncertainty in the signal frequency, but this is dwarfed by the tolerance on the phase shift.

Because the error in phase shift is based in time, errors in phase angle will depend on the frequency.

$$\Phi = f_t \Delta t \times 360^\circ \qquad \text{and} \qquad \delta = 1.16\Phi \tag{C.6}$$

Thus, the error in a measured drop size is dependent on that drop's velocity.

$$\delta = 1.16\left(\frac{U_{\perp t}}{13.08} + 0.907\,MHz\right)(\Delta t \pm 0.025\,\mu s) \times 360^\circ \tag{C.7}$$

Drop Velocity m/s	95% Confidence Interval on Drop Size μm
0	$\pm$18.9
4	$\pm$25.3
8	$\pm$31.7
12	$\pm$38.1
16	$\pm$44.5

Table C.3: Random error bounds on drop size measurements as a function of velocity. This table shows the bounds of 95% confidence in the measurements of drop size.

gives the standard error in measured drop diameters, exclusive of the systematic error described in section C.4.1, above. Table C.3 gives the variation in the 95% confidence interval for drop diameter, as a function of drop velocity. It is a linear function of drop velocity, with an offset at zero velocity due to the shift frequency.

The error values given by table C.3 are very large. As with the calculations of the errors in velocity, these represent the extreme. Actual values would be expected to be much lower. Figure 4.11 shows plots of drop size distributions taken under identical conditions, except for variation of the phase shift validation parameter. It takes three values; 0.5, 1 and 2. The only notable variation between the measurements is in the rejection rate. From the analysis above the error should vary strongly between these three cases. Several conclusions are possible:

- The error is very large, but has no effect on the drop size distribution.

- The error is large, but is unaffected by the verification parameter.
- The error is small in all three cases, so that there is naturally very little difference observed.

The first seems unlikely, as with standard errors approaching 20 μm, the distribution would be expected to show some broadening with increasing error levels. The second is entirely contrary to well accepted sampling theory. This leaves only the last possibility, suggesting that the actual errors involved are generally much less than those found in the extreme case.

C.4.4 Error Due to Phase Ambiguity

When a signal is detected by the system, there is no way to differentiate between some phase shift Φ, and the same phase shift increased by one or more wavelengths to $\Phi + 2\pi$, $\Phi + 4\pi$, etc. In this instance, that ambiguity meant that the instrument was unable to differentiate between, for example, a drop of 15 μm and one of 325 μm. This was not a major problem, as very few drops were observed to be larger than 200 μm.

The effects of this ambiguity are visible only in the very small drop sizes where few drops are present. The addition of small numbers of large drops has no effect on the drop size distribution, but it dramatically alters the mean and RMS velocity values recorded. The very small drops have low velocities, very close to the air velocity. The larger drops have not been affected as strongly by drag and have much higher velocities. This effect is responsible for the upturn in both mean and RMS velocity at the smallest drop sizes. The larger drops may be seen as a small, high velocity "hill" in the surface plots of chapter 5.